Dissertation
submitted to the
Combined Faculties of the Natural Sciences and for Mathematics
of the Ruperto-Carola University of Heidelberg, Germany
for the degree of
Doctor of Natural Sciences

Put forward by
Charles Ludwig Majer
born in Freiburg
Oral examination: July 9th, 2014

Joint reconstruction of the mass distributions of galaxy clusters from gravitational lensing and thermal gas

Referees: Prof. Dr. Matthias Bartelmann
Prof. Dr. Joachim Wambsganß

"*But the real way to get happiness is by giving out happiness to other people.*"
– Robert Baden-Powell

Kombinierte Rekonstruktion der Massenverteilungen von Galaxienhaufen mittels Gravitationslinseneffekt und thermischem Gas

Massereiche Galaxienhaufen sind die größten gravitativ gebundenen Objekte im Universum. Ihre Masse kann mittels des Gravitationslinseneffekts bestimmt werden. Um verlässliche Aussagen treffen zu können, ist es besonders wichtig, die dabei auftretenden Unsicherheiten zu quantifizieren, dies ist aber numerisch sehr aufwendig. Wir erarbeiten eine neue Methode, diese Unsicherheiten analytisch zu bestimmen, wobei wir uns auf Massenrekonstruktionen beschränken, die auf dem schwachen Linseneffekt beruhen.

Galaxienhaufen enthalten eine große Menge an intergalaktischer Materie, was zu einer Vielzahl von weiteren Beobachtungsgrößen führt. Die von uns entwickelte Methode kann aus zweien dieser Observablen das Linsenpotential des Haufens bestimmen: Hierzu nutzen wir Signale des thermischen Sunyaev-Zel'dovich-Effekts und die Emission von Röntgenstrahlung in Folge von thermischer Bremsstrahlung. Unter der Annahme, dass sich das Gas im hydrostatischem Gleichgewicht befindet und einer polytropischen Zustandsgleichung folgt, verknüpfen wir diese Observablen mit dem Gravitationspotential. Hierbei ist eine Deprojektion vonnöten, welche wir mittels der Richardson-Lucy-Methode durchführen. Das gesuchte Linsenpotential ergibt sich dann durch eine Projektion des Gravitationspotentials entlang der Sichtlinie. Den Erfolg unserer Methode testen wir an Galaxienhaufen mit vorgegebenem Dichteprofil, einer numerischen N-Teilchen-Simulation und dem Galaxienhaufen RXJ1347.

Unsere Bemühungen sind als die ersten Schritte in Richtung eines nicht-parametrischen Algorithmus zu verstehen, bei welchem wir alle zur Verfügung stehenden Observablen für eine gemeinsame Rekonstruktion der Massenverteilung nutzen wollen. Durch das Einbeziehen mehrerer unterschiedlicher Beobachtungsgrößen, vereint in einem gemeinsam rekonstruierten Linsenpotential, ist es möglich, die Massen von Galaxienhaufen sowie deren interne Struktur deutlich präziser zu bestimmen.

Joint reconstruction of the mass distributions of galaxy clusters from gravitational lensing and thermal gas

We focus on the reconstruction of mass distributions of the massive galaxy clusters, which are the largest gravitationally bound objects in the Universe. An approach to determine the masses of clusters is based on the effects of gravitational lensing. Estimating errors induced by this method is crucial but computationally expensive. We present a novel approach to estimate analytically the errors made by reconstructions which use weak-lensing information.

As galaxy clusters host a large amount of intracluster medium they provide a multitude of observables. We present a new method to infer the lensing potential from two of these: signals of the thermal Sunyaev-Zel'dovich effect and the emission of X-rays due to thermal bremsstrahlung. By assuming that the gas is in hydrostatic equilibrium and follows a polytropic equation of state, we link these observables to the gravitational potential, which is then projected along the line-of-sight to infer the lensing potential. For this we deproject the observables by means of the Richardson-Lucy algorithm. We test our method on clusters with analytic profiles, a numerical simulation and on the galaxy cluster RXJ1347.

Our efforts are the first steps towards a non-parametric algorithm for a joint cluster reconstruction. By taking all possible cluster observables into account, mass distributions of clusters will be determined more accurately.

Contents

Table of Contents ix

List of Figures xi

List of Tables xii

1 Introduction 1

2 Cosmology 5
2.1 Cosmological principle . . . 5
2.2 Friedmann-Lemaître-Robertson-Walker models . . . 6
2.3 Cosmological redshift . . . 7
2.4 Hubble function and density parameters . . . 8
2.5 Distance measures . . . 10
2.6 Structure formation . . . 12
2.7 Mass function . . . 16

3 Galaxy clusters 19
3.1 Cluster structure . . . 19
3.2 Observing galaxy clusters . . . 21

4 Reconstruction of the mass distribution using gravitational lensing 33
4.1 A strong- and weak-lensing reconstruction code . . . 33
4.2 Approaching an analytic error estimation . . . 38
4.3 Application to mock data . . . 41
4.4 Application to an N-body/hydrodynamica cluster simulation . . . 43
4.5 Summary and conclusion . . . 46

5 Richardson-Lucy deprojection 49
5.1 Merits and limits of deprojections . . . 49
5.2 Principles of the Richardson-Lucy deprojection . . . 50
5.3 Richardson-Lucy deprojection and spherical symmetry . . . 52
5.4 Richardson-Lucy deprojection and spheroidal symmetry . . . 53
5.5 Constraining the two degrees of freedom $\boldsymbol{\alpha}$ and $\mathbf{L}$ . . . 55
5.6 Richardson-Lucy method compared to onion peeling . . . 56
5.7 Testing the influence of the free parameters $\boldsymbol{\alpha}$ and $\mathbf{L}$ . . . 58
5.8 Summary and conclusion . . . 60

6 Reconstruction of the mass distribution of clusters using the thermal Sunyaev-Zel'dovich effect 61
6.1 Simulation of ALMA observations . . . 61
6.2 Application to mock data with spherical symmetry . . . 63
6.3 Application to a simulation assuming spherical symmetry . . . 65
6.4 Application to a simulation assuming spheroidal symmetry . . . 66

6.5 Summary and conclusion 68

7 Reconstruction of the mass distribution of clusters using X-ray emission 71
7.1 Simulation of Chandra observations 71
7.2 Application to mock data with spherical symmetry 73
7.3 Application to a simulation assuming spheroidal symmetry 74
7.4 Summary and conclusion 76

8 Application to RXJ1347-1145 77
8.1 RXJ1347 77
8.2 Reconstruction assuming spherical symmetry 78
8.3 Reconstruction assuming spheroidal symmetry 79
8.4 Summary and conclusion 82

9 Conclusion and outlook 83

Bibliography 87

Acknowledgements 97

List of Figures

2.1 Illustration of different curvature. . . . 6
2.2 Density parameters. . . . 10
2.3 Different distance measures. . . . 11

3.1 Images of strong-lensing clusters. . . . 20
3.2 NWF density profile. . . . 21
3.3 Observations of clusters with different methods. . . . 22
3.4 Lensing geometry. . . . 23
3.5 Distortion caused by convergence, shear and flexion. . . . 25
3.6 Frequency change due to the thermal SZ effect. . . . 26
3.7 Images of the Coma cluster. . . . 28
3.8 Spectrum of thermal bremsstrahlung. . . . 30

4.1 Galaxy averaging of *SaWLens*. . . . 35
4.2 Geometry of ellipticity averaging. . . . 38
4.3 Convergence and standard deviation for different regularisation parameters. . . . 42
4.4 Standard deviation for different regularisation parameters from the analytical model. 44
4.5 Convergence and standard deviation for the g1 cluster. . . . 45
4.6 Azimuthal average of the convergence and the standard deviation for the g1 cluster. . 46

5.1 Radial profile and line-of-sight geometry of the spherical RL algorithm. . . . 52
5.2 Spheroidal cluster geometry. . . . 53
5.3 Surface brightness profile and reconstructed emissivity of A1689. . . . 57
5.4 Reconstructed density and temperature profile of A1689. . . . 58
5.5 Reconstructed lensing potential of A1689. . . . 58
5.6 Scatter introduced by α and $L_{\max}$. . . . 59
5.7 Schematic overview of the used reconstruction method. . . . 60

6.1 Specific intensity change for a mock simulation. . . . 64
6.2 Reconstruction of the mock cluster using thermal SZ. . . . 64
6.3 Relative rms of the reconstruction using thermal SZ data. . . . 65
6.4 Compton-y parameter for the g1 cluster. . . . 65
6.5 Reconstruction of the lensing potential and relative rms for the g1 cluster. . . . 66
6.6 Specific intensity change for the g1 cluster. . . . 67
6.7 Spheroidal reconstruction for the g1 cluster. . . . 68

7.1 Surface brightness of a mock cluster. . . . 72
7.2 Reconstruction of the mock cluster using X-ray emission. . . . 73
7.3 The g1 cluster as seen with Chandra. . . . 74
7.4 Spheroidal reconstruction for the g1 cluster. . . . 75

8.1 Thermal SZ signal of RXJ1347-1145 at 140 GHz. . . . 78
8.2 Spherical reconstruction of RXJ1347-1145. . . . 79
8.3 Spheroidal reconstruction of RXJ1347-1145. . . . 81
8.4 One-dimensional view of the spheroidal reconstruction of RXJ1347-1145. . . . 81

List of Tables

2.1 Density parameters, Hubble constant, and σ_8. 9

4.1 Main properties of the cluster g1. 44

Chapter 1

Introduction

In recent years modern cosmology has become a major branch in physics. With a multitude of new available data sets and an ever increasing accuracy, cosmology evolved to a field of research illuminating the Universe as a whole with tight bounds on introduced cosmological parameters.

The successful *cosmological standard model*, also known as ΛCDM, explains the Universe with a minimal set of six parameters. According to this model the Universe emerged from a singularity with a *Big Bang* 13.7 billion years ago. Shortly thereafter – considering cosmological time scales – matter and radiation decoupled. This is nowadays observed in the *Cosmic Microwave Background* (CMB). It was released approximately 400,000 years after the Big Bang. The ΛCDM model postulates the existence of a cosmological constant Λ. It was introduced in the field equations by Einstein himself to account for the possibility of a static Universe. The standard model further postulates the existence of an unknown and not electromagnetically interacting – hence *dark* – matter component, so far only known to interact gravitationally (or maybe weakly) with 'ordinary' matter. It further states that structures in the Universe evolved hierarchically starting with tiny density fluctuations, imprinted in the CMB. Their amplitudes grew over time and due to non-linear structure formation they formed the *cosmic web* and the massive galaxy clusters imbedded there. The dark matter component accounts for 26.8% and the cosmological constant for 68.3% of the total energy density of the Universe, leaving us with 4.9% (see Planck Collaboration, 2013a) for the world we know – given by baryonic matter. To summarise: 95.1% of the energy density lie in the *dark* and are not understood so far.

The Universe we observe today appears spatially flat. A spatially flat universe involves a high degree of fine-tuning, raising the so called *flatness problem*. Another observational constraint is the CMB, which is almost perfectly isotropic – relative primary anisotropies are of the order 10^{-5}. The primordial density fluctuations imprinted in the CMB are correlated on large scales. These scales are larger than the horizon within which signals have been able to be in causal contact at the time of recombination. This issue is stated by the so-called *horizon problem*. Some form of early accelerated expansion – called *inflation* – is capable to resolve both mentioned problems.

The latest objects formed, according to hierarchical structure formation, are galaxy clusters. The core structure of galaxy clusters provides important cosmological information. Based on numerical simulations, we expect the dark-matter distribution to follow a universal profile with characteristic gradients and a scale radius (Navarro et al., 1997). Outside relatively small central regions, cluster density profiles should not be strongly affected by baryonic physics because of the long cooling times in the intracluster plasma compared to the Hubble time. Cold dark matter is expected to clump on virtually arbitrarily small scales. The level of substructure in clusters thus potentially constrains the nature of the dark matter particles (Boylan-Kolchin et al., 2009; Gao et al., 2011). Further, the ratio between the scale and the virial radii of galaxy clusters, dubbed the concentration parameter, has been frequently observed to be substantially different than theoretically expected. In particular, in strongly gravitationally lensing clusters, concentration parameters that are significantly higher than those found in numerical simulations have been reported (e.g. Coe et al., 2012, Fig. 14), for example *Abell 1689*

(Goldberg & Leonard, 2007; Umetsu & Broadhurst, 2008; Broadhurst et al., 2008). For *Abell 1689* a multitude of different observations are available. This cluster has been modelled to explain the observed strong and weak-lensing features favouring a low concentration parameter. X-ray analyses, however, draw a different picture of this massive cluster as they favour very high concentrations ≈ 14 (Peng et al., 2009). These findings are claimed to be in some tension with the standard model of cosmology (Corless et al., 2009; Oguri et al., 2009) as at present they are only weakly consistent with ΛCDM. However, this issue is maybe due to our present techniques to infer the concentration parameter of massive galaxy clusters.

Another problem, closely related to the concentration problem, is the arc-statistic problem (Bartelmann et al., 1998), stating that massive galaxy clusters produce more arcs (i.e. strong-lensing features) than theory is able do predict. This problem remains largely unsolved up to date. Attempts have been made at explaining high concentrations and thus a high number of arcs by including trixiality of the clusters (e.g. Oguri et al., 2003), but the core of this problem still remains.

Numerous other problems are raised once high-resolution simulations of structure formation of cold dark matter are compared to observations. A prominent one is concerning the aforementioned density profile. Simulations predict a universal profile of dark matter halos which have *cuspy* cores. Observations, however, favour *flat* cores in the central regions of clusters. This discrepancy is called the *core-cusp problem* (e.g. de Blok, 2010).

Even though many attempts have been made to explain the discrepancies, we are far from a consistent picture of structure formation. It is fundamental to find out whether these discrepancies reflect insufficient understanding at the level of our theory of cosmological structure formation, or whether it is a combination of baryonic physics, selection effects, and measurement biases that gives rise to these differences between theory and observations.

Considering the constraints they give on the cosmological standard model, the mysteries they hold and the multitude of observables they provide, galaxy clusters are clearly the class of objects to study. In the following discussion we will focus on the following observables: Weak and strong gravitational lensing effects enable a direct estimate of the scaled surface-mass density of a lensing mass distribution. X-ray emission and the thermal Sunyaev-Zel'dovich (SZ) effect reflect the physical state of the hot intracluster gas. Assuming equilibrium and hydrostatic stability, the gas properties can also be related to the gravitational potential. This suggests to devise a method by which lensing, X-ray, and thermal SZ data can be combined in a joint analysis aiming at recovering the gravitational potential best compatible with all observables. We enter the stage of multi-wavelength reconstructions. There already exist several works on reconstructions based on multiple data sets (Reblinsky, 2000a; Doré et al., 2001; Puchwein & Bartelmann, 2006). However, these works use separate reconstructions for each observable rather than one consistent algorithm to reconstruct them all together. Recent applications (e.g. De Filippis et al. 2005; Sereno 2007; Yuan et al. 2008; Nord et al. 2009; Basu et al. 2010) have shown how precious and valuable the information is one is capable to retrieve with multiple probes.

In this work we present a consistent method to infer the lensing potential from the thermal SZ effect and the X-ray emission. This marks, together with the findings from Sarli et al. (2013) on galaxy kinematics and the work of Merten (2010) on gravitational lensing, the beginning of a multi-wavelength approach on the common ground of the line-of-sight projected gravitational potential – which is proportional to the lensing potential.

In two major parts we cover the three aforementioned observables – gravitational lensing, thermal SZ effect and X-ray emission – and explain our method to infer the lensing potential from them. The first part focusses on the errors made by using reconstructions of the mass distribution based on weak gravitational lensing and how these are estimated. The second part covers our approach to reconstruct the lensing potential from the thermal SZ effect and the X-ray emission of galaxy clusters.

The overall structure of this thesis is as follows: We start with a short review of modern cosmology in Chapter 2 to familiarise the reader with those parts of cosmology which are needed in the subse-

quent chapters. We then concentrate the discussion in Chapter 3 on massive galaxy clusters and the different observables they provide. There we also discuss the fundamental relation between the used observables and the lensing potential. But before we apply our reconstruction method to data, we first explain the strong- and weak-lensing reconstruction code *SaWLens* of Merten (2010) in Chapter 4. For the weak-lensing reconstruction of *SaWLens* we derive an analytic error estimation and verify our results with a numerical experiment. We finish this first major part with an application to a hydrodynamical/N-body simulation of a massive galaxy cluster. Entering the second major part, we proceed to the details of our reconstruction algorithm in Chapter 5. Here we describe the used deprojection method. With it, we are capable to retrieve the line-of-sight projected cluster potential from the X-ray surface brightness and observations of the thermal SZ effect. By applying our deprojection method to the galaxy cluster Abell 1689, we compare our deprojection method to the conventionally used *onion peeling* method. Numerical tests, described in Chapter 6 and 7, illustrate how our reconstruction algorithm performs under realistic conditions. Although we adopt a spherically symmetric cluster potential for the tests, spherical symmetry is not a necessary condition for our algorithm to work. The influence of a possible deviation from spherical symmetry is exemplified in Section 6.3 with a data set from a hydrodynamical/N-body simulation. We further extend our algorithm towards spheroidal cluster geometries and apply it to a simulated cluster in Section 6.4 for the thermal SZ effect. In the same manner we use X-ray emission in Section 7.3. Finally, we have a thermal SZ observation of the galaxy cluster RXJ1347-1145 from Sayers et al. (2013) to apply our reconstruction method to. The detailed results of this application are presented in Chapter 8. We conclude and give an outlook in Chapter 9.

Parts of this work were published in the following articles:

- Konrad, S., **Majer, C. L.**, Meyer, S., Sarli, E., & Bartelmann, M. (2013): *Joint reconstruction of galaxy clusters from gravitational lensing and thermal gas I. Outline of a non-parametric method.* A&A, 553, A118.
- **Majer, C. L.**, Meyer, S., Konrad, S., Sarli, E., & Bartelmann, M. (2013): *Joint reconstruction of galaxy clusters from gravitational lensing and thermal gas II. Inversion of the thermal Sunyaev-Zel'dovich effect.* ArXiv e-prints: 1304.6522
- Tchernin, C., **Majer, C. L.**, Meyer, S., Sarli, E., Eckert, D., & Bartelmann, M. (2013): *Reconstruction of the lensing potential of the cluster A1689 from X-ray measurements.* Submitted

2 Chapter 2
Cosmology

Cosmology has its linguistic origins in the greek language, κόσμος λογία, meaning *study of the world* and was more of philosophical nature. The Greek also marked the earliest form of cosmology, nowadays known as *celestial mechanics*. More than 2300 years after that, cosmology has evolved to a fundamental branch in modern physics, amongst others describing the evolution of our Universe. Even though we are capable to observe the Universe 'shortly' after the *Big Bang*, we sometimes touch the realm of philosophy, just as our ancient ancestors.

In this chapter we want to present some parts of modern cosmology which the reader may be in need of to follow the line of thought throughout this thesis. Focussing only on the very fields of cosmology needed, this overview is certainly not complete. As we concentrate on the discussion of massive galaxy clusters and structure formation, it is not necessary to discuss the field of the early Universe. This includes the time of *recombination*, *primordial nucleosynthesis* as well as *inflation*. These special fields of cosmology, as well as the content presented, are covered in numerous text books, e.g. Weinberg (2008); Mukhanov (2008); Schneider (2006b), notes by Bartelmann (2004) or the thesis of Angrick (2011) and Merkel (2013).

2.1 Cosmological principle

We want to start this chapter with an axiom – the *cosmological principle*, which consist of two statements. The first implies that the Universe is isotropic. This is a bold assumption dating back to the beginnings of modern cosmology, though this principle is clearly violated on small scales as we observe the night sky. But it is accepted if averaged over sufficiently large scales. On scales larger than 100 Mpc isotropy is observed by a multitude of surveys, e.g. of the *cosmic microwave background* (CMB) with the *Wilkinson Microwave Anisotropy Probe* satellite (WMAP). The second assumption of the cosmological principle is the *Copernican principle*, saying that our position in the Universe is not preferred over others. Both the assumptions combined obviously lead to an Universe which has to be *homogeneous*.

Given this cosmological principle more questions about our Universe are raised. The most prominent and crucial question for modern cosmology is how anisotropies, like the Milky Way, evolved whereas the Universe remains homogeneous on large scales.

Observations of the CMB are heavily supporting the assumption of homogeneity. The CMB itself originates from the time when the temperature of the cosmic plasma dropped below $\sim 3000\,\mathrm{K}$ and photons decoupled from protons and electrons. At this time, roughly 400,000 years after the Big Bang, our Universe turned from opaque to optically thin, allowing the CMB photons to reach us today. Due to the cosmic expansion the temperature of the CMB photons dropped to $T_0 = 2.73\,\mathrm{K}$ today. Observations of the CMB reveal very small relative temperature fluctuations of the order $10^{-5}\,\mathrm{K}$, reflecting those of the energy distribution of the Universe back at the time of decoupling. This is taken

as a proof that the early Universe was extremely homogeneous and today's anisotropies emerged from these fluctuations and evolved to what we today see as galaxies and galaxy clusters.

The time evolution of the Universe is governed by gravity as the other fundamental interactions are limited to length scales typical for elementary particles (i.e. strong and weak interactions) or limited by the shielding of opposite charges (i.e. electromagnetic interactions). Gravity is described in the framework of *General Relativity* (GR) (Einstein, 1915), describing *space-time* as a four-dimensional manifold with a metric $g_{\mu\nu}$. Due to symmetry, this rank-2 tensor in four dimensions has ten independent components. The dynamics of the metric are then described by *Einstein's field equations* which connect the geometry of space-time with its energy content. The field equation can be written as

$$R_{\mu\nu} - \frac{1}{2} g_{\mu\nu} R - \Lambda g_{\mu\nu} = \frac{8\pi G}{c^4} T_{\mu\nu} \,, \tag{2.1}$$

with the Ricci tensor $R_{\mu\nu}$, the Ricci scalar R and the *cosmological constant* Λ. The Ricci tensor is obtained from the Riemann tensor by contraction $R_{\mu\nu} = R^{\alpha}{}_{\mu\alpha\nu}$ and the Ricci scalar is given by the trace of the Ricci tensor $R = R^{\mu}{}_{\mu}$. The Riemann tensor itself characterises the curvature and contains second derivatives of the metric. The *energy-momentum tensor* $T_{\mu\nu}$ describes the matter content of the Universe. The constants are Newton's gravitational constant G and the speed of light c. For weak gravitational fields and non-relativistic matter Newtonian gravity is restored. GR is highly non-linear as seen above: The geometry of space-time dictates the motion of matter and energy, vice versa the energy content determines the geometry of space-time.

2.2 Friedmann-Lemaître-Robertson-Walker models

For describing the geometry of space-time we are in need of a metric with the line element

$$\mathrm{d}s^2 = g_{\mu\nu} \, \mathrm{d}x^{\mu} \, \mathrm{d}x^{\nu} \,, \tag{2.2}$$

containing the metric tensor $g_{\mu\nu}$ which is chosen to have the signature $(-1, 1, 1, 1)$.

If the metric fulfils the cosmological principle it is called a *Robertson-Walker* (RW) *metric* (Robertson, 1935; Walker, 1935). Due to isotropy synchronisation between any two clocks needs to be possible, reducing the line element to

$$\mathrm{d}s^2 = c^2 \, \mathrm{d}t^2 + g_{ij} \, \mathrm{d}x^i \, \mathrm{d}x^j \,, \tag{2.3}$$

and allowing the global foliation of space-time into spatial hyper-surfaces. These are scaled by the *cosmological scale factor* $a(t)$, responsible for potential isotropic contractions or expansions of the Universe as a whole. Since the hyper-surfaces have to be isotropic and homogeneous, they are spaces of constant curvature and are parameterised by the curvature K and further illustrated in Fig. 2.1. Three different cases are distinguishable:

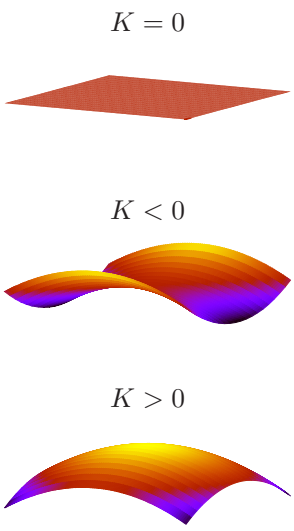

Figure 2.1: Three different curvature parameters which correspond to different geometries.

(1) $K < 0$: *open* Universe,

(2) $K = 0$: *flat* Universe,

(3) $K > 0$: *closed* Universe.

By introducing the set of polar coordinates (χ, θ, ϕ), we can rewrite the line element from above as

$$\mathrm{d}s^2 = -c^2\,\mathrm{d}t^2 + a^2(t)\left[\mathrm{d}\chi^2 + f_\mathrm{K}^2(\chi)(\mathrm{d}\theta^2 + \sin^2\theta\,\mathrm{d}\phi^2)\right], \tag{2.4}$$

with

$$f_\mathrm{K}(\chi) = \begin{cases} \frac{\sinh(\sqrt{|K|}\chi)}{\sqrt{|K|}} & \text{if } K < 0\,, \\ \chi & \text{if } K = 0\,, \\ \frac{\sin(\sqrt{K}\chi)}{\sqrt{K}} & \text{if } K > 0\,. \end{cases} \tag{2.5}$$

Moving on to the time evolution of the scale factor, we specify the energy-momentum tensor in Eq. (2.1) as the one of a perfect fluid with density ρ and pressure p. In its eigenframe it has the components $T^0_0 = -\rho c^2, T^i_j = p\delta^i_j$, and all other entries are equal to zero. With this we can simplify the field equations (2.1) to the two *Friedmann equations* (Friedmann, 1922, 1924; Lemaître, 1927):

$$\left(\frac{\dot{a}}{a}\right)^2 = \frac{8\pi G}{3}\rho - \frac{Kc^2}{a^2} + \frac{\Lambda}{3}\,, \tag{2.6}$$

$$\frac{\ddot{a}}{a} = -\frac{4\pi G}{3}\left(\rho + \frac{3p}{c^2}\right) + \frac{\Lambda}{3}\,. \tag{2.7}$$

The scale factor $a(t)$ may be normalised such that at present $a(t_0) \equiv 1$. If the scale factor of a RW metric satisfies Eq. (2.6) and Eq. (2.7) this metric is called a *Friedmann-Lemaître-Robertson-Walker* (FLRW) metric.

2.3 Cosmological redshift

In the year 1917 Vesto Slipher measured the *redshift* of galaxies, though it was Georges Lemaître who interpreted the data correctly in 1927 as the expansion of the Universe. However, credits were given to Edwin Hubble in 1929 and the relation between velocity and distance is called *Hubble's law* (Hubble, 1929). It states that extragalactic objects like other galaxies are moving away from us with a velocity proportional to their distance to us. The light emitted from these moving objects is then *redshifted*. The expansion itself is parameterised by the scale factor $a(t)$, as explained above. In the framework of GR this observation can be understood as follows: as light moves on null geodesics with constant θ and ϕ, the line element $\mathrm{d}s^2$ has to vanish

$$\mathrm{d}s^2 = 0 \quad \Rightarrow \quad c\,\mathrm{d}t = -a(t)\,\mathrm{d}\chi\,. \tag{2.8}$$

By integrating this from the time of photon emission t_e to present time t_0

$$\chi = \int_{t_\mathrm{e}}^{t_0} \mathrm{d}\chi = \int_{t_\mathrm{e}}^{t_0} \frac{c\,\mathrm{d}t}{a(t)} = \text{const.}\,, \tag{2.9}$$

we see that the derivative of χ with respect to t_e has to vanish:

$$\frac{\mathrm{d}\chi}{\mathrm{d}t_\mathrm{e}} = 0 = \frac{c}{a(t_0)}\frac{\mathrm{d}t_0}{\mathrm{d}t_\mathrm{e}} - \frac{c}{a(t_\mathrm{e})} \Rightarrow \frac{\mathrm{d}t_0}{\mathrm{d}t_\mathrm{e}} = \frac{a(t_0)}{a(t_\mathrm{e})}\,. \tag{2.10}$$

A time interval changes during the time of emission and detection of the signal by an observer. This change is proportional to a change in the scale factor of the Universe. Since the frequency of the emitted signal is inversely proportional to a physical time interval and the scale factor increases with time, the signal is shifted towards smaller frequencies. This in turn implies that the wavelength λ is shifted to larger values, e.g. blue light is shifted to the red end of the optical band, the light gets *redshifted*. The cosmological redshift z is then defined as

$$1 + z \equiv 1 + \frac{\lambda_0 - \lambda_\mathrm{e}}{\lambda_\mathrm{e}} = \frac{a(t_0)}{a(t_\mathrm{e})} = \frac{1}{a(t_\mathrm{e})}\,. \tag{2.11}$$

2.4 Hubble function and density parameters

It is common to define the *Hubble function* $H(t)$,

$$H(t) \equiv \frac{\dot{a}}{a}\,, \tag{2.12}$$

with the value $H_0 \equiv H(t_0)$ today. This time-dependent function quantifies the recessional velocity of distant objects, or equivalently the time evolution of Hubble's law, see Section 2.3. The Hubble constant is given in units km s^{-1} Mpc^{-1} and often written as h in units of 100 km s^{-1} Mpc^{-1}.

We now introduce the so-called *equation of state parameter* w,

$$w \equiv \frac{p}{\rho c^2}\,. \tag{2.13}$$

For different types of matter we may have different values for w. Non-relativistic matter ρ_m is characterised by $w = 0$ and relativistic matter (any form of radiation and neutrinos) ρ_r by $w = 1/3$. Non-relativistic matter is composed of baryonic matter ρ_b and *cold dark matter* (CDM) ρ_CDM. The term 'cold' refers to the non-relativistic character and 'dark' as it is not electromagnetically interacting. CDM is so far only accessible to us through its gravitational interaction and its existence is indicated by rotation curves of galaxies and CMB measurements.

By combining the Friedmann equations (2.6) and (2.7), we find an *adiabatic equation*. This in combination with Eq. (2.13) allows us to infer the dependence of the density on the scale factor,

$$\rho_\mathrm{m} \propto a^{-3} \quad \text{and} \quad \rho_\mathrm{r} \propto a^{-4}\,. \tag{2.14}$$

The difference of the two types is understood as follows: The density of non-relativistic matter is diluted by the expansion of the Universe but photons experience an additional redshift, diminishing their energy. Introducing the dimensionless *critical density*

$$\rho_\mathrm{crit} \equiv \frac{3H^2(t)}{8\pi G}\,, \tag{2.15}$$

allows us to define the dimensionless *density parameters*,

$$\Omega_\mathrm{m} \equiv \frac{\rho_\mathrm{m}}{\rho_\mathrm{crit}} \quad \text{and} \quad \Omega_\mathrm{r} \equiv \frac{\rho_\mathrm{r}}{\rho_\mathrm{crit}}\,. \tag{2.16}$$

Correspondingly, contributions from the cosmological constant ρ_Λ and from the curvature ρ_K are given by:

$$\Omega_\Lambda \equiv \frac{\Lambda}{3H^2} \quad \text{and} \quad \Omega_\mathrm{K} \equiv -\frac{Kc^2}{H^2}\,. \tag{2.17}$$

With these dimensionless parameters and the Hubble function and further replacing ρ by $\rho_\mathrm{m} + \rho_\mathrm{r}$, the first Friedmann equation (2.6) yields

$$H^2(a) = H_0^2\left(\Omega_{\mathrm{r}0}a^{-4} + \Omega_{\mathrm{m}0}a^{-3} + \Omega_{\mathrm{K}0}a^{-2} + \Omega_{\Lambda 0}\right) \equiv H_0^2 E^2(a)\,, \tag{2.18}$$

where we define quantities with the subscript '0' as their present values and also define the *expansion function* $E(a)$. Equation (2.6) additionally constrains the density parameters

$$\Omega_\mathrm{r} + \Omega_\mathrm{m} + \Omega_\mathrm{K} + \Omega_\Lambda = 1 \quad \text{for all } a\,, \tag{2.19}$$

which implies that only three of the density parameters are independent. Most interestingly, referring to Eq. (2.18), all density parameters scale with different powers of the scale factor a. For instance,

Table 2.1: Density parameters, Hubble constant, and σ_8.

Parameter	*WMAP*	*Planck*
Ω_{m0}	$0.288^{+0.0093}_{-0.0092}$	0.314 ± 0.014
Ω_{b0}	0.0472 ± 0.0010	0.0486 ± 0.0021
Ω_{CDM0}	$0.2408^{+0.0093}_{-0.0092}$	0.263 ± 0.013
Ω_{r0}	$(8.689 \pm 0.110) \times 10^{-5}$	$(9.187 \pm 0.382) \times 10^{-5}$
$\Omega_{\Lambda 0}$	$0.712 \pm +0.010$	0.686 ± 0.020
h	0.6933 ± 0.0088	0.674 ± 0.014
σ_8	0.830 ± 0.018	0.834 ± 0.027

Compilation of the density parameters and the Hubble constant today and σ_8. The normalisation of the linear power spectrum σ_8 will be discussed in Section 2.6.2. The *WMAP* data is a best-fit from the nine-year ΛCDM *WMAP*+BAO+H_0 data (Hinshaw et al., 2013) and the third column gives the results from the *Planck* CMB temperature power spectrum alone (Planck Collaboration, 2013a). The radiation density parameter $\Omega_{\mathrm{r0}} = 2.469 \times 10^{-5}\, h^{-2}(1 + 0.2271\, N_{\mathrm{eff}})$ includes the contribution of neutrinos with an effective number of species $N_{\mathrm{eff}} = 3.046$.

the radiation density is much smaller than the matter density today, but going back in time, it grows inevitably faster until the epoch when radiation dominated. Vice versa, at present the density parameter of the cosmological constant dominates over the other density parameters. Figure 2.2 depicts the three density parameters in dependence of the scale factor and indicates the different epochs of evolution in a spatially flat Universe.

The expansion function $E(a)$ further determines the age t of the Universe since $H = \dot{a}/a$,

$$H_0 t = \int_0^a \frac{\mathrm{d}a'}{a'\, E(a')}\,, \tag{2.20}$$

assuming $t = 0$ for $a = 0$. Concentrating on the radiation-dominated and matter-dominated eras we can make further statements. For the matter-dominated era we assume a so-called *Einstein-de Sitter Universe*, a flat Universe that only contains matter (i.e. $\Omega_{\mathrm{m}} = 1$) and obtain

$$a \propto \begin{cases} \sqrt{t} & \text{for radiation-domination and} \quad E(a) = \sqrt{\Omega_{\mathrm{r0}}}\, a^{-2} \\ t^{2/3} & \text{for matter-domination and} \quad E(a) = \sqrt{\Omega_{\mathrm{m0}}}\, a^{-3/2}\,. \end{cases} \tag{2.21}$$

A major goal in modern cosmology has been to measure the above density parameters, wherefore several missions have been launched. The latest measurements infer their results from CMB measurements combined with measurements from *baryon acoustic oscillations* (BAO) and local measurements of the Hubble constant H_0 (Hinshaw et al., 2013). BAOs are oscillations of sound waves, which emerge from the counteraction of the radiation pressure pointing outwards and inwards pointing gravitational force in the primordial plasma before recombination. In Tab. 2.1 we show the results from the *WMAP* (Hinshaw et al., 2013) after the nine-year data release and the first measurements of *Planck* (Planck Collaboration, 2013a).

According to the Planck measurements and assuming a flat Universe, the Universe is filled by roughly 4.9% matter that we are familiar with, baryonic matter. 26.8% are due to dark matter. But even more energy, namely 68.3%, is contributed from the cosmological constant Λ. Today the contribution from radiation is negligible and of the order of 10^{-5}. This leaves us with 95.1% of the total energy content which is dark and unknown to us. Despite this lack of understanding of the 'dark'

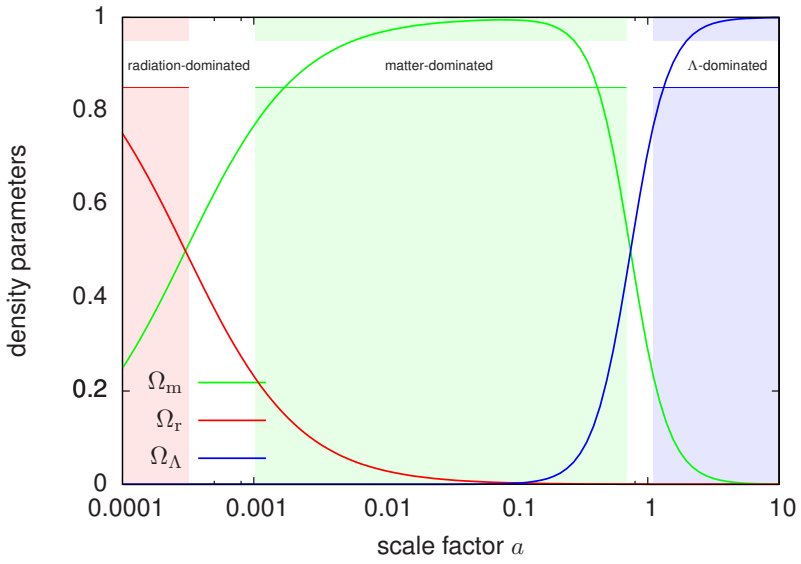

Figure 2.2: Evolution of the three density parameters assuming a flat ΛCDM model with best-fit values from WMAP9+BAO+H_0 measurements.

components, for which 'observations' must always be indirect, the sketched ΛCDM describes our Universe accurately to a high degree. Therefore, it is nowadays also called the *standard model of cosmology*.

Observations of Supernovae Type Ia [1] (SN Ia) indicate that the Universe is currently in a state of accelerated expansion (Riess et al., 1998; Perlmutter et al., 1999). The second Friedmann equation (2.7) then requires an equation of state parameter $w < -1/3$ or equivalently 'negative pressure'. One candidate for this energy density contribution is the cosmological constant Λ which has $w = -1$. An explanation for Λ may be found in the vacuum energy density, which serves as a further source of gravity. However, this would lead to an energy density 120 orders of magnitude larger than the observed value of the critical density. In a more general context the missing energy density is phrased *dark energy*. Various explanations for the dark energy exist in the literature, one is the class of the so-called *quintessence models* (Wetterich, 1988; Ratra & Peebles, 1988; Caldwell et al., 1998). In this framework dark energy is supposed to be distinguishable from the cosmological constant and described by a scalar field. The energy-momentum tensor of this scalar field acts on the right-hand side of Eq. (2.1). Another class of models considers changes on the left-hand side of Eq. (2.1), which alters the nature of gravity. Hence they are called *modified gravity models*.

A further puzzling fact of the ΛCDM model is that the cosmological constant started to dominate the energy content of the Universe rather recently, allowing us to observe the accelerated expansion. This is called *why now problem*.

2.5 Distance measures

Euclidian space allows us the definition of unique distance measures, which is not possible anymore in a curved space-time. Depending on the measurement description different measures have to be considered, wherefore we want to explain four commonly used measures: The proper distance, the

[1] SN Ia, according to current models, are located in binary systems, where a white dwarf and a red giant are in close proximity. As the red giant evolves and exceeds its *Roche volume*, it starts to lose mass to the white dwarf. On the other hand, the white dwarf's mass is limited by the *Chandrasekhar mass*, as its stability arises from the Fermi pressure of its degenerated relativistic electron gas. Once the white dwarf exceeds the Chandrasekhar mass it collapses and releases a specific amount of energy. Therefore all SN Ia nearly peak at the same absolute luminosity, allowing a distant observer to infer its *luminosity distance*.

comoving distance, the angular diameter distance and the luminosity distance. The luminosity and angular-diameter distance are defined in regard of their Euclidian counterpart and reparameterised in curved space-time.

i. Proper distance

The proper distance D_p is given by the time a light signal needs to propagate from the source to the observer, defined as

$$\mathrm{d}D_\mathrm{p} \equiv -c\,\mathrm{d}t = -c\frac{\mathrm{d}a}{\dot{a}}\,, \tag{2.22}$$

where the minus sign ensures that the proper distance increases away from the observer while a and t decrease. Integrating this equation and using Eq. (2.18), the proper distance between two redshifts z_1 and z_2 is

$$D_\mathrm{p}(z_1, z_2) = \frac{c}{H_0}\int_{a(z_2)}^{a(z_1)} \frac{\mathrm{d}a'}{a' E(a')}\,. \tag{2.23}$$

ii. Comoving distance

The comoving distance D_c describes the distance between a source and a distant observer, both co-moving with the cosmic flow on the spatial hypersurface. Any change in the expansion given by the scale factor a has to be divided out, thus

$$\mathrm{d}D_\mathrm{c} \equiv \frac{-c\mathrm{d}t}{a} = -c\frac{\mathrm{d}a}{a\dot{a}}\,. \tag{2.24}$$

Again, the integral gives the distance between two redshifts,

$$D_\mathrm{c}(z_1, z_2) = \frac{c}{H_0}\int_{a(z_2)}^{a(z_1)} \frac{\mathrm{d}a'}{a'^2 E(a')}\,. \tag{2.25}$$

iii. Angular diameter distance

The angular diameter distance D_A is defined, as in Euclidian space, as the fraction of the proper size of an object δl and its observed solid angle $\delta\vartheta$,

$$D_\mathrm{A} \equiv \frac{\delta l}{\delta\vartheta}\,. \tag{2.26}$$

The physical size in comoving coordinates is given by the FLRW metric Eq. (2.4)

$$\delta l = a f_\mathrm{K}(\chi)\,\delta\vartheta\,, \tag{2.27}$$

which yields the angular diameter distance

$$\begin{aligned} D_\mathrm{A}(z_1, z_2) &= a(z_2) f_\mathrm{K}[\chi(z_1, z_2)] \\ &= a(z_2) f_\mathrm{K}[D_\mathrm{c}]\,, \end{aligned} \tag{2.28}$$

with f_K from Eq. (2.5).

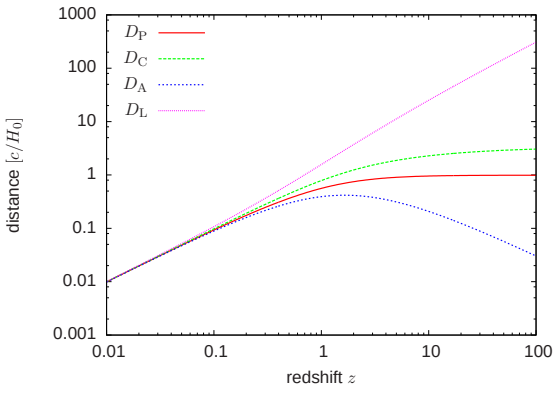

Figure 2.3: Double logarithmic plot of the four distance measures in dependence of redshift z for a spatially flat ΛCDM model ($\Omega_{\mathrm{m}0} = 0.272$ and $\Omega_{\Lambda 0} = 0.728$).

iv. Luminosity distance

The luminosity distance D_L is derived from the relation between the total luminosity L of an object at z_2 and the received flux F at z_1

$$F \equiv \frac{L}{4\pi D_\mathrm{L}^2}\,. \tag{2.29}$$

This definition is again generalised to curved space and comoving coordinates. Due to the *Etherington relation*, the luminosity distance is given as

$$D_{\mathrm{L}}(z_1, z_2) \equiv \left[\frac{a(z_1)}{a(z_2)}\right]^2 D_{\mathrm{A}} = \frac{a(z_1)^2}{a(z_2)} f_{\mathrm{K}}[D_{\mathrm{c}}]\,. \tag{2.30}$$

The above defined cosmological distance measures are plotted in Fig. 2.3 in dependence of redshift for a spatially flat ΛCDM model. For small redshifts (i.e. $z \lesssim 0.2$) all distance measures return approximately the same distance, but for larger redshifts the discrepancy becomes more severe. For instance, in a spatially flat Universe the angular diameter distance D_{A} is given by

$$D_{\mathrm{A}}(z) = \frac{\chi}{1+z}\,. \tag{2.31}$$

This has the interesting feature that for small z the angular diameter distance increases, but for larger redshifts it decreases, as seen in Fig. 2.3. Furthermore, the proper and the comoving distance flatten for large redshifts, which indicates the existence of a *particle horizon*. Such a horizon implies that since the Big Bang light can only have travelled a finite distance, limiting the influence on particles to finite regions.

2.6 Structure formation

Up to this point the picture we drew of our Universe was based on the assumption of homogeneity, thus the Universe would be structureless. However, observing the night sky reveals a multitude of structures visible, like our Milky Way, massive galaxy clusters, large filamentary structures or the voids in between, together also known as the *cosmic web*. In the following sections we want to explain how structures in the Universe evolved. As indicated by the measured matter power spectrum structure formed hierarchically: Small halos form at high redshifts and larger ones formed later. This scenario is called *hierarchical structure formation*.

The model of structure formation assumes that structures are forming by gravitational instability emerging from small fluctuations at early times in the Universe. The amplitudes of these fluctuations then grow due to gravitational instability. The origin of these fluctuations is unknown. One assumes them to be related to quantum fluctuations shortly after the Big Bang, enlarged in scale during the phase of *inflation*. In this scenario the fluctuations would be uncorrelated and their amplitudes would be Gaussian distributed. Assuming further that the relative matter fluctuations are small, they can be assessed as small perturbations of a uniform background density, allowing us to apply linear perturbation theory.

Assuming dark matter particles to be collisionless and other matter components to interact microscopically very strong, mass, momentum and energy conservation is guaranteed. In this case we can describe the matter content of the Universe as a perfect fluid, applicable at least on large scales. We can apply the hydrodynamic equations for the density ρ, the velocity $\boldsymbol{v}$ and pressure P in the gravitational field Φ:

i. *The continuity equation*

$$\frac{\partial \rho}{\partial t} + \nabla \cdot (\rho \boldsymbol{v}) = 0\,, \tag{2.32}$$

ii. *the Euler equation*

$$\frac{\partial \boldsymbol{v}}{\partial t} + (\nabla \cdot \boldsymbol{v})\boldsymbol{v} = -\nabla\Phi - \frac{\nabla P}{\rho}\,, \tag{2.33}$$

iii. *the Poisson equation*

$$\triangle\Phi = 4\pi G\rho\,. \tag{2.34}$$

Having this set of equations at hand, we will proceed with the linear perturbation theory.

2.6.1 Linear structure formation

For small density perturbations we can linearise the hydrodynamic equations and decompose the quantities into a time-dependent background term and a perturbation term,

$$\rho(\boldsymbol{x},t) = \rho_{\mathrm{bg}}(t) + \delta\rho_(\boldsymbol{x},t)\,, \tag{2.35}$$
$$\boldsymbol{v}(\boldsymbol{x},t) = \boldsymbol{v}_{\mathrm{bg}}(t) + \delta\boldsymbol{v}(\boldsymbol{x},t)\,, \tag{2.36}$$
$$p(\boldsymbol{x},t) = p_{\mathrm{bg}}(t) + \delta p(\boldsymbol{x},t)\,, \tag{2.37}$$
$$\Phi(\boldsymbol{x},t) = \Phi_{\mathrm{bg}}(t) + \delta\Phi(\boldsymbol{x},t)\,, \tag{2.38}$$

where the quantities with the subscript 'bg' denote the homogeneous background components. The aforementioned density perturbations are characterised by the density contrast $\delta(\boldsymbol{x},t)$,

$$\delta(\boldsymbol{x},t) \equiv \frac{\rho(\boldsymbol{x},t) - \rho_{\mathrm{bg}}(t)}{\rho_{\mathrm{bg}}(t)}\,. \tag{2.39}$$

We define the *comoving peculiar velocity* $\boldsymbol{u} \equiv \boldsymbol{v}/a$ and the adiabatic *sound speed* $c_{\mathrm{s}}^2 \equiv \delta p/\delta\rho$. These relations are inserted into the set of Eqs (2.32), (2.33) and (2.34) to yield a second-order differential equation for the density contrast when leaving out terms which are not linear in the perturbations,

$$\ddot{\delta} + 2H\dot{\delta} - 4\pi G\rho_{\mathrm{bg}}\delta - \frac{c_{\mathrm{s}}^2}{a^2}\triangle\delta = 0\,. \tag{2.40}$$

Decomposing the density contrast into plane waves, inserting this in Eq. (2.40) and additionally transforming the equation to Fourier space reveals a more familiar form – an oscillator-like equation. In Fourier space the density contrast $\hat{\delta}(\boldsymbol{k},t)$ is written as

$$\hat{\delta}(\boldsymbol{k},t) = \int \mathrm{d}^3x\,\delta(\boldsymbol{x},t)\exp\left(\mathrm{i}\boldsymbol{k}\cdot\boldsymbol{x}\right). \tag{2.41}$$

We can identify a particular length scale called *Jeans length* $\lambda_{\mathrm{L}} \equiv c_{\mathrm{s}}\sqrt{\pi/(G\rho_{\mathrm{bg}})}$. Perturbations with length scales smaller than the Jeans length will oscillate, perturbations larger than the Jeans length will either grow or decay. On these scales the pressure term in Eq. (2.40) is neglected, which simplifies the equation as no spatial derivatives appear.

In the radiation-dominated era, however, we have to use relativistic fluid mechanics. This alters the shape of Eq. (2.40). We give here the perturbation equations for scales much larger than the Jeans length in both cases,

$$\text{matter-domination } (\Omega_{\mathrm{m}} = 1): \quad \ddot{\hat{\delta}} + 2H\dot{\hat{\delta}} = \frac{3}{2}H^2\hat{\delta}\,, \tag{2.42}$$
$$\text{radiation-domination:} \quad \ddot{\hat{\delta}} + 2H\dot{\hat{\delta}} = 4H^2\hat{\delta}\,. \tag{2.43}$$

With the ansatz $\hat{\delta}(\boldsymbol{k},t) \propto t^n$ we find for the matter-dominated case $n = 1, -2/3$ and in the radiation-dominated case $n = \pm 1$. If we omit the decaying solution, we get, using the proportionalities from Eq. (2.21),

$$\hat{\delta} \propto \begin{cases} a & \text{for matter-domination}\,, \\ a^2 & \text{for radiation-domination}\,. \end{cases} \tag{2.44}$$

The linear evolution of δ is then described by the *linear growth factor* D_+, which allows us to rewrite the density contrast as

$$\delta(\boldsymbol{x}, t) = \delta(\boldsymbol{x}, t_0) D_+(t) \,. \tag{2.45}$$

Considering the evolution-equation Eq. (2.40), we see that matter density drives the growth of structures whereas the Hubble expansion counteracts. In more general cases than $\Omega_\mathrm{m} = 1$, the evolution equation of the density contrast may only be solved numerically.

2.6.2 The power spectrum

Considering the scenario of cosmic single-field inflation, density perturbations are initially expected to follow a Gaussian distribution (e.g. see Liddle & Lyth, 2000) according to the central limit theorem. Deviations from this Gaussian random field, called *non-Gausianities*, are expected to be negligible if measurable at all (Komatsu et al., 2011). Such a Gaussian field is fully described by its mean and variance, whereas in our case the mean equals zero by construction, leaving us only in the need of the power spectrum of the density perturbations to fully describe their statistics.

The variance of δ defines the power spectrum $P(k)$, which only depends on the modulus of k due to isotropy,

$$\langle \hat{\delta}(\boldsymbol{k})\, \hat{\delta}^\star(\boldsymbol{k'}) \rangle \equiv (2\pi)^3 P(k)\, \delta_\mathrm{D}(\boldsymbol{k} - \boldsymbol{k'}) \,. \tag{2.46}$$

Dirac's delta distribution δ_D ensures that different k-modes are uncorrelated, otherwise the assumption of homogeneity would be violated. The star indicates the complex conjugate. In real space the correlation function ξ is defined as

$$\xi(y) \equiv \langle \delta(\boldsymbol{x})\, \delta(\boldsymbol{x} + \boldsymbol{y}) \rangle \quad \text{with} \quad y = |\boldsymbol{y}| \quad \text{due to isotropy.} \tag{2.47}$$

$\xi(y)$ is a measure for the coherence of the density contrast for all points separated by the distance modulus y. The variance σ^2 is then given by $\xi(y = 0)$,

$$\sigma^2 = 4\pi \int \frac{\mathrm{d}k\, k^2}{(2\pi)^3} P(k) \,. \tag{2.48}$$

By introducing a window function W_R and its Fourier-transform $\hat{W}_R$ and using Eq. (2.46) we can consider specific scales only

$$\sigma_R^2(a) \equiv \frac{1}{2\pi^2} \int \mathrm{d}k\, k^2\, D_+^2(a)\, \hat{W}_R^2\, P(k) \,. \tag{2.49}$$

Usually, a scale of $8\,\mathrm{Mpc}\,h^{-1}$ is considered using a top-hat filter function, defining the cosmological parameter σ_8 today.

The above discussion of the power spectrum is true for the matter-dominated era of the Universe in which density perturbations that enter the horizon either grow or decay. The picture changes if we take a closer look at perturbations small enough to enter the horizon in the radiation-dominated era. We inferred from Eq. (2.44) that perturbations in the density contrast grow proportional to a in the matter-dominated era, while they grow proportional to a^2 in the radiation-dominated era. But modes entering the horizon during the radiation-dominated era feel the radiation pressure and will be hindered from growing until the Universe is matter-dominated. Therefore, we can define a scale factor a_eq, corresponding to the time when radiation density and matter density were nearly equal. This also defines a specific length scale λ_eq (or wavenumber k_eq) equal to the Hubble radius at that time and further allows modes to grow normally with $k < k_\mathrm{eq}$ and hinders the growth of modes with $k > k_\mathrm{eq}$ nearly entirely. Modes entering the horizon at $a_\mathrm{enter} < a_\mathrm{eq}$ will start growing again once the Universe enters the matter-dominated phase.

2.6.3 Non-linear structure formation

Up to now we only considered first order density perturbations, requiring the density contrast to be rather small. However, structures in the Universe do exist, i.e. massive galaxy clusters with densities of $200 \times \rho_{\mathrm{bg}}$, heavily violating our previous assumption. Numerical simulations allow us to determine the shape of the power spectrum for non-linear structure formation which differs from the shape of the linear power spectrum. The reason for this is the following: In non-linear structure formation the transfer of power from larger to smaller scales is possible and necessary to form small scale structures– *mode coupling* occurs.

A glimpse into non-linear structure formation was developed by Zel'dovich (1970), explaining the cosmic fluid with a kinematical approach and decomposing it into particles following specific trajectories $\boldsymbol{r}$,

$$\boldsymbol{r}(t) = a(t)\boldsymbol{x} + b(t)\,\boldsymbol{f}(\boldsymbol{x})\,, \tag{2.50}$$

written as the sum of a universal expansion at position $\boldsymbol{x}$ and a peculiar motion described by the *displacement field* $\boldsymbol{f}(\boldsymbol{x}) = \boldsymbol{\nabla}\phi(\boldsymbol{x})$, being the gradient of some scalar field ϕ. The function $b(t)$ describes the time evolution of the displacement field. The derivative of Eq. (2.50) can be written in terms of the *deformation tensor* $\partial^2\phi/(\partial x_i \partial x_j)$. With this ansatz one obtains a relation between the density contrast δ and the eigenvalues of the deformation tensor and the ratio b/a. Even though this Zel'dovich approach is an approximation, it allows us to enrich our understanding of structure formation. Assuming a Gaussian random field for the perturbations of the gravitational field, one can infer the probability distribution for the eigenvalues of the deformation tensor. This results in the fact that the probability for any two eigenvalues to be equal is zero, ruling out isotropic collapse of structures. The anisotropic behaviour of gravitational collapse is observationally confirmed. Eventually, the Zel'dovich approximation fails once the trajectories of particles start to cross each other as their self-interaction was neglected.

2.6.4 Spherical collapse model

In the preceding section we motivated that isotropic collapse of structures is not possible. Nevertheless, the so-called *spherical collapse model* takes a closer look at collapsing spherical overdensities in a homogeneous background with density ρ_{bg}. This model is interesting, as one is capable to compute an analytic solution for the evolution of the density contrast (e.g. Padmanabhan (1993) or the thesis of Puchwein (2007)).

Considering only small scales in an *Einstein-de Sitter Universe*, a test particle at a physical distance r from the centre of the spherical overdense halo follows the Newtonian equation of motion,

$$\ddot{r} = -\frac{GM}{r^2}\,, \tag{2.51}$$

with the total mass $M = \frac{4}{3}\pi r^3\,\rho$. This equation could, if not focused on an *Einstein-de Sitter Universe*, contain contributions from the cosmological constant Λ. The integral of the equation of motion is given by

$$E = \frac{1}{2}\dot{r}^2 - \frac{GM}{r} \tag{2.52}$$

with the total energy E of the system. In the case of $E < 0$ the spherical halo first will expand together with the Universe reaching a maximum radius r_{ta} and eventually start to collapse at a turn-around time t_{ta}. A solution for the equation of motion in parametric form is given by

$$r = A\,(1 - \cos\theta)\,, \tag{2.53}$$

$$t = B\,(\theta - \sin\theta)\,, \tag{2.54}$$

which depends on the parameter θ. The constants A and B are related by

$$A^3 = B^2 GM\,. \tag{2.55}$$

Assuming $r = 0$ at $t = 0$ and inserting the above equation, Eqs. (2.53) and (2.54) yield

$$r = \frac{r_{\rm ta}}{2}\,(1 - \cos\theta)\,, \tag{2.56}$$

$$t = \frac{(t_{\rm ta}/2)^{3/2}}{\sqrt{GM}}\,(\theta - \sin\theta)\,. \tag{2.57}$$

As restricted to an *Einstein-de Sitter Universe*, we define the overdensity Δ,

$$\Delta \equiv \frac{\rho}{\rho_{\rm bg}} = \frac{9}{2}\frac{(\theta - \sin\theta)^2}{(1 - \cos\theta)^3}\,. \tag{2.58}$$

The density contrast $\delta \equiv \rho/\rho_{\rm bg} - 1$, see Eq. (2.39), to lowest order in t is then

$$\delta \approx \frac{3}{20}\left(\frac{6t}{B}\right)^{2/3} \propto a\,, \tag{2.59}$$

giving the linear density contrast $\delta_{\rm c}$. The proportionality is due to the fact that during matter-domination the scale factor a is proportional to $t^{2/3}$. For $\theta = \pi$ the overdensity is at its turn-around point and entirely collapses at $t = 2t_{\rm ta}$ (i.e. $\theta = 2\pi$) due to symmetry. This implies an infinite density for this model, but a realistic halo will rather settle in virial equilibrium, where the mean potential energy of the halo is twice the energy at the turn-around. Assuming energy conservation and considering that at turn-around the kinetic energy is zero, the halo will have a radius of $r_{\rm vir} = r_{\rm ta}/2$. At virialisation we find $\theta = 2\pi$ and thus the critical linear density contrast is $\delta_{\rm c} \approx 1.69$. Given the density contrast we can calculate the mean density $\rho_{\rm v}$

$$\rho_{\rm v} = \left(\frac{r_{\rm ta}}{r_{\rm vir}}\right)^3 [\delta(t_{\rm ta}) + 1]\;\rho_{\rm bg}(t_{\rm ta}) \approx 178\,\rho_{\rm bg}(t_{\rm vir})\,. \tag{2.60}$$

Following from Eq. (2.58) the overdensity is

$$\Delta_{\rm v} \approx 178\,. \tag{2.61}$$

A virialised overdense halo thus has a mean overdensity of about 178 times the background density. The linear density contrast $\delta_{\rm c}$ and the overdensity $\Delta_{\rm v}$ are used in cosmology to characterise dark matter halos. For a more general cosmology than the one considered here, an analytic calculation is not possible and one has to rely on numerical solutions.

2.7 Mass function

In the preceding section we sketched how structures in the Universe form and that they must not collapse isotropically. This allows us to ask the following question: Given that we observe structures, how is the distribution of dark matter halos with mass?

This distribution of halos over mass at a given redshift z is called *mass function* $n(M, z)$. Using the spherical collapse model from Section 2.6.4, Press & Schechter (1974) derived a formula for the mass function. It was reformulated by Bond et al. (1991) assuming halo formation to be a random walk process.

We define a characteristic length scale $R(M)$ of a halo with given mass M. A sphere filled with the average background density $\rho_{\rm bg} = \Omega_{\rm m}\,\rho_{\rm crit}$ has the mass

$$M = \frac{4}{3}\pi\,\Omega_{\rm m}\,\rho_{\rm crit}\,R^3\,, \tag{2.62}$$

which defines the length scale

$$R(M) = \left(\frac{3M}{4\pi\,\Omega_\mathrm{m}\,\rho_\mathrm{crit}} \right)^{1/3} . \tag{2.63}$$

To obtain the variance of the density contrast according to Eq. (2.49), the Gaussian density field is smoothed on the scale $R(M)$. This is achieved by convolving the density contrast with a window function W_R,

$$\delta_R(\boldsymbol{x}, z) \equiv \int \mathrm{d}^3 y\, \delta(\boldsymbol{y}, z)\, W_R(|\boldsymbol{x} - \boldsymbol{y}|) . \tag{2.64}$$

Once the linearly scaled density contrast δ_R is larger than a specific density contrast δ_c the overdense regions should collapse. For this barrier we take the result obtained with the spherical collapse model from Section 2.6.4. The probability to form such a halo with mass M is

$$P(\delta_R \geq \delta_\mathrm{c}) = \int_{\delta_\mathrm{c}(z)}^{\infty} \mathrm{d}\delta_R\, p(\delta_R) = \frac{1}{\sqrt{2\pi}\sigma_R(z)} \int_{\delta_\mathrm{c}(z)}^{\infty} \mathrm{d}\delta_R\, \exp\left[-\frac{\delta_R^2}{2\sigma_\mathrm{R}^2(z)} \right] = \frac{1}{2} \mathrm{erfc}\left[\frac{\delta_\mathrm{c}}{\sqrt{2}\sigma_R(z)} \right] , \tag{2.65}$$

with the complementary error function $\mathrm{erfc}(x) \equiv 1 - \mathrm{erf}(x)$. One main assumption of the *Press-Schechter formalism* is the following: The probability to find a δ_R above or equal to δ_c equals the fraction of the cosmic volume F with halos of mass M; we can write $P(\delta_\mathrm{R} \geq \delta_\mathrm{c}) = F(M)$. The halo distribution in dependence of mass is then

$$\frac{\partial F(M)}{\partial M} \mathrm{d}M = \frac{\partial P(\delta_R \geq \delta_\mathrm{c})}{\partial \sigma_R} \frac{\partial \sigma_R}{\partial R} \frac{\partial R}{\partial M} \mathrm{d}M . \tag{2.66}$$

The consideration by Press & Schechter (1974) as sketched above is missing a factor of two. The integral of Eq. (2.66) over all masses is not equal to one but to one half. The solution to this normalisation problem was found by Bond et al. (1991) by interpreting the halo formation as a random walk. It is then given by the cloud-in-cloud problem, i.e. the fact that haloes may contain smaller halos.

With the correct normalisation, which we insert here by hand without proof, we can divide the equation by the typical volume $V_\mathrm{m} = M/\rho_\mathrm{bg}$ of a halo,

$$n(M, z) = \frac{\partial^2 N}{\partial M\, \partial V} = \sqrt{\frac{2}{\pi}} \frac{\rho_\mathrm{bg}}{M} \frac{\delta_\mathrm{c}(z)}{D_+(z)\sigma_R} \left| \frac{\partial \ln \sigma_R^2}{\partial M} \right| \exp\left[-\frac{\delta_\mathrm{c}^2(z)}{2D_+^2(z)\sigma_R} \right] \tag{2.67}$$

with the total number N of halos. This function is called *Press-Schechter mass function* and gives a good insight into structure formation with redshift as the linear power spectrum of density fluctuations can be computed. The obtained mass function compares very well to those found by numerical simulations.

Even better results are found with a model that accounts for ellipsoidal collapse, which was developed by Sheth et al. (2001) and yields the following mass function:

$$n(M, z) = A \sqrt{\frac{2}{\pi}} \left(1 + \frac{1}{\nu^{2q}} \right) \frac{\rho_\mathrm{bg}}{M} \frac{\mathrm{d}\nu}{\mathrm{d}M} \exp\left(-\frac{\nu^2}{2} \right) , \tag{2.68}$$

where $\nu = \sqrt{\alpha}\, \delta_\mathrm{c} / [D_+(z]\, \sigma_\mathrm{R})$. For the remaining parameters, Sheth et al. (2001) find by comparison to numerical results: $A = 0.322$, $\alpha = 0.707$ and $q = 0.3$. The Press-Schechter mass function is obtained for $A = 1/2$, $\alpha = 1$ and $q = 0$. Further work by Jenkins et al. (2001) suggests values of $A = 0.353$, $\alpha = 0.73$ and $q = 0.175$.

To measure the mass function provides a good way to infer the normalisation of the power spectrum as the mass function depends exponentially on the variance of the density contrast. It also allows us to study the evolution of Ω_m as it enters in the mean background density ρ_bg.

Chapter 3

3 Galaxy clusters

Galaxy clusters are the most massive gravitationally bound objects in the Universe. In the scenario of hierarchical structure formation (see Section 2.6) they are the class of objects formed latest. As cold dark matter is expected to clump on all scales, massive objects such as galaxy clusters should have a broad spectrum of massive sublumps embedded (cf. Boylan-Kolchin et al., 2009; Dolag et al., 2009; Gao et al., 2004, 2011; Giocoli et al., 2010; Zentner et al., 2005). However, the distribution of cold dark matter in galaxy clusters should be least affected by baryonic physics, due to the long cooling time exceeding the *Hubble time*, of the baryonic matter (e.g. Duffy et al., 2010). Galaxy clusters are the class of objects best suited for testing expectations raised by simulations.

On the other hand, galaxy clusters provide information on the cosmological parameters, by means of their population statistics. As pointed out by different authors (e.g. Press & Schechter 1974; Jenkins et al. 2001; Sheth & Tormen 2002; Schuecker et al. 2003; Warren et al. 2006) cluster mass functions constrain the growth of structure, thus testing ΛCDM, see also Section 2.7.

In the light of these opportunities, many new data sets of cluster observables are becoming or will become available. As an extraordinary example we want to point out a specific *HST Multi-Cycle Treasury* programme – CLASH (**C**luster **L**ensing **A**nd **S**upernova survey with **H**ubble), in the course of which 25 X-ray luminous clusters have been observed in 16 bands with a wavelength coverage in the main survey from HST/WFC3/IR through HST/ACS optical to HST/WFC3/UVIS. All of these clusters will be analysed by the CLASH-Team (e.g. Coe et al., 2013; Postman et al., 2012; Umetsu et al., 2012; Zitrin et al., 2012, 2013), amongst other techniques, applying strong- and weak-lensing reconstructions of the mass distributions.

This chapter is dedicated to the constituents and the structure of galaxy clusters, as well as the different wavebands which clusters may be observed in.

3.1 Cluster structure

In the following we briefly discuss the current understanding of the structure of galaxy clusters. Examples for four massive galaxy clusters (Abell 383 (A), MACS 1149.6+2223 (B), Abell 2261 (C), MACS 1206.2-0847 (D)), are shown in Fig. 3.1. We further give an overview of the different components of galaxy clusters and how their generalised radial density distribution is phrased.

3.1.1 Constituents

First galaxies were observed in our close neighbourhood, though later galaxies in large agglomerations were found by Frederick William Herschel – giving galaxy clusters their name. Galaxies are prominent in the optical band. A cluster may host up to 1000 galaxies, each containing billions of stars. The

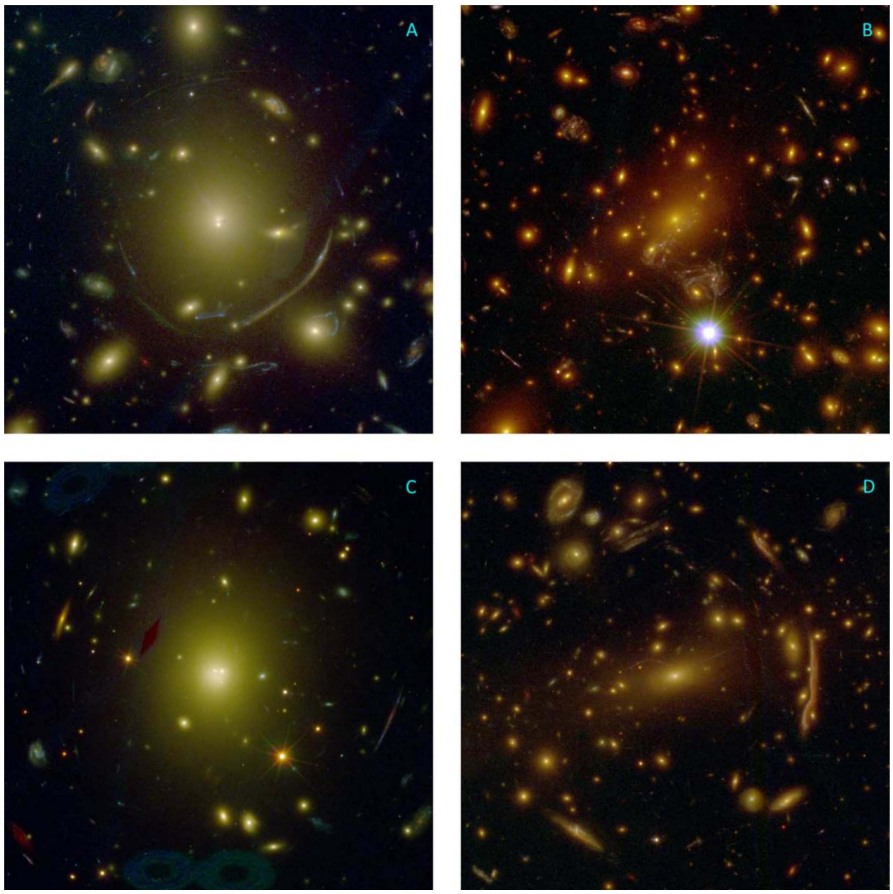

Figure 3.1: Images of strong gravitationally lensing galaxy clusters which are part of the CLASH project. Abell 383 (A), MACS 1149.6+2223 (B), Abell 2261 (C), and MACS 1206.2-0847 (D; Postman et al. 2012).

visible mass of the galaxies is responsible for roughly 1-2% of the total cluster's mass. Galaxies are used to infer their velocity dispersion (see Binney & Tremaine, 1988; Schneider, 2006a) first measured by Zwicky (1933, 1937) and now widely used to recover mass estimates of clusters, via the *Virial Theorem* (e.g. Diaferio et al., 2005).

Concerning the mass fraction the more massive component is the *intracluster medium* (ICM) with a mass fraction of roughly 10-15%. Mostly consisting of hydrogen and helium, the ICM radiates thermal bremsstrahlung revealing clusters in the X-ray band. Another signal the ICM is responsible for is the *thermal Sunyaev-Zel'dovich effect* (SZ) (Sunyaev & Zeldovich, 1980) measurable in the microwave regime. For many clusters the assumption of hydrostatic equilibrium is applicable thus the ICM directly probes the cluster potential well.

The total baryonic mass of clusters is therefore around 15%, thus galaxy clusters are missing a large amount of visible matter. The last 85% are due to *dark matter*, previously discussed in Section 2.4.

It was Zwicky (1937), who observed the Coma cluster which provided the first evidence for the presence of dark matter in galaxy clusters. Estimating the total mass of the *Coma cluster* much higher than inferred from optical measurements was a clear hint for a discrepancy, so far only solvable by a dark matter component.

3.1.2 NFW profile

Many numerical simulations have shown that gravitationally bound structures dominated by dark matter are following a universal density profile, first described by Navarro et al. (1996, 1997, hereafter

NFW). The NFW profile itself is flatter in the core, steepens around a scale radius r_s and then asymptotically approaches a double-logarithmic slope near -3 towards the virial radius r_{vir} (e.g. Jing & Suto 2000; Merritt et al. 2006; Navarro et al. 2004; Power et al. 2003; Moore et al. 1998, 1999 and Fig. 3.2).

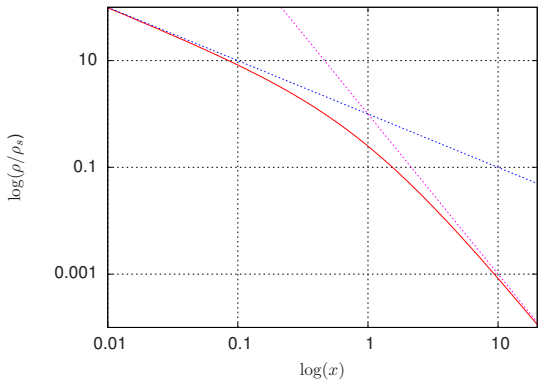

Figure 3.2: Double logarithmic plot of the NFW density profile for $x = r/r_s$. The asymptotic behaviour is illustrated by the dashed lines with slopes of -1 and -3.

The NFW profile is written as

$$\rho(r) = \frac{\rho_s}{(r/r_s)(1 + r/r_s)^2}, \tag{3.1}$$

with the characteristic density ρ_s of the halo.

Slight deviations from this universal profile exist, such as steeper slopes in the cluster core as pointed out by serval authors (Moore et al., 1999, 1998). Furthermore, recent findings by Power et al. (2003) and Navarro et al. (2004) argue for a slope probably depending on the halo mass. These efforts are combined in the generalised NFW profile (see Jing & Suto, 2002).

However, the above profile is spherically symmetric, clearly contradicting observed ellipsoidal cluster shapes, as a triaxial cluster shape fits better to real cluster observations (Allgood et al., 2006). This is also in agreement with the model of structure collapse according to the Zel'dovich approximation (see Section 2.6.3).

The importance of possible triaxial cluster shapes is also revealed by the following: The fraction r_{vir}/r_s is called the *concentration parameter* c and is found in simulations to depend only weakly on the mass M, decreasing with $\propto M^{-0.1}$ (see Navarro et al., 1996, 1997; Seljak, 2000; Bullock et al., 2001; Eke et al., 2001; Dolag et al., 2004; Shaw et al., 2006; Neto et al., 2007; Macciò et al., 2007; Duffy et al., 2008; Gao et al., 2008; Macciò et al., 2008; Zhao et al., 2009, for examples). The concentration parameter is frequently observed to be substantially different than theoretically expected. Particularly in strong gravitationally lensing clusters concentration parameters significantly higher than those found in numerical simulations have been claimed (Broadhurst et al., 2008; Coe et al., 2012, Fig. 14). Some of this discrepancy may be overcome, as pointed out by Sereno & Zitrin (2012), by taking cluster triaxiality into account, raising concerns on the universality of the spherical NFW profile. Other explanations to this problem of over-concentrated clusters exist. For instance, an introduced bias given by selection effects due to the used cluster sample (e.g. Meneghetti et al., 2010a).

3.2 Observing galaxy clusters

As mentioned before, clusters are observed in a multitude of different bands probing their different components. For a compilation of commonly used probes see Fig. 3.3, where we show that different methods probe different scales in galaxy clusters.

In this section we first want to describe the effect of gravitational lensing in the framework of general relativity. Thereafter, we will focus on the physical principles of the thermal SZ effect and the X-ray emission due to thermal bremsstrahlung.

For a detailed review on gravitational lensing we refer the interested reader to Bartelmann (2010), the thesis of Angrick (2011), notes of Meneghetti (2007) and the book by Schneider et al. (2006). Concerning the thermal SZ effect an excellent review is provided by Birkinshaw (1999), as well as for X-ray emission by Sarazin (1986); Sarazin & Surdin (1988) and in the recent publication by Ettori et al. (2013).

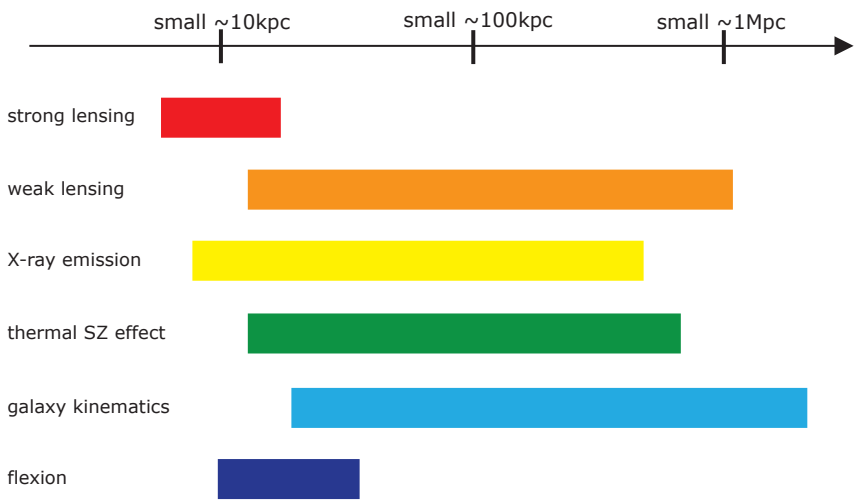

Figure 3.3: Different methods probe different scales in galaxy clusters and thus also their mass distribution. The picture further shows a possible range for flexion measurements (credits: M. Bartelmann).

3.2.1 Gravitational lensing

A method where observations of galaxies are crucial is the effect of *gravitational lensing*, even though not the cluster members but rather the background galaxies are the ones of interest here. Gravitational lensing effects give an insight into the surface-mass density or the effective lensing potential of the cluster.

According to general relativity a propagating ray of light is bent towards massive objects by the gravitational potential, nearly analogues to a convex glass lens. Such a propagating ray may be the light emitted by a background galaxy, which in the following will be called *source*. The source is located behind a massive object, e.g. a galaxy cluster, acting as the *lens*. This lensing effect leads to an apparent position change of the source in the plane of the sky, as well as to distortions depending on the alignment of the lens and source and the strength of the lens itself. Therefore, one can distinguish between two different regimes:

Strong lensing leads to strong image distortions, multiple images, giant arcs or so called *Einstein rings*. These visually striking effects occur whenever the source is exactly behind the lens (Einstein rings) or near the centre (strong distortions, multiple images and giant arcs, see also Fig. 3.1).

Weak lensing in comparison is only responsible for minor distortions of the source leading to small changes in the ellipticity of the background galaxies. This in turn implies a problem in measuring the effects of weak lensing as galaxies have intrinsic ellipticities. It only allows statistical statements on the weak-lensing signal as the intrinsic ellipticity is expected to vanish if one averages over a large sample of lensed galaxies.

Lens equation

In the following we want to present the framework of gravitational lensing in the so-called *thin-lens-approximation* as the distances are large in comparison to the size of the lens and the background source. The distance between the observer and the lens is called D_d, at this distance the mass of the lens is projected onto a plane – the *lens plane*. It describes the plane in the sky where lensing is assumed to occur. The distance from the lens plane to the *source plane* is called D_ds and the distance from the observer to the source plane D_s. As distances are angular diameter distances, D_s is generally not the sum of D_ds and D_d (see also Section 2.5). The assumed geometry of the lensing system is depicted in Fig. 3.4, defining the angular position $\boldsymbol{\beta}$ and the apparent position angle $\boldsymbol{\theta}$ of the source,

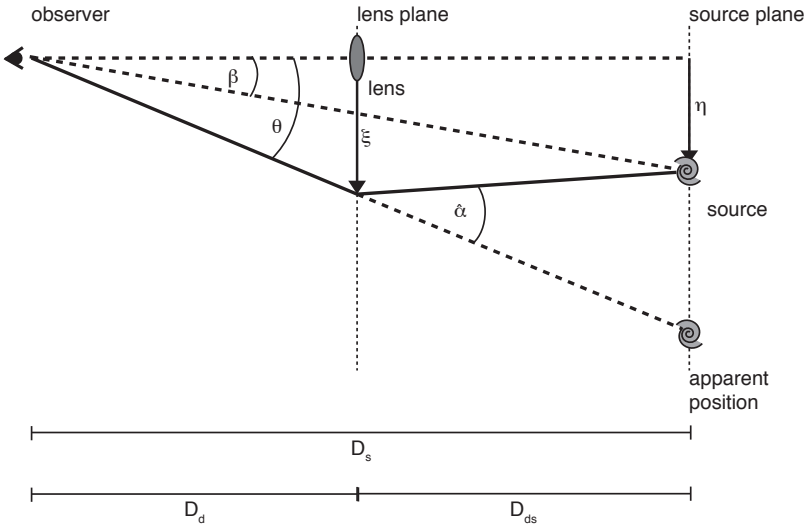

Figure 3.4: Geometrical description in the thin-lens-approximation, defining the source plane, lens plane and the impact parameter $\boldsymbol{\xi}$, as well as the position angles $\hat{\boldsymbol{\alpha}}$, $\boldsymbol{\beta}$ and $\boldsymbol{\theta}$ (see text).

lying at the distance $\boldsymbol{\eta} = \boldsymbol{\beta} D_\mathrm{s}$ in the source plane. From Fig. 3.4 we further define the impact parameter as $\boldsymbol{\xi} = \boldsymbol{\theta} D_\mathrm{d}$. As all the angles are expected to be small, simple geometric considerations lead to the so called *lens equation*

$$\boldsymbol{\eta} = D_\mathrm{ds} \hat{\boldsymbol{\alpha}} = \frac{D_\mathrm{s}}{D_\mathrm{d}} \boldsymbol{\xi} \tag{3.2}$$

with the deflection angle $\hat{\boldsymbol{\alpha}}$. We can further introduce the *reduced deflection angle*

$$\boldsymbol{\alpha}(\boldsymbol{\theta}) \equiv \frac{D_\mathrm{ds}}{D_\mathrm{s}} \hat{\boldsymbol{\alpha}}(\boldsymbol{\theta}) \,. \tag{3.3}$$

With it, in combination with the position angles $\boldsymbol{\beta}$ and $\boldsymbol{\theta}$, the lens equation can be simplified to

$$\boldsymbol{\beta} = \boldsymbol{\theta} - \boldsymbol{\alpha}(\boldsymbol{\theta}) \,. \tag{3.4}$$

Lensing Potential

From the linearised field equations Eq. (2.1) we can retrieve the deflection angle, which points towards the mass, as

$$\hat{\boldsymbol{\alpha}} = \frac{4GM}{c^2} \frac{\boldsymbol{\xi}}{|\boldsymbol{\xi}|^2} \,. \tag{3.5}$$

This is twice the value expected from Newtonian physics where the time-time part of the metric is neglected.

Furthermore, an object acting as a gravitational lens can be described with the three-dimensional mass density $\rho(\boldsymbol{r})$ with $\boldsymbol{r} = (\xi_1, \xi_2, r_3)$, such that r_3 points along the line-of-sight to the lens plane. Giving this mass distribution as the sum of point masses allows us to replace the mass in Eq. (3.5) by an integration over the density,

$$\hat{\alpha}(\boldsymbol{\xi}) = \frac{4G}{c^2} \int \mathrm{d}^3 r' \, \rho(\boldsymbol{r'}) \, \frac{\boldsymbol{\xi} - \boldsymbol{\xi}'}{|\boldsymbol{\xi} - \boldsymbol{\xi}'|^2} = \frac{4G}{c^2} \int \mathrm{d}^2 \xi' \, \Sigma(\boldsymbol{\xi}') \, \frac{\boldsymbol{\xi} - \boldsymbol{\xi}'}{|\boldsymbol{\xi} - \boldsymbol{\xi}'|^2} \,. \tag{3.6}$$

The line-of-sight projection of this density is the so-called *surface-mass density* $\Sigma(\boldsymbol{\xi})$. This further defines the *convergence* κ as the dimensionless ratio of the surface-mass density and the *critical mass*

density $\Sigma_{\rm crit}$, characterising the geometry of the lens system,

$$\kappa(\boldsymbol{\theta}) \equiv \frac{\Sigma(D_{\rm d}\boldsymbol{\theta})}{\Sigma_{\rm crit}}\,, \tag{3.7}$$

$$\Sigma_{\rm crit} \equiv \frac{c^2}{4\pi G}\,\frac{D_{\rm s}}{D_{\rm d}D_{\rm ds}}\,. \tag{3.8}$$

There is a sufficient condition for the convergence ($\kappa \geq 1$) in order to have strong lensing. Given the convergence, we rewrite Eq. (3.6) introducing the *lensing potential* ψ

$$\begin{aligned}\alpha(\boldsymbol{\theta}) &= \frac{1}{\pi}\int \mathrm{d}^2\boldsymbol{\theta}'\,\kappa(\boldsymbol{\theta})\,\frac{\boldsymbol{\theta}-\boldsymbol{\theta}'}{|\boldsymbol{\theta}-\boldsymbol{\theta}'|^2} \\ &= \nabla\psi \quad \text{with} \quad \psi \equiv \int \mathrm{d}^2\boldsymbol{\theta}'\,\kappa(\boldsymbol{\theta})\,\ln|\boldsymbol{\theta}-\boldsymbol{\theta}'|\,.\end{aligned} \tag{3.9}$$

In the last equation we used

$$\nabla \ln|\boldsymbol{\theta}-\boldsymbol{\theta}'| = \frac{\boldsymbol{\theta}-\boldsymbol{\theta}'}{|\boldsymbol{\theta}-\boldsymbol{\theta}'|^2}\,. \tag{3.10}$$

Defined according to Eq. (3.9), the lensing potential is the scaled line-of-sight projection of the Newtonian potential Φ of the given mass distribution,

$$\psi(\boldsymbol{\theta}) = \frac{2}{c^2}\,\frac{D_{\rm ds}}{D_{\rm s}D_{\rm d}}\int \mathrm{d}r_3\,\Phi(D_{\rm d}\boldsymbol{\theta}, r_3)\,, \tag{3.11}$$

and satisfies Poisson's equation in two dimensions,

$$\triangle\psi = 2\kappa\,. \tag{3.12}$$

Convergence and shear

The observed image of a background source may either get enlarged or reduced in size and additionally distorted. But the lensing process does not create or destroy photons, conserving the surface brightness of the source. If the source is small compared to the extent of the lens, the mapping $\boldsymbol{\beta} \mapsto \boldsymbol{\theta}$ can be linearised around a point $\boldsymbol{\theta}_0$ using the local Jacobian A

$$\boldsymbol{\beta} = \boldsymbol{\beta}_0 + A(\boldsymbol{\theta}_0)\cdot[\boldsymbol{\theta}-\boldsymbol{\theta}_0]\,, \tag{3.13}$$

where we use the angle between the line-of-sight and the centre of the source $\boldsymbol{\beta}_0$, as well as the angle between the line-of-sight and the centre of the image $\boldsymbol{\theta}_0$. The Jacobian can be rewritten in terms of the lensing potential, further introducing the *shear* γ, with its two components γ_1 and γ_2,

$$A = \left(\delta_{ij} - \frac{\partial^2\psi}{\partial\theta_i\partial\theta_j}\right) \equiv \begin{pmatrix} 1-\kappa-\gamma_1 & -\gamma_2 \\ -\gamma_2 & 1-\kappa+\gamma_1 \end{pmatrix}. \tag{3.14}$$

The shear components and the convergence in terms of the lensing potential are then given as combinations of second order derivatives of the lensing potential,

$$\gamma_1 = \frac{1}{2}\left(\frac{\partial^2\psi}{\partial\theta_1^2} - \frac{\partial^2\psi}{\partial\theta_2^2}\right), \qquad \gamma_2 = \frac{\partial^2\psi}{\partial\theta_1\,\partial\theta_2}\,, \qquad \kappa = \frac{1}{2}\left(\frac{\partial^2\psi}{\partial\theta_1^2} + \frac{\partial^2\psi}{\partial\theta_2^2}\right). \tag{3.15}$$

We can finally define the magnification as the inverse of the determinant of the Jacobian

$$\mu \equiv |\det A|^{-1} = \left|\det\left(\frac{\partial\beta_i}{\partial\theta_j}\right)\right|^{-1} = \frac{1}{(1-\kappa)^2 - |\gamma|^2}\,. \tag{3.16}$$

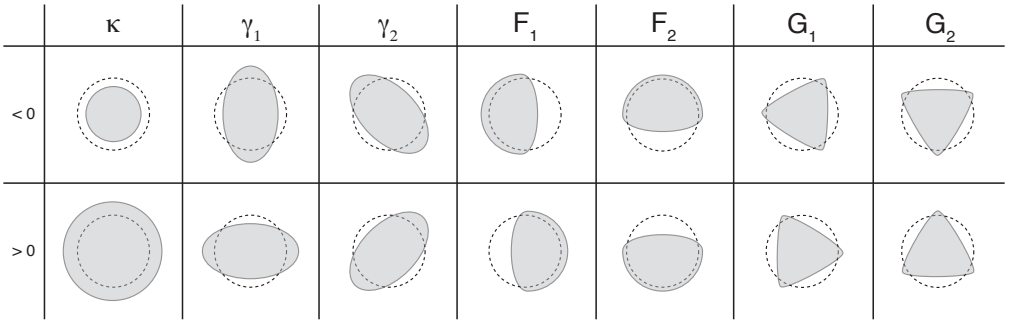

Figure 3.5: Distortions caused by the convergence, shear components and the components of F- and G-flexion. The round shape of the unlensed source is indicated by the dashed circles.

Going back to Eq. (3.14), a factor $(1-\kappa)$ can be separated from the matrix. This defines the *reduced shear* g with its components g_1 and g_2,

$$A = (1-\kappa)\begin{pmatrix} 1-g_1 & -g_2 \\ -g_2 & 1+g_1 \end{pmatrix}. \tag{3.17}$$

The reduced shear is an observable, thus only image distortions as a combination of shear and convergence are measurable. The prefactor $(1-\kappa)$ is acting as a homogenous distortion only changing the apparent size of the source.

The intrinsic ellipticity $\epsilon^{(s)}$ of galaxies is assumed to be randomly distributed and its contribution to the observed signal should average out for a large number of observed galaxies in the same region if correlations between nearby galaxies are not present. The transition from image ellipticity ϵ to source ellipticity $\epsilon^{(s)}$ is, as a function of the reduced shear $g(\boldsymbol{\theta})$, depending on the angular position $\boldsymbol{\theta}$ (see Seitz & Schneider, 1997),

$$\epsilon^{(s)} = \begin{cases} \dfrac{\epsilon - g(\boldsymbol{\theta})}{1 - g^\star(\boldsymbol{\theta})\epsilon} & \text{for } |g(\boldsymbol{\theta})| \leq 1\,, \\[2ex] \dfrac{1 - g(\boldsymbol{\theta})\epsilon^\star}{\epsilon^\star - g^\star(\boldsymbol{\theta})} & \text{for } |g(\boldsymbol{\theta})| > 1\,. \end{cases} \tag{3.18}$$

The inverse transformation from the image ellipticity to the source ellipticity is obtained by interchanging $\epsilon^{(s)}$ with ϵ and g with $-g$. The reduced shear implicitly depends on the redshift z of the source, but by introducing the so-called *cosmological weight* $Z(z)$ we can factorise the redshift dependence as

$$\kappa(\boldsymbol{\theta}, z) = Z(z)\kappa(\boldsymbol{\theta}) \quad \text{and} \quad \gamma(\boldsymbol{\theta}, z) = Z(z)\gamma(\boldsymbol{\theta})\,. \tag{3.19}$$

The function $Z(z)$ is according to Bartelmann & Schneider (2001), for a source at distance D_s and the distance D_{ds} between the lens and the source, given as

$$Z(z) = \frac{D_\infty D_{ds}}{D_{d\infty} D_s}\,\Theta(z - z_d)\,, \tag{3.20}$$

where the theta-function ensures that only sources behind the lens, located at redshift z_d, are taken into account for lensing effects. The function can be scaled to an arbitrary fiducial redshift. However, as the angular diameter distance is finite for infinite redshift, a convenient choice is to scale the quantities to a fiducial source redshift of infinity. This choice defines the angular diameter distances D_∞ between the observer and infinity and $D_{d\infty}$ between the lens and infinity.

The expectation value of the ellipticity $\langle\epsilon\rangle$ is then

$$\langle\epsilon\rangle = \begin{cases} \dfrac{Z(z)\gamma(\boldsymbol{\theta})}{1 - Z(z)\kappa(\boldsymbol{\theta})} & \text{for } |g(\boldsymbol{\theta}, z)| \leq 1\,, \\ \dfrac{1 - Z(z)\kappa(\boldsymbol{\theta})}{Z(z)\gamma^{\star}(\boldsymbol{\theta})} & \text{for } |g(\boldsymbol{\theta}, z)| > 1\,. \end{cases} \tag{3.21}$$

From Eq. (3.13) we derived the distortions up to first order giving us the shear components. Including the second order would reveal the so called *F-flexion* and *G-flexion*. Flexion is responsible for curvature and other distortions in the images. Figure 3.5 gives an overview how the introduced quantities act on a circular source.

3.2.2 Thermal SZ effect

The thermal Sunyaev-Zel'dovich effect is caused by hot electrons in the intracluster plasma that inversely Compton scatter the much less energetic photons of the CMB to higher energies. The SZ effect thus slightly distorts the CMB spectrum away from its Planckian shape.

Seen against the CMB, clusters cast shadows below 217 GHz and shine at frequencies above. Massive galaxy clusters can be identified by this characteristic spectral appearance at centimetre to millimetre wavelengths if the angular resolution of the telescope is of order $1'$ or better.

The Compton-y parameter, depending on the angular position $\boldsymbol{s}$ and the line-of-sight position z, is quantified by

$$y(\boldsymbol{s}) = \frac{k_\mathrm{B}}{m_\mathrm{e}c^2}\sigma_\mathrm{T}\int \mathrm{d}z\, T(\boldsymbol{s}, z) n_\mathrm{e}(\boldsymbol{s}, z)\,, \tag{3.22}$$

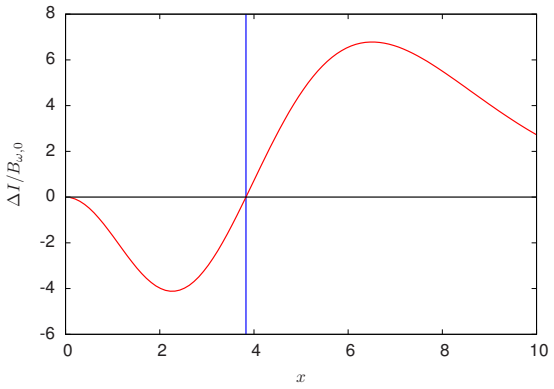

Figure 3.6: The relative intensity change of the CMB due to the thermal SZ effect as a function of $x = \hbar\omega/k_\mathrm{B}T_\mathrm{CMB}$. For values smaller than $x = 3.83$, corresponding to a frequency of 217 GHz, the change is negative and for larger values positive.

which compares the mean thermal energy $k_\mathrm{B}T$ of the electrons, with the Boltzmann constant k_B, to their rest energy $m_\mathrm{e}c^2$ of the electrons and multiplies their ratio with the *Thomson cross section* σ_T and the electron number density n_e. Thus thermal SZ effect is characterised by the scattering probability $n_\mathrm{e}\sigma_\mathrm{T}\,\mathrm{d}z$ and the mean relative energy change $k_\mathrm{B}T/(m_\mathrm{e}c^2)$. By Compton-upscattering, the specific intensity of the CMB seen through a galaxy cluster changes by

$$\frac{\Delta I_\mathrm{SZ}(\boldsymbol{s})}{B_\omega(T)} = g(x)y(\boldsymbol{s}) \tag{3.23}$$

relative to the Planck spectrum $B_\omega(T)$ of the CMB, where

$$x = \frac{\hbar\omega}{k_\mathrm{B}T_\mathrm{CMB}} \tag{3.24}$$

is the photon energy in units of the mean thermal energy of the CMB. The function $g(x)$ describes the frequency and temperature dependence of the thermal SZ effect,

$$g(x) = \frac{x^4\mathrm{e}^x}{\mathrm{e}^x - 1}\left(x\frac{\mathrm{e}^x + 1}{\mathrm{e}^x - 1} - 4\right). \tag{3.25}$$

This dependence is shown in Fig. 3.6, which has no intensity change at a frequency of 217 GHz. Note, the thermal SZ effect is independent of the redshift of the cluster, which is a most interesting feature.

It arises due to the fact that in the thermal SZ effect depends on the CMB temperature in the rest frame of the cluster. At the cluster's redshift the thermal SZ effect has a different behaviour with frequency, but after the CMB photons passed the cluster they are further redshifted as they travel towards the observer, which renders the thermal SZ effect independent of redshift.

From Eq. (3.23), we can write the specific intensity as the projection of the effective pressure $P(\boldsymbol{s}, z)$ along the line-of-sight,

$$\frac{\Delta I_{\mathrm{SZ}}(\boldsymbol{s})}{B_\omega(T)} = \int \mathrm{d}z\, P(\boldsymbol{s}, z)\,, \tag{3.26}$$

defining the effective pressure as

$$P(\boldsymbol{s}, z) \equiv P_0\, T(\boldsymbol{s}, z) n_{\mathrm{e}}(\boldsymbol{s}, z)\,, \tag{3.27}$$

$$P_0 = g(x)\frac{k_{\mathrm{B}}\sigma_{\mathrm{T}}}{m_{\mathrm{e}}c^2} T_0 \rho_0\,. \tag{3.28}$$

Quantities with a subscript '0' refer to an arbitrary but fixed radius, for instance the centre of the cluster, provided the density is finite there.

Due to the finite telescope resolution, the observable quantity is not the Compton-y parameter or the specific intensity change from Eq. (3.23), but rather the beam-convolved quantities. The Compton-y profile convolved with a beam profile $b(\boldsymbol{s})$ is

$$\bar{y}(\boldsymbol{s}) \equiv \int \mathrm{d}^2 s'\, y(\boldsymbol{s}')\, b(\boldsymbol{s} - \boldsymbol{s}')\,. \tag{3.29}$$

Current state-of-the-art instruments like *Bolocam* have an effective beam of almost $1'$. In such cases we would need to include the beam convolution in our calculations. However, future SZ observations will reach an angular resolution much better than the angular resolution that can be achieved with potential reconstructions based on gravitational lensing: For instance, assuming 50 background galaxies per arcmin^2 and averaging over 20 galaxies to obtain a sufficiently robust weak-lensing signal, the resolution of a weak-lensing map corresponds to $\approx 35''$. Beam profiles of modern thermal SZ observations will be narrower than that, allowing us to approximate the beam $b(\boldsymbol{s})$ in (3.29) by a Dirac delta distribution. In such a case the beam convolution can in fact be ignored for our purposes. An example for such a telescope is the *Atacama Large Millimeter/submillimeter Array* (ALMA) with a beam size of $14.95''$ at a wavelength of 0.85 mm (Lundgren, 2013).

To illustrate current thermal SZ and X-ray observations we show in Fig. 3.7 an overview of the *Coma cluster* in different regimes. The image shows the thermal SZ effect observed with Planck, the X-ray emission (see Section 3.2.3) observed with ROSAT and additionally overlaid optical images.

SZ effect as a tracer for the lensing potential

We now consider the ICM in the gravitational potential well Φ of a massive galaxy cluster including the dark matter halo. At least in or near hydrostatic equilibrium the density and temperature of the gas are fully characterised by the Newtonian potential. Therefore, we begin with the hydrostatic equation

$$\boldsymbol{\nabla} P = -\rho \boldsymbol{\nabla} \Phi\,, \tag{3.30}$$

and assume that the gas satisfies the polytropic relation

$$\frac{P}{P_0} = \left(\frac{\rho}{\rho_0}\right)^\gamma\,, \tag{3.31}$$

with an effective adiabatic index γ. Eq. (3.30) is immediately integrated to give

$$\left(\frac{\rho}{\rho_0}\right)^{\gamma-1} = \frac{\gamma - 1}{\gamma}\frac{\rho_0}{P_0}(\Phi_{\mathrm{cut}} - \Phi)\,, \tag{3.32}$$

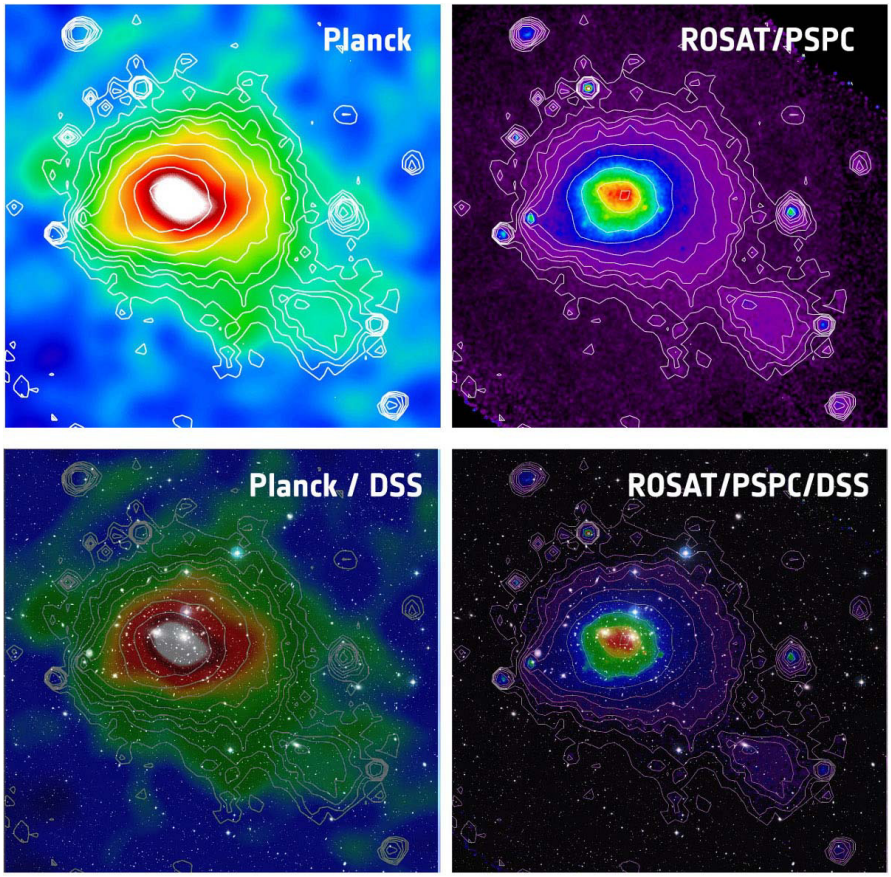

Figure 3.7: Image of the thermal SZ effect observed with Planck, the X-ray emission observed with ROSAT, and additionally overlaid optical images.

where quantities with a subscript '0' refer to an arbitrary but fixed radius r_0. For practical reasons we introduce a cutoff radius $r_{\mathrm{cut}} > r_0$ and fix the potential such that $\Phi_{\mathrm{cut}} = \Phi(r_{\mathrm{cut}})$.

For $\gamma > 1$ and a density profile that decreases monotonically, $\Phi(r)$ can be arranged to be negative for $r < r_0$ by the structure of Eq. (3.32). Therefore ρ remains positive and semi-definite. The quantity

$$\gamma \frac{P_0}{\rho_0} = c_{\mathrm{s},0}^2 \,, \tag{3.33}$$

appearing in Eq. (3.32) is the squared sound speed at the cutoff radius. For convenience, we introduce the dimensionless potential

$$\varphi = \frac{\gamma - 1}{c_{\mathrm{s},0}^2} \left(\Phi_{\mathrm{cut}} - \Phi\right) \,, \tag{3.34}$$

and obtain a relation between the gas density and the dimensionless potential

$$\rho = \rho_0 \, \varphi^{1/(\gamma-1)} \,. \tag{3.35}$$

The temperature of an ideal gas is given by

$$T = \frac{\bar{m}}{k_{\mathrm{B}}} \frac{P}{\rho} \,, \tag{3.36}$$

where $\bar{m}$ is the mean gas-particle mass. If the gas is in in thermal equilibrium and the cluster settled in virial equilibrium we can relate the temperature to the potential φ by

$$T = \frac{\bar{m}}{k_{\mathrm{B}}} \frac{P_0}{\rho_0} \varphi = T_0 \, \varphi \,. \tag{3.37}$$

Equations (3.35) and (3.37) are fundamental for the key idea of our work and will be widely used throughout the next chapters.

Combining Eqs. (3.22), (3.35) and (3.37), the Compton-y parameter can be rewritten in terms of the dimensionless potential φ as

$$y(\boldsymbol{s}) = \frac{k_\mathrm{B}\sigma_\mathrm{T}}{m_\mathrm{e}c^2}\, T_0\rho_0 \int \mathrm{d}z\, \varphi^\eta(\boldsymbol{s}, z)\,, \tag{3.38}$$

with the exponent $\eta = \gamma(\gamma-1)^{-1}$. For inferred polytropic indices, $1.1 \lesssim \gamma \lesssim 1.2$ (Finoguenov et al., 2001), the exponent η is a large number, $6 \lesssim \eta \lesssim 11$. Equation (3.38) in terms of the specific intensity change, combined with Eq. (3.26) relates the effective pressure $P(\boldsymbol{r})$ and the gravitational potential $\varphi(\boldsymbol{r})$,

$$\begin{aligned}\frac{\Delta\bar{I}_\mathrm{SZ}(\boldsymbol{s})}{B_\omega(T)} &= g(x)\,\frac{k_\mathrm{B}\sigma_\mathrm{T}}{m_\mathrm{e}c^2}\, T_0\rho_0 \int \mathrm{d}z\, \varphi^\eta(\boldsymbol{s}, z) \\ &= \int \mathrm{d}z\, P(\boldsymbol{s}, z)\,.\end{aligned} \tag{3.39}$$

leaving us with

$$P(\boldsymbol{s}, z) \propto \varphi^\eta(\boldsymbol{s}, z)\,. \tag{3.40}$$

With these equations we can define our method for recovering the projected gravitational potential:

(1) By deprojection of the measured relative specific intensity change $\Delta I_\mathrm{SZ}/B_\omega(T)$, we find an estimate for the three-dimensional effective pressure P using Eq. (3.26).

(2) Next, we use Eq. (3.40) to find an estimate $\tilde{\varphi}$ for the scaled gravitational potential φ,

$$\tilde{\varphi}(\boldsymbol{s}, z) = \left[\frac{P(\boldsymbol{s}, z)}{P_0}\right]^{1/\eta}\,. \tag{3.41}$$

(3) The estimate $\tilde{\varphi}$ of the three-dimensional potential is then projected along the line-of-sight according to Eq. (3.11) to find an estimate $\tilde{\psi}$ which is proportional to the two-dimensional lensing potential ψ,

$$\tilde{\psi}(\boldsymbol{s}) = \int \mathrm{d}z\, \tilde{\varphi}(\boldsymbol{s}, z)\,. \tag{3.42}$$

Since η is large, the exponent $1/\eta$ is a small number, which is a most welcome property of Eq. (3.40). Fluctuations in the estimate $\tilde{P}$ of the deprojected effective pressure will be substantially smoothed that way.

3.2.3 X-ray emission

As mentioned above, galaxy clusters host a large amount of hot plasma. The ICM reaches temperatures of $10^7 - 10^8$ K. This ICM contains a significant amount of metals, with a metallicity of up to 30% of the solar metallicity. Within this plasma electrons get accelerated in the electromagnetic field of other ions, leading to the emission of thermal bremsstrahlung, which is a free-free radiation. Given this gas mixture, the spectra of galaxy clusters are thus composed of a continuum emission due to thermal bremsstrahlung and a line spectrum due to the line emission of heavy ions. Figure 3.8 shows the difference between zero metallicity and 25% of the solar metallicity for two different temperatures. Even though metals change the spectrum significantly in some regions, for this work the line emission may be neglected as the temperatures are so high that line emission is subdominant.

Detailed derivations of the bremsstrahlung spectrum may be found in numerous textbooks, the most recent one by Bartelmann (2013), giving the emissivity of non-relativistic thermal bremsstrahlung,

$$j_X(\omega) = \frac{16\pi^2}{3\sqrt{3}} \frac{Z^2 e^6 n_\mathrm{i} n_\mathrm{e}}{m_\mathrm{e}^2 c^3} \bar{g}_\mathrm{ff}(\omega) \sqrt{\frac{2m_\mathrm{e}}{\pi k_\mathrm{B} T}} \times \exp\left(-\frac{\hbar\omega}{k_\mathrm{B} T}\right), \tag{3.43}$$

where e is the electron charge and m_e electron mass, n_i and n_e are the ion and electron particle densities. Z is the atomic number and $\hbar$ the reduced Planck constant. The *Gaunt factor* $\bar{g}_{\mathrm{ff}(\omega)}$ is sufficiently approximated by 1. Integrating Eq. (3.43) over all frequencies yields the total emissivity

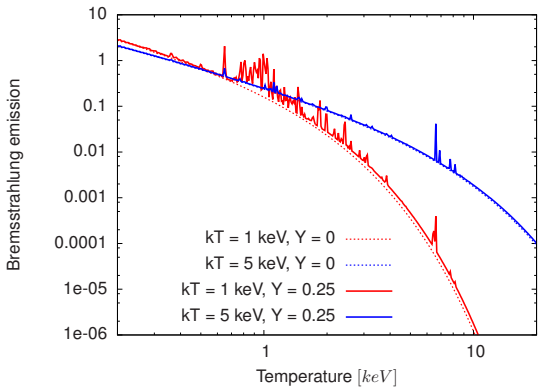

Figure 3.8: Spectrum of thermal bremstrahlung for two different temperatures with and without metallicities ($Y = 0$). The spectra were produced with the *xspec* software package using a Raymond-Smith plasma model and kindly provided by M. Bartelmann.

$$j_X = \frac{16\pi^2}{3\sqrt{3}} \frac{Z^2 e^6 n_\mathrm{i} n_\mathrm{e}}{m_\mathrm{e}^2 c^3} \sqrt{\frac{2m_\mathrm{e}}{\pi}} \frac{\sqrt{k_\mathrm{B} T}}{\hbar}\,. \tag{3.44}$$

We now replace the particle densities with the gas density ρ, introducing the mean particle mass $\bar{m}$

$$\begin{aligned} j_X &= \frac{16\pi^2}{3\sqrt{3}} \frac{Z^2 e^6}{m_\mathrm{e}^2 \bar{m}^2 c^3 \hbar} \sqrt{\frac{2m_\mathrm{e}}{\pi}} \rho^2 \sqrt{k_\mathrm{B} T} \\ &= C\,\rho^2 T^{1/2} \end{aligned} \tag{3.45}$$

with the bremsstrahlung constant C. For a fully ionised hydrogen gas we find $C \approx 143.6/\hbar$. The resulting X-ray emission may be observed with space-based telescopes like the *Chandra X-ray Observatory* (Chandra) or the *X-ray Multi-Mirror Mission - Newton* (XMM) in energy ranges between 0.2 - 12 keV.

However, telescopes only observe the line-of-sight projection of the three-dimensional emissivity, the surface brightness S_x. The surface brightness is expressed in the angular coordinate $\boldsymbol{s}$ by a line-of-sight integral,

$$\begin{aligned} S_x(\boldsymbol{s}) &= \int \mathrm{d}z\, j_X(\boldsymbol{s}, z) \\ &= C \int \mathrm{d}z\, \rho^2(\boldsymbol{s}, z)\, T^{1/2}(\boldsymbol{s}, z)\,. \end{aligned} \tag{3.46}$$

X-ray emission as a tracer for the lensing potential

The reader may notice that Eq. (3.46) has the same appearance as Eq. (3.22), a line-of-sight integral of the density and the temperature with given exponents. This allows us to link the surface brightness (equivalently the specific intensity) to the underlying gravitational potential of the cluster. Since the frequency-integrated emissivity due to bremsstrahlung is given by Eq. (3.45) it can be related to the potential by using the expression for the density and the temperature from Section 3.2.2, revealing

$$j_X = C\rho_0^2 T_0^{1/2} \varphi^{\hat{\eta}} \quad \text{with} \quad \hat{\eta} = \frac{3+\gamma}{2(\gamma-1)}\,. \tag{3.47}$$

For observed effective adiabatic indices the exponent $\hat{\eta}$ is again a large number, $10 \lesssim \hat{\eta} \lesssim 20$.

Equation (3.47), together with the fact that ordinary lensing effects are determined by second-order derivatives of the projected Newtonian potential, suggests the following algorithm for combining X-ray and lensing data, in analogy to the method outlined for the thermal SZ effect in Sec. 3.2.2:

(1) By deprojection of an X-ray surface brightness map S_X we find an estimate $\tilde{j}_X$ for the X-ray emissivity.

(2) We then use Eq. (3.47) to infer an estimate

$$\tilde{\varphi} = \left(\frac{\tilde{j}_X}{C\rho_0^2 T_0^{1/2}} \right)^{1/\hat{\eta}} \tag{3.48}$$

for the three-dimensional, scaled Newtonian potential φ.

(3) By projecting $\tilde{\varphi}$ along the line-of-sight we obtain an estimate $\tilde{\psi}$ for the two-dimensional potential, which is proportional to the lensing potential and can thus directly be combined with estimates of ψ derived from lensing or other methods.

Since $\hat{\eta}$ is again large, fluctuations in the deprojected estimate $\tilde{j}_X$ will be considerably smoothed as in the case of the thermal SZ effect.

Chapter 4

4 Reconstruction of the mass distribution using gravitational lensing

Gravitational lensing probes the second derivatives of the line-of-sight projected Newtonian potential of a galaxy cluster, observable due to distortions of background galaxies. As mentioned in Section 3.2.1 we can identify different regimes of lensing – strong and weak gravitational lensing – which are applicable for massive galaxy clusters.

We further focus the following discussion on weak lensing only as this regime covers the galaxy cluster as a whole. In comparison, strong lensing only occurs in a small region within the core of the galaxy cluster.

A reliable error estimation is crucial for reconstructions of the mass distribution using the effects of gravitational lensing. Due to the statistical nature of weak lensing, the signal at different positions in the reconstruction will be correlated. This correlation has to be considered when the uncertainty of the reconstruction is to be evaluated.

In the following chapter we want to explain how the well-established strong- and weak-lensing reconstruction code *SaWLens* (which is an acronym for **S**trong **A**nd **W**eak **Lens**ing) from Merten (2010) works in the weak lensing case alone. *SaWLens* belongs to a special class of lensing reconstruction codes which are parameter-free and non-local, but like others suffers from the same problem: The reconstruction method is non-linear due to the non-linearity of the reduced shear (see Section 3.2.1). This in turn means that an error estimation in an analytic fashion is difficult. So far, error estimations have been done by means of a bootstrap method, a highly computationally expensive procedure. Therefore, an analytic way to estimate the errors made in such reconstructions would be favourable but difficult to achieve due to the mentioned non-linearities.

We will explain how an approach to an analytic error estimation can be made by strictly following the weak-lensing reconstruction method from the *SaWLens* code. By testing our analytic method with simulated NFW halos we can directly compare our result to the real scatter in the retrieved convergence maps. Furthermore, we will compare our results to the classical bootstrap method already implemented in *SaWLens*.

4.1 A strong- and weak-lensing reconstruction code

The reconstruction code *SaWLens* from Merten et al. (2009) and Merten (2010) is a non-parametric maximum-likelihood reconstruction method based on the works by Bartelmann et al. (1996); Seitz et al. (1998); Bradač (2004) and Cacciato et al. (2006). Using strong-lensing constraints, like the positions of multiple images or giants arcs, and weak-lensing constrains, i.e. the mean ellipticity of background galaxies, the code is capable to recover the underlying lensing potential ψ by a χ^2-minimisation. In this context non-parametric means that the code is independent of any a-priori as-

sumptions regarding the underlying lensing potential. As the method is grid-based (see below for details) with an adaptive-mesh-refinement technique, the obtained results are a discrete representation of ψ that is most likely to produce the observed lensing features.

4.1.1 General concept

SaWLens divides the observational field into a given number of cells, from now on called pixels. As an input *SaWLens* requires an ellipticity catalogue containing the positions of the sources in an arbitrary coordinate frame and the two corresponding components of the ellipticity. For strong-lensing constraints *SaWLens* needs the positions of multiple images and giant arcs.

Strong- and weak-lensing signals constrain the same underlying lensing potential, but the constraints are independent from each other. An appropriate χ^2-function will therefore consist of a weak- and a strong-lensing term,

$$\chi^2(\psi) = \chi^2_{\mathrm{w}}(\psi) + \chi^2_{\mathrm{s}}(\psi)\,. \tag{4.1}$$

The χ^2-function needs to be minimised with respect to the lensing potential at a given position a,

$$\frac{\partial\chi^2(\psi)}{\partial\psi_a} = \frac{\partial\chi^2_{\mathrm{w}}(\psi)}{\partial\psi_a} + \frac{\partial\chi^2_{\mathrm{s}}(\psi)}{\partial\psi_a} \stackrel{!}{=} 0\,. \tag{4.2}$$

The term ‘position’ refers to a specific grid cell, and the minimisation is achieved by varying the potential values in the grid cells.

This maximum likelihood approach is very flexible as it allows for the inclusion of arbitrarily many terms in the χ^2-function. At the present stage *SaWLens* includes multiple images, information on critical curves, ellipticity and flexion measurements. But in principle one could include an appropriate term for constraints from thermal X-ray emission due to bremsstrahlung. Analogously, one could include a term for the CMB distortions caused by the thermal Sunyaev-Zel’dovich effect or information based on measurements of galaxy kinematics. How statements on the lensing potential can be made for the first two of these three will be discussed in Chapter 6 and Chapter 7. The last constraint, the galaxy kinematics, is discussed in Sarli et al. (2013). There are also numerical tests on the feasibility of adding further constraints provided by Huber (2013).

Concerning the χ^2-minimisation it is obvious, due to the reduced shear in Eq. (3.17) and the strong-lensing features, that it is not a linear system of equations. However, the non-linearities may be approximately linearised in an iterative scheme, following the idea of Schneider & Seitz (1995), also applied in Bradač et al. (2005). In doing so, the non-linear factors in each term are kept constant in each iteration and their values are given by the preceding step, this iteration we call *inner-level iteration*. As Bradač et al. (2005) suggested, an initial guess of no mass present is assumed, only marginally affecting the result of the reconstruction.

Modern weak-lensing observations only allow an angular resolution of roughly $0.5'$, if pixels should be uncorrelated. This number is only influenced by the number of observed background galaxies. Though a higher resolution is favourable, it inevitably correlates different pixels, clearly affecting the reconstruction. A higher resolution will also cause the reconstructed mass to be increased, as at a higher grid resolution, grid cells in the central part of the cluster are expected to contain more mass. But increasing the signal strength clearly contradicts the starting assumption of a vanishing convergence. This problem can be overcome by introducing another iteration level (called *outer-level iteration*) beginning with a very low resolution. With this resolution the inner-level iteration from above is performed until the reconstruction converges. Thereafter, the resolution is slightly increased by interpolation of the obtained lensing potential (for further details, see Bradač et al., 2005). The inner-level iteration is repeated till again the reconstruction converges. In this manner the reconstruction is repeated in the outer-level iteration until the desired resolution is reached.

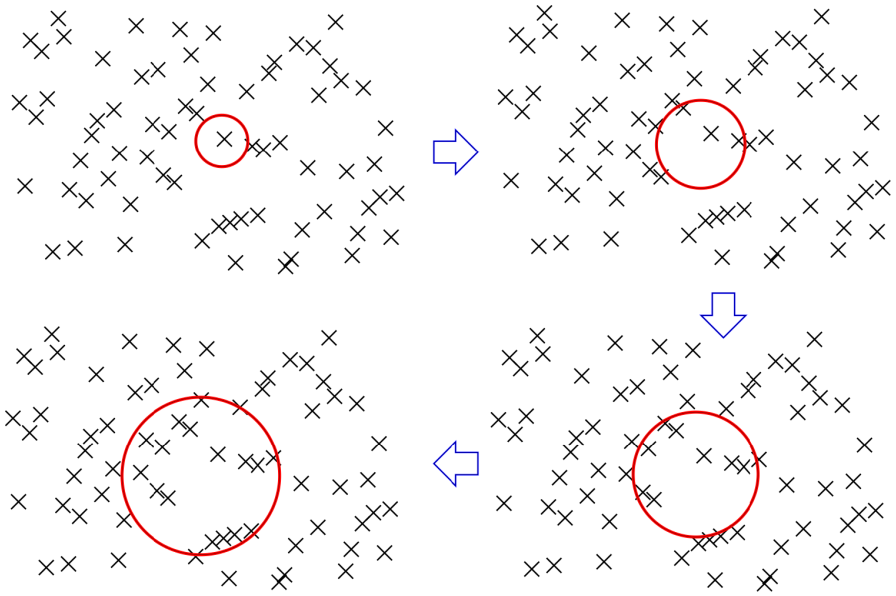

Figure 4.1: Averaging procedure of *SaWLens*. A circle is drawn around a pixel position and its size is iteratively increased to cover a predefined number of galaxies (black crosses).

4.1.2 Weak-lensing constraints

To account for the statistical nature of the weak-lensing signal, each pixel is assigned with two values, one for each mean ellipticity of that area. This averaging process produces correlations between adjacent pixels. The number of galaxies used in each pixel is crucial for the reconstruction, as the signal-to-noise ratio increases with the number of used galaxies. Each pixel should contain the average value obtained from roughly the same number of background galaxies. This is achieved by an adaptive averaging process in which the mean is taken in circles around each pixel centre. The radius of each circle is iteratively increased until a predefined number of galaxies is reached. This results in a specific radius for each pixel, due to local fluctuations in the background galaxy density, the correlation between pixels will also dependend on position. Figure 4.1 shows this adaptive averaging process for a random position in the observational field.

Given the theoretical background from Section 3.2.1, we are able to define the χ^2_w-function needed in Eq. (4.1). Since the pixels are correlated because of the chosen averaging method and the expectation value of the ellipticity is given by the reduced shear (see Eq. 3.17), we write

$$\chi^2_\mathrm{w}(\psi) = \left(\langle\epsilon\rangle - \frac{\gamma(\psi)}{1-\kappa(\psi)}\right)^\mathrm{T}_i C^{-1}_{ij} \left(\langle\epsilon\rangle - \frac{\gamma(\psi)}{1-\kappa(\psi)}\right)_j \tag{4.3}$$

$$= \left(\frac{1}{1-\kappa(\psi)}\left[\langle\epsilon\rangle\,(1-\kappa(\psi)) - \gamma(\psi)\right]\right)^\mathrm{T}_i C^{-1}_{ij} \left(\frac{1}{1-\kappa(\psi)}\left[\langle\epsilon\rangle\,(1-\kappa(\psi)) - \gamma(\psi)\right]\right)_j , \tag{4.4}$$

where C^{-1}_{ij} is the inverse of the covariance matrix (see below) and $\langle\epsilon\rangle$ is the mean ellipticity in each pixel. Also note, that we sum over all indices appearing twice. The cosmological weight $Z(z)$ from Eq. (3.20) is implicitly included in the shear and convergence. The inverse covariance matrix C^{-1}_{ij} depends on the number of averaged galaxies per pixel and thus on the size of the corresponding averaging circle. Given the standard deviation σ of the ellipticity in each pixel obtained from the averaging procedure, the inverse covariance matrix can be written as

$$C^{-1}_{ij} = w_{ij}\sigma_i\sigma_j \tag{4.5}$$

with a weight factor w_{ij} representing a relative weight which depends on the number of shared galaxies

between pixels i and j. Going back to Eq. (4.3) and applying the differential operators from Eq. (3.15), the shear components and convergence can be replaced in terms of the lensing potential.

Convergence and shear are now discretised on a grid and may be written as a column vector, changing only the data handling itself. The used differential operators are approximated by finite differencing, according to a Taylor expansion (see Merten et al. (2009); Merten (2010) for further details), and represented by symmetric sparse matrices. This conversion allows us to write the second derivatives of ψ, i.e. the convergence and shear, as simple multiplications with the respective differential operator,

$$\kappa_i = \mathcal{K}_{ij}\psi_j\,, \tag{4.6}$$

$$\gamma_i^1 = \mathcal{G}_{ij}^1\psi_j\,, \tag{4.7}$$

$$\gamma_i^2 = \mathcal{G}_{ij}^2\psi_j\,. \tag{4.8}$$

We return to Eq. (4.4) and write the factors containing the non-linearities $1/(1-\kappa)$ as a diagonal matrix M and combine it with the inverse covariance matrix C^{-1}, which defines the matrix H such that

$$H_{kl} \equiv M_{ki}\, C_{ij}^{-1}\, M_{jl}\,. \tag{4.9}$$

This changes Eq. (4.4) to

$$\chi^2_{\mathrm{w}}(\psi) = \left[\langle\epsilon\rangle\,(1-\kappa(\psi)) - \gamma(\psi)\right]_i^{\top}\; H_{il}\; \left[\langle\epsilon\rangle\,(1-\kappa(\psi)) - \gamma(\psi)\right]_l\,, \tag{4.10}$$

We define the diagonal matrix

$$N \equiv \mathrm{diag}(1-\kappa_i) = \mathrm{diag}(1-\mathcal{K}_{ik}\psi_k)\,, \tag{4.11}$$

which changes Eq. (4.10), once the products are expanded, to

$$\chi^2_{\mathrm{w}}(\psi) = \langle\epsilon\rangle_i N_{ij} H_{jk} N_{kl} \langle\epsilon\rangle_l - 2\langle\epsilon\rangle_i N_{ij} H_{jk}\gamma_k + \gamma_j H_{jk}\gamma_k\,. \tag{4.12}$$

From now on we will excessively use the fact that all calligraphic matrices as well as N and H are symmetric. Minimising this χ^2-function yields

$$\frac{\partial\chi^2}{\partial\psi_a} = 2\langle\epsilon\rangle_i \left(N_{ij}H_{jk}\right)\frac{\partial N_{kl}}{\partial\psi_a}\langle\epsilon\rangle_l - 2\langle\epsilon\rangle_i\frac{\partial N_{ij}}{\partial\psi_a}H_{jk}\gamma_k - 2\langle\epsilon\rangle_i N_{ij}H_{jk}\frac{\partial\gamma_k}{\partial\psi_a} + 2\gamma_j H_{jk}\frac{\partial\gamma_k}{\partial\psi_a}\,. \tag{4.13}$$

With the definitions from Eqs. (4.7), (4.8) and (4.11), we find for the derivatives

$$\frac{\partial\gamma_k}{\partial\psi_a} = \frac{\partial}{\partial\psi_a}\mathcal{G}_{kb}\psi_b = \mathcal{G}_{ka}\,, \tag{4.14}$$

$$\frac{\partial N_{kl}}{\partial\psi_a} = \frac{\partial}{\partial\psi_a}\mathrm{diag}(1-\kappa_k) = \mathrm{diag}(-\mathcal{K}_{ka})\,. \tag{4.15}$$

Returning to Eq. (4.13), we insert the results from above to obtain

$$\frac{\partial\chi^2}{\partial\psi_a} = -\sum_{k=1}^{N}\left(2\langle\epsilon\rangle_i N_{ij}H_{jk}\langle\epsilon\rangle_k\mathcal{K}_{ka}\right) + \sum_{j=1}^{N}\left(2\langle\epsilon\rangle_i H_{jk}\gamma_k\mathcal{K}_{ja}\right) - 2\langle\epsilon\rangle_i N_{ij}H_{jk}\mathcal{G}_{ka} + 2\gamma_j H_{jk}\mathcal{G}_{ka}\,. \tag{4.16}$$

In the first sum in Eq. (4.16) we can insert the definition (4.11) of the matrix N, thus

$$\begin{aligned}
-\sum_{k=1}^{N} 2\langle\epsilon\rangle_i N_{ij}H_{jk}\langle\epsilon\rangle_k\mathcal{K}_{ka} &= -\sum_{i,k=1}^{N} 2\langle\epsilon\rangle_i(1-\kappa_i)H_{ik}\langle\epsilon\rangle_k\mathcal{K}_{ka} \\
&= -\sum_{i,k=1}^{N} 2\langle\epsilon\rangle_i H_{ik}\langle\epsilon\rangle_k\mathcal{K}_{ka} + \sum_{i,k=1}^{N} 2\langle\epsilon\rangle_i\mathcal{K}_{ib}\psi_b H_{ik}\langle\epsilon\rangle_k\mathcal{K}_{ka} \\
&\equiv -y_a + A_{ab}\psi_b\,.
\end{aligned} \tag{4.17}$$

The second sum of Eq. (4.16) turns into

$$\sum_{j=1}^{N} 2\langle\epsilon\rangle_i H_{jk}\gamma_k\mathcal{K}_{ja} \equiv B_{ab}\psi_b\,. \tag{4.18}$$

The third and fourth term in Eq. (4.16) can be re-defined correspondingly,

$$\begin{aligned} -2\langle\epsilon\rangle_i N_{ij} H_{jk}\mathcal{G}_{ka} &= -\sum_{i=1}^{N} 2\langle\epsilon\rangle_i(1-\mathcal{K}_{ib}\psi_b)H_{ik}\mathcal{G}_{ka} \\ &\equiv -z_a + D_{ab}\psi_b\,, \qquad (4.19) \\ 2\gamma_j H_{jk}\mathcal{G}_{ka} &= 2\mathcal{G}_{jb}\psi_b H_{jk}\mathcal{G}_{ka} \\ &\equiv E_{ab}\psi_b\,. \qquad (4.20) \end{aligned}$$

Once we combine the results from Eqs. (4.17) – (4.20) we find

$$\frac{\partial\chi^2}{\partial\psi_a} = -y_a + A_{ab}\psi_b + B_{ab}\psi_b - z_a + D_{ab}\psi_b + E_{ab}\psi_b\,, \tag{4.21}$$

which should be equal to zero. This complete formalism directly results in a solvable system of linear equations,

$$\mathcal{B}_{ab}\psi_b = \mathcal{V}_a \tag{4.22}$$

with the coefficient matrix $\mathcal{B}_{ab}$ and the vector $\mathcal{V}_a$ for one shear component,

$$\mathcal{B}_{ab} = A_{ab} + B_{ab} + D_{ab} + E_{ab}\,, \tag{4.23}$$

$$\mathcal{V}_a = y_a + z_a\,. \tag{4.24}$$

The system for the second shear component can be written in the exact same form. We note here once more that the matrix H contains the non-linearities discussed in Section 4.1.1 and is only updated in the outer-level iteration.

4.1.3 Regularisation

Up to now the reconstruction is sensitive to intrinsic noise patterns not reflecting real features of the underlying lensing potential. This can be avoided by introducing a further term $R(\psi)$ in Eq. (4.1), adding another summand to the final system of linear equations (4.22). This is chosen such that its amplitude can be regulated by the parameter η,

$$R \equiv \eta\left[\bar{\kappa}_i - \kappa_i(\psi)\right]^{\mathrm{T}}\left[\bar{\kappa}_i - \kappa_i(\psi)\right]\,. \tag{4.25}$$

The convergence $\bar{\kappa}_i$ is chosen as the convergence of the preceding outer-level iteration step – or of the prior, if no outer-level iteration preceded.

This definition implies that the convergence must not deviate too strongly from the result – or the prior – preceding the current iteration step, starting the iteration with the assumption of no convergence (as mentioned in Section 4.1.1). The additions to the set of linear equations (4.22) due to the regularisation term are given by,

$$\mathcal{B}^{\mathrm{reg}}_{ab} = \eta\mathcal{K}_{al}\mathcal{K}_{lb}\,, \tag{4.26}$$

$$\mathcal{V}^{\mathrm{reg}}_{a} = \eta\bar{\kappa}_i\mathcal{K}_{ia}\,. \tag{4.27}$$

4.2 Approaching an analytic error estimation

4.2.1 Covariance of the ellipticity

Starting with the correlation between the measured ellipticities, we have to return to the averaging scheme explained in Section 4.1.1. Once the averaging circles contain the given number of background galaxies, also the overlap between two pixels is constrained. From Fig. 4.2 we can determine the overlap area A, depending of the pixel separation d and pixel radius R, taken as the mean value of all radii,

$$A(d) = 2R^2 \left[\arcsin\left(\sqrt{1 - \frac{d^2}{4R^2}} \right) - \frac{d}{2R} \sqrt{1 - \frac{d^2}{4R^2}} \right] \quad \text{for} \quad d \leq 2R\,. \tag{4.28}$$

The ellipticity $\bar{\epsilon}_i$ in a pixel i is given by the sum of all ellipticity measurements in the corresponding circle, thus

$$\bar{\epsilon}_i = \frac{1}{N_i} \sum_{a=1}^{N_i} \epsilon_a \tag{4.29}$$

with N_i being the number of galaxies in the averaging circle. This relation certainly holds for any two pixels (i, j) as well, further allowing us to give an estimator for the covariance $\langle \bar{\epsilon}_i \bar{\epsilon}_j \rangle$ of two pixels (i, j),

$$\langle \bar{\epsilon}_i \bar{\epsilon}_j \rangle = \frac{1}{N_i N_j} \sum_{a=1}^{N_{ij}} \langle \epsilon_a^2 \rangle \tag{4.30}$$

with the summation over all galaxies contained in the overlap of the two circles, N_{ij}. We note here that the above consideration is only possible if nearby galaxies are assumed to have uncorrelated ellipticities. Further, the expectation value $\langle \epsilon_a^2 \rangle$ is given by half of the intrinsic variance σ_ϵ^2 of the ellipticities as we have two independent ellipticity components. Inserting the expectation value of the ellipticity yields the expectation value of the covariance C_{ij}^ϵ,

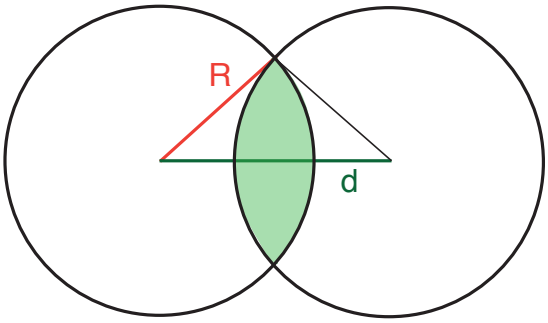

Figure 4.2: Geometry of the averaging scheme for two pixels with distance d and corresponding averaging circles with radius R. The green area shows the overlap.

$$\begin{aligned} C_{ij}^\epsilon \equiv \langle \bar{\epsilon}_i \bar{\epsilon}_j \rangle &= \frac{1}{N_i N_j} \frac{\sigma_\epsilon^2}{2} N_{ij} \\ &= \frac{\sigma_\epsilon^2}{2n\pi R^2} A(d_{ij}) \end{aligned} \tag{4.31}$$

with the given galaxy density n at the position (i, j) and the distance d_{ij} between two pixels. In the case of an unknown galaxy density at the specific position we can replace n with the mean galaxy density of the complete field of view.

4.2.2 Covariance of the convergence

The χ^2-function for weak lensing including the regularisation term from Section 4.1.3 can be rewritten with the use of the general differential operators from Section 4.1.1. For practical reasons we will from now on drop the matrix indices which gives the operators from the definitions in Eqs. (4.6) – (4.8) the following form,

$$\mathcal{K} \equiv \frac{1}{2} \left(\frac{\partial^2}{\partial x^2} + \frac{\partial^2}{\partial y^2} \right), \quad \mathcal{G}_1 \equiv \frac{1}{2} \left(\frac{\partial^2}{\partial x^2} - \frac{\partial^2}{\partial y^2} \right), \quad \mathcal{G}_2 \equiv \frac{\partial^2}{\partial x \partial y}\,. \tag{4.32}$$

In this notation the χ^2-function from Eq. (4.1), only including the weak lensing and regularisation term, is given as

$$\begin{aligned}\chi^2 = &(\epsilon_1 - N\mathcal{G}_1\psi)^\top\ C_1^{-1}\ (\epsilon - N\mathcal{G}_1\psi) + (\epsilon_2 - N\mathcal{G}_2\psi)^\top\ C_2^{-1}\ (\epsilon_2 - N\mathcal{G}_2\psi)\\ &- \eta\ (\bar{\kappa} - \mathcal{K}\psi)^\top\ (\bar{\kappa} - \mathcal{K}\psi)\ ,\end{aligned} \tag{4.33}$$

where ϵ, ψ and κ are functions of the two coordinates (x, y), or equivalently of the pixel 'numbers' (i, j). The matrix N is defined as

$$N \equiv \mathrm{diag}\left[(1 - \kappa_i)^{-1}\right]\ . \tag{4.34}$$

We will now assume that the entries of N are spatially constant, during an inner-level iteration, which allows us to find the minimum of the χ^2-function at

$$\frac{\partial\chi^2}{\partial\psi} \stackrel{!}{=} 0 = 2\ (\epsilon_1 - N\mathcal{G}_1\psi)^\top\ C_1^{-1}\ (-N\mathcal{G}_1) + 2\,(\epsilon_2 - N\mathcal{G}_2\psi)\,C_2^{-1}\,(-N\mathcal{G}_2) - 2\eta\,(\bar{\kappa} - \mathcal{K}\psi)\,\mathcal{K}\,. \tag{4.35}$$

Note here, that in this way we do not account for the linearised terms from Eq. (4.4). We further transform Eq. (4.35) to

$$\left(\mathcal{K}^2\eta + N\mathcal{G}_1C_1^{-1}N\mathcal{G}_1 + N\mathcal{G}_2C_2^{-1}N\mathcal{G}_2\right)\psi = C_1^{-1}N\mathcal{G}_1\epsilon_1 + C_2^{-1}N\mathcal{G}_2\epsilon_2 + \eta\mathcal{K}\bar{\kappa}\,. \tag{4.36}$$

We assume the covariance matrix of the first shear component to be equal to the covariance of the second component as they should follow the same statistics if we neglect intrinsic correlations of nearby galaxies. Of course, the inverse covariance matrices $C_1^{-1} = C_2^{-1}$ then have to be equal as well. We further assume the covariance matrix to be diagonal with entries σ_i^2, thus we can define a matrix $S \equiv \mathrm{diag}(\sigma_i^{-2})$. Additionally, we apply the convergence operator $\mathcal{K}$ on both sides to make the transition from the lensing potential ψ to the convergence κ,

$$\left(\mathcal{K}^2\eta + N\mathcal{G}_1SN\mathcal{G}_1 + N\mathcal{G}_2SN\mathcal{G}_2\right)\kappa = \mathcal{K}SN\mathcal{G}_1\epsilon_1 + \mathcal{K}SN\mathcal{G}_2\epsilon_2 + \eta\mathcal{K}^2\bar{\kappa}\,. \tag{4.37}$$

We can abbreviate this equation by introducing the following quantities,

$$P^{-1} \equiv \left(\mathcal{K}^2\eta + N\mathcal{G}_1SN\mathcal{G}_1 + N\mathcal{G}_2SN\mathcal{G}_2\right)\ , \tag{4.38}$$

$$A_k \equiv \mathcal{K}SN\mathcal{G}_k\epsilon_k\,, \tag{4.39}$$

$$B \equiv \eta\mathcal{K}^2 \tag{4.40}$$

with $k \in (1, 2)$, which results in the short-hand notation of Eq. (4.37),

$$\kappa = P\,(A_1\epsilon_1 + A_2\epsilon_2 + B\bar{\kappa})\ . \tag{4.41}$$

From this equation we can calculate the covariance of the convergence using the tensor product $\otimes$,

$$\mathrm{Cov}(\kappa) \equiv \langle\kappa \otimes \kappa'\rangle\,. \tag{4.42}$$

This leads us to an expression for the covariance,

$$\begin{aligned}\langle\kappa \otimes \kappa'\rangle &= P^2A_1^2\langle\epsilon_1 \otimes \epsilon_1'\rangle + P^2A_2^2\langle\epsilon_2 \otimes \epsilon_2'\rangle + P^2B^2\langle\bar{\kappa} \otimes \bar{\kappa}'\rangle\\ &\quad + P^2A_1B\langle\epsilon_1 \otimes \bar{\kappa}'\rangle + P^2A_1B\langle\bar{\kappa} \otimes \epsilon_1'\rangle + P^2A_2B\langle\epsilon_2 \otimes \bar{\kappa}'\rangle + P^2A_2B\langle\bar{\kappa} \otimes \epsilon_2'\rangle\\ &= P^2A_1^2\langle\epsilon_1 \otimes \epsilon_1'\rangle + P^2A_2^2\langle\epsilon_2 \otimes \epsilon_2'\rangle + P^2B^2\langle\bar{\kappa} \otimes \bar{\kappa}'\rangle\\ &\quad + 2P^2A_1B\langle\epsilon_1 \otimes \bar{\kappa}'\rangle + 2P^2A_2B\langle\epsilon_2 \otimes \bar{\kappa}'\rangle\,.\end{aligned} \tag{4.43}$$

The difference between the convergence and the preceding estimate should be zero and thus $\bar{\kappa} = \kappa$ once the algorithm has converged. But for now we will take $\bar{\kappa}$ as a smaller estimate of the final convergence as it leads us to a better understanding in the following, so that

$$\bar{\kappa} = a\kappa \quad \text{with} \quad a \leq 1\,. \tag{4.44}$$

The convergence $\bar{\kappa}$ is expected to be smaller than the final convergence κ since we start our iteration with $\kappa \equiv 0$. However, we cannot guarantee that at some iteration step we will find $\bar{\kappa} > \kappa$, but due to experience and the regularisation term this is unlikely to happen.

We now need to evaluate the terms containing the ellipticity and convergence from Eq. (4.43). This is done by inserting Eq. (4.41) again,

$$\begin{aligned}\langle \epsilon_1 \otimes \bar{\kappa}' \rangle =& \langle \epsilon_1 \otimes (aP\,(A_1\epsilon_1 + A_2\epsilon_2 + B\bar{\kappa}))' \rangle \\ =& \left(\mathcal{I} - aPB\right)^{-1} aPA_1 \langle \epsilon_1 \otimes \epsilon_1' \rangle\,, \qquad (4.45)\\ \langle \epsilon_2 \otimes \bar{\kappa}' \rangle =& \langle \epsilon_2 \otimes (aP\,(A_1\epsilon_1 + A_2\epsilon_2 + B\bar{\kappa}))' \rangle \\ =& \left(\mathcal{I} - aPB\right)^{-1} aPA_2 \langle \epsilon_2 \otimes \epsilon_2' \rangle\,. \qquad (4.46)\end{aligned}$$

These expressions are now replaced in Eq. (4.43) for the covariance, which changes it to

$$\left(\mathcal{I} - aPB\right) \langle \kappa \otimes \kappa' \rangle = \left(P^2A_1^2 + P^2A_2^2\right) \left(\mathcal{I} - aPB\right)^{-1} \langle \epsilon \otimes \epsilon' \rangle\,, \qquad (4.47)$$

while we use

$$\langle \epsilon \otimes \epsilon' \rangle = \langle \epsilon_1 \otimes \epsilon_1' \rangle = \langle \epsilon_2 \otimes \epsilon_2' \rangle\,. \qquad (4.48)$$

This equation is now transferred to Fourier space, where the differential operators are represented as simple multiplication factors with the respective k-vectors. Here we are able to calculate the covariance $\langle \hat{\kappa} \otimes \hat{\kappa}'^{\star} \rangle$ between to convergences $\hat{\kappa}$ and the complex-conjugated convergence in Fourier space $\hat{\kappa}'^{\star}$. The Fourier transformations of the differential operators are given as

$$\begin{aligned}\hat{\mathcal{K}} &= -\frac{1}{2}\left(k_1^2 + k_2^2\right)\,, \qquad (4.49)\\ \hat{\mathcal{G}}_1 &= -\frac{1}{2}\left(k_1^2 - k_2^2\right)\,, \qquad (4.50)\\ \hat{\mathcal{G}}_2 &= -k_1k_2\,, \qquad (4.51)\\ \hat{\mathcal{G}}_1^2 + \hat{\mathcal{G}}_2^2 &= \frac{1}{4}\left(k_1^2 + k_2^2\right)^2 = \hat{\mathcal{K}}^2\,, \qquad (4.52)\end{aligned}$$

with an important identity in the last equation. Once we Fourier transform Eq. (4.47), the differential operators $\mathcal{G}_1$, $\mathcal{G}_2$, and $\mathcal{K}$ are replaced by simple multiplications. We can further infer with the definitions of Eqs. (4.38) – (4.40),

$$\begin{aligned}\hat{P}^{-1} &= \left(\hat{\mathcal{K}}^2\eta + N^2S\hat{\mathcal{K}}^2\right)\\ &= N\left(\eta N\hat{\mathcal{K}}^2N + S\hat{\mathcal{K}}^2\right)N\\ &= N\left\{\left[\eta(N^{-1})^2 + S\right]\hat{\mathcal{K}}^2\right\}N\,, \qquad (4.53)\\ \hat{A}_k &= \hat{\mathcal{K}}\hat{\mathcal{G}}_kNS\,, \qquad (4.54)\\ \hat{B} &= \eta\hat{\mathcal{K}}^2\,. \qquad (4.55)\end{aligned}$$

Given these expressions we can evaluate the terms in Eq. (4.47) in Fourier space,

$$\begin{aligned}\hat{P} &= N^{-1}\left(\eta N^{-2} + S\right)^{-1} N^{-1}\,\hat{\mathcal{K}}^{-2}\,, \qquad (4.56)\\ \hat{P}^2\hat{A}_k^2 &= N^{-1}\left(\eta N^{-2} + S\right)^{-1} N^{-1}\,\hat{\mathcal{K}}^{-2}\hat{\mathcal{G}}_k^2\,S^2\,, \qquad (4.57)\\ \mathcal{I} - a\hat{P}\hat{B} &= \mathcal{I} - a\eta N^{-1}\left(\eta N^{-2} + S\right)^{-1} N^{-1}\,. \qquad (4.58)\end{aligned}$$

In the Fourier-transformed Eq. (4.47) we find a term $\hat{P}^2\hat{A}_1^2 + \hat{P}^2\hat{A}_2^2$, which contains the operators $\mathcal{K}$ and $\mathcal{G}_k$, where we can substitute the sum of both squared shear operators with the operator for the

converge according to the identity (4.52). In this way the calligraphic operators in Eq. (4.47) cancel each other, and we find

$$\left(\hat{P}^2\hat{A}_1^2 + \hat{P}^2\hat{A}_2^2\right)\left(\mathcal{I} - a\hat{P}\hat{B}\right)^{-2} = N^{-1}\left(\eta N^{-2} + S\right)^{-2} N^{-1} S^2 \left[\mathcal{I} - a\eta N^{-1}\left(\eta N^{-2} + S\right)^{-1} N^{-1}\right]^{-2} . \quad (4.59)$$

As the matrices N and S are diagonal, we can easily obtain their inverse, which transforms the above equation to

$$\left(\hat{P}^2\hat{A}_1^2 + \hat{P}^2\hat{A}_2^2\right)\left(\mathcal{I} - a\hat{P}\hat{B}\right)^{-2} = \mathcal{I}\,\frac{(1-\kappa)^2}{\left[\eta\sigma^2\,(1-\kappa)^2\,(1-a)+1\right]^2} . \quad (4.60)$$

Once we apply the inverse Fourier transform and insert this result into Eq. (4.47), we find for the covariance of the convergence κ,

$$\langle \kappa \otimes \kappa' \rangle = \frac{(1-\kappa)^2}{\left[\eta\sigma^2\,(1-\kappa)^2\,(1-a)+1\right]^2}\langle \epsilon \otimes \epsilon' \rangle . \quad (4.61)$$

This equation holds an intuitive explanation for the effect on the covariance of the convergence κ if regularisation is present and the algorithm did not fully converge yet: The difference between the current result and the fully converged solution, is still large due to strong regularisation, reducing the covariance. But we have to make statements about the unknown $\bar{\kappa}$ if we want to calculate values for the covariance. Ideally, the difference between the convergence and the preceding estimate is zero and thus $\bar{\kappa} = \kappa$, equally we can state that the factor a should approach one. This assumption will also eliminate the regularisation parameter η, obvious from Eq. (4.25), as the above equation reduces to

$$\langle \kappa \otimes \kappa' \rangle = (1-\kappa)^2\,\langle \epsilon \otimes \epsilon' \rangle . \quad (4.62)$$

Unfortunately, we do not know exactly if *SaWLens* has fully converged and is independent of any prior for a specific reconstruction, posing problems in evaluating the factor a. By simply assuming convergence of the algorithm, the obtained error estimate will certainly be biased to higher values.

4.3 Application to mock data

In the following sections we want to test our analytic expression from Eq. (4.61) for the covariance of the convergence on mock cluster catalogues. From the density profile of a spherically symmetric NFW halo we derive the convergence map and the two components of the ellipticity in a field covering the whole cluster to the virial radius.

4.3.1 Creation of ellipticity catalogues

We simulate a galaxy cluster with a mass of $M = 5 \times 10^{14}\,\mathrm{M}_\odot\,h^{-1}$ resulting in a virial radius (taken as r_{200}) of $r_{\mathrm{vir}} = 1.25\,\mathrm{Mpc}\,h^{-1}$. Further we choose a concentration parameter of $c = 5$. The redshift is taken to be $z = 0.2$. We reconstruct the cluster within its virial radius which defines the field of view to be $17.5 \times 17.5\,\mathrm{arcmin}^2$.

The background galaxies are placed randomly over the entire field and to each of them we assign the ellipticities, which are generated by the convergence and shear as predicted from the density profile. Furthermore, to account for intrinsic ellipticities, we use a Gaussian distribution with a standard deviation of 0.3 (Heavens, 2003) for each component of the ellipticity. According to Eq. (3.18) we transform the reduced shear and the intrinsic ellipticity to obtain the measured ellipticity. With this model we can create different noise realisations of the same cluster and can directly measure the variance in the reconstructed convergence. This procedure we will call our *numerical experiment*.

The density of background galaxies is chosen to be $n = 30\,\mathrm{arcmin}^{-2}$, matching observations. As we want to compare the reconstructed halos with the expected convergence, we smooth the introduced convergence on the same angular scale as our reconstruction.

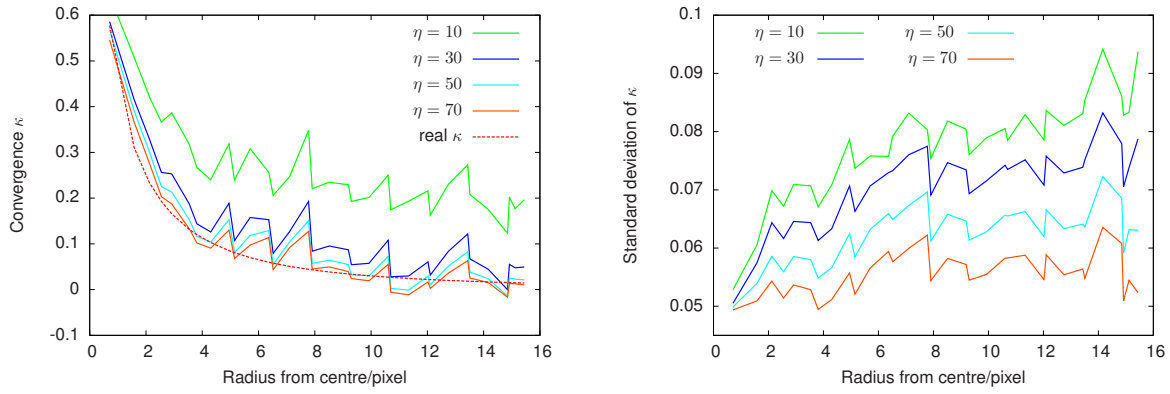

(a) (b)

Figure 4.3: (a) Convergence profile for different regularisation parameters ($\eta = 10, 30, 50, 70$) compared to the true convergence smoothed on the same angular scale (dotted red curve). (b) Standard deviation of the convergence for different regularisation parameters.

4.3.2 Dependence on the regularisation

According to Eq. (4.25) the regularisation term should approach zero as the reconstruction algorithm converges. However, *SaWLens* has an internal stopping criterion by comparing two consecutive iteration steps and allowing only for a pre-set deviation. For high values of η the reconstruction will need many iterations to converge as the prior of no lensing potential will dominate. Considering the limited computational power there is clearly a tradeoff between the time needed for a reconstruction and accuracy. On the other hand, η must be high enough to prevent the algorithm from fitting noise patterns.

For regularisation to be efficient in the first iteration steps, the χ^2-contributions of the reconstruction and the regularisation should be similar; as the iteration proceeds, the regularisation will (and should) shrink. In our case the amplitude of the signal is governed by the strength of the covariance between two pixels, thus approximately by the main diagonal elements of the inverse covariance matrix C^{-1}. In our chosen example the optimal regularisation would be of the order $\eta \approx 30$ as directly inferred from the inverse covariance matrix.

We test *SaWLens* by reconstructing our mock catalogues with different regularisation parameters and compare the results to the convergence we created the initial catalogues with. The smallest tested value is $\eta = 10$, as for lower regularisation the noise becomes too strong. We bin our ellipticity catalogues on an 18×18 grid and increase the resolution up to 32×32 with 20 galaxies per pixel. A higher resolution would significantly increase the computational time needed for our test. Furthermore, a resolution much higher than 45×45 would result in such a strong correlation between different pixels that the system of linear equations is not solvable any more. Due to the spherical symmetry we will focus on azimuthally averaged radial profiles, allowing us to compare the reconstruction to the true convergence profile.

Figure 4.3(a) shows the result of the reconstruction using different regularisation parameters compared to the true convergence in dependence of the cluster radius in pixels. A low regularisation parameter (i.e. $\eta = 10$, green curve in Fig. 4.3(a)) results in fitting the noise pattern and overestimating the convergence in the outskirts of the cluster. A higher regularisation parameter enforces the starting assumption of a vanishing convergence and the overestimation in the outskirts is eliminated. On the other hand, stronger regularisation than effectively needed (i.e. $\eta = 70$, orange curve in figure 4.3(a)) will result in a flatter profile in the cluster centre.

We produce 50 ellipticity catalogues for the same cluster and reconstruct each of them with *SaWLens* using the given regularisation amplitudes η from above. With this set of noise realisations of the same

underlying cluster we can calculate the standard deviation in each pixel. Following the spherical symmetry, the resulting standard deviation is again plotted as a radial profile in Fig. 4.3(b). We see that a stronger regularisation leads to a flatter profile in the standard deviation following our expectations if the reconstruction did not fully converge yet. The pre-factor a from definition (4.44) should be less than unity and according to Eq. (4.61) the standard deviation has to be flatter. Apparently, even though the best possible interpolation between different resolutions is used (i.e. one pixel per iteration), the algorithm is still not independent of the regularisation parameter for high values of η. This would imply that we have to focus on Eq. (4.61) rather than on Eq. (4.62) if we were to estimate the variance.

4.3.3 Testing the analytic model

In the light of the results from the above section we are now capable to compare our analytical model from Eq. (4.61) to these findings. We will focus again on the standard deviation, thus we can replace ϵ' with ϵ and the convergence κ' with κ. This corresponds to the case in Section 4.2.1 if the averaging circles fully overlap. From this we can derive the standard deviation of the convergence again as an azimuthally averaged profile and compare it to our numerical experiment.

According to Eq. (4.61) we need the convergence κ itself in each pixel. The variance of the ellipticity is obtained from Eq. (4.31) where we replace the intrinsic variance σ_ϵ^2 with the value obtained with *SaWLens* in each pixel. In the same manner we can insert the number of galaxies obtained in each averaging circle.

Furthermore, we can compare our analytic results to the traditional method of bootstrapping. So far, reconstructions of the mass distribution using this iterative scheme obtain their errors by re-sampling the input catalogues (Bradač et al., 2005), with the two ellipticity components. This is done by drawing galaxies from the parent catalogue but returning the galaxies. In this way a set of new catalogues is produced. A reconstruction is run on each of them and the resulting scatter provides the standard deviation. However, this technique is computationally expensive as every sample has to be reconstructed with the same resolution and the same number of iterations. We compare our analytic result with the bootstrapping method for one specific regularisation $\eta = 30$ and use 50 bootstrapping catalogues.

In Fig. 4.4 the numerical result from Section 4.3.2, the analytical result from Eq. (4.61), using $a = 1$ (see Section 4.3.2 for explanation), and the mentioned bootstrap method from *SaWLens* are shown. Obviously, both methods underestimate the standard deviation of the convergence for the centre pixels, though this effect is stronger for the analytic model. However, as we are considering radial profiles each data point is given as the mean of several pixels with the same distance to the centre, allowing us to give a corresponding error. Figure 4.4 also illustrates the corresponding one-sigma-error with the light-blue area for the numerical experiment, explained in Section 4.3.1. We see that both error estimations are within one standard deviation, indicating that our analytic error estimation is capable to give quantitive statements.

4.4 Application to a realistic N-body/hydrodynamica cluster simulation

4.4.1 N-body cluster simulations

To further test our analytic model for the variance of the convergence we test Eq. (4.61) on a realistic cluster simulation. Our data set is taken from Meneghetti et al. (2010b) (denoted g1), based on original work from Saro et al. (2006). This cluster is based on an N-body/hydrodynamical simulation with a ΛCDM model ($\Omega_\mathrm{m} = 0.3$, $\Omega_\mathrm{b} = 0.04$, $h = 0.7$, and $\sigma_8 = 0.9$), see also Tab. 4.1 for more details of the cluster, including the best-fitting values for an NFW profile.

The cluster simulation itself was obtained as follows: A simulation with only dark matter was carried out and in regions where clusters formed the area was re-simulated with a higher mass resolution

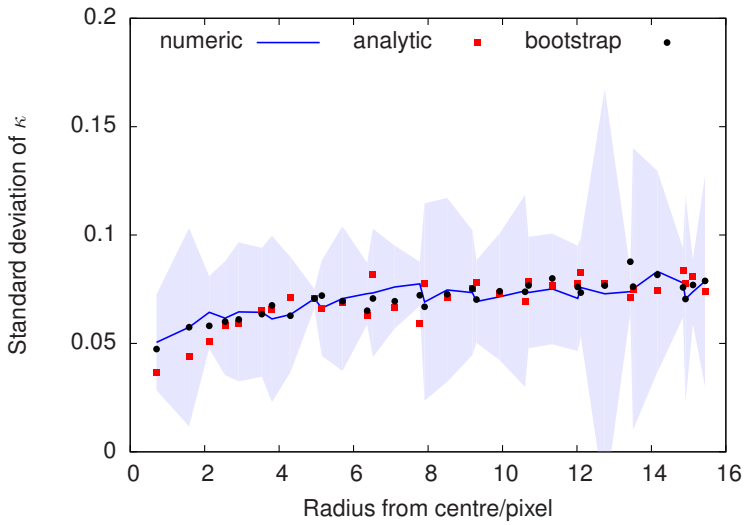

Figure 4.4: Profile of the standard deviation of the reconstructed convergence for $\eta = 30$ (blue curve), the same quantity according to Eq. (4.61) (red) and obtained from the bootstrapping technique (black) implemented in *SaWLens*. The standard deviation obtained from the numerical experiment due to the azimuthal average in each bin is indicated by the light-blue area.

and an additional baryonic component. The parent simulation was carried out by Yoshida et al. (2001) with the ΛCDM model from above. The new initial conditions for the re-simulation were obtained with the *Zoomed Initial Condition technique* from Tormen et al. (1997). Many publications (Dolag et al., 2005; Puchwein et al., 2005; Meneghetti et al., 2007, 2008; Rasia et al., 2006, 2008) have analysed some of these clusters – including g1 – in great detail.

We use the specific re-simulations of Saro et al. (2006), which were done with the N-body/Smoothed Particle Hydrodynamics-code *Gadget 2* (Springel, 2005), including radiative cooling, galactic winds, supernova feedback and chemical enrichment. From this simulation the lensing data were obtained with the *SkyLens*-tool (Meneghetti et al., 2008). *SkyLens* is a ray-tracing code which follows light rays through different planes in the sky and evaluates the position and intensity changes in each of them, corresponding to the scenario in Fig. 3.4. *SkyLens* itself uses a realistic catalogue of background galaxies from the *Hubble Ultra Deep Field* (Beckwith et al., 2006) and the *Great Observatories Origins Deep Survey* (Giavalisco et al., 2004) archives. These sources are decomposed using shapelets (Melchior, 2010) and the components are lensed by the cluster. The last step to proceed towards a realistic observation is the imitation of the *SUBARU Suprime-Cam*. Details on the parameters for this chosen simulation are found in Merten (2010) and Meneghetti et al. (2010b).

This simulated observation is then analysed using again *SkyLens* with the *KSB-method* (Kaiser et al., 1995; Luppino & Kaiser, 1997; Hoekstra et al., 1998). This method decomposes the surface brightness of each observed galaxy into multipoles. After a correction for the point spread function of the telescope one finally obtains the ellipticity components for each galaxy. This catalogue is then the input for our reconstruction with *SaWLens*.

Table 4.1: Main properties of cluster g1, taken from Meneghetti et al. (2010b). Given are the redshift z of the cluster, the used projection plane, axis ratios and best-fitting NFW-profile parameters.

z	projection plane	r_{200} $[h^{-1}\mathrm{Mpc}]$	M_{200} $[h^{-1}\mathrm{M}_\odot]$	b/a	c/a	c_{200}	r_s $[h^{-1}\mathrm{Mpc}]$
0.297	xy	1.54	1.14×10^{15}	0.64	0.57	4.46	0.31

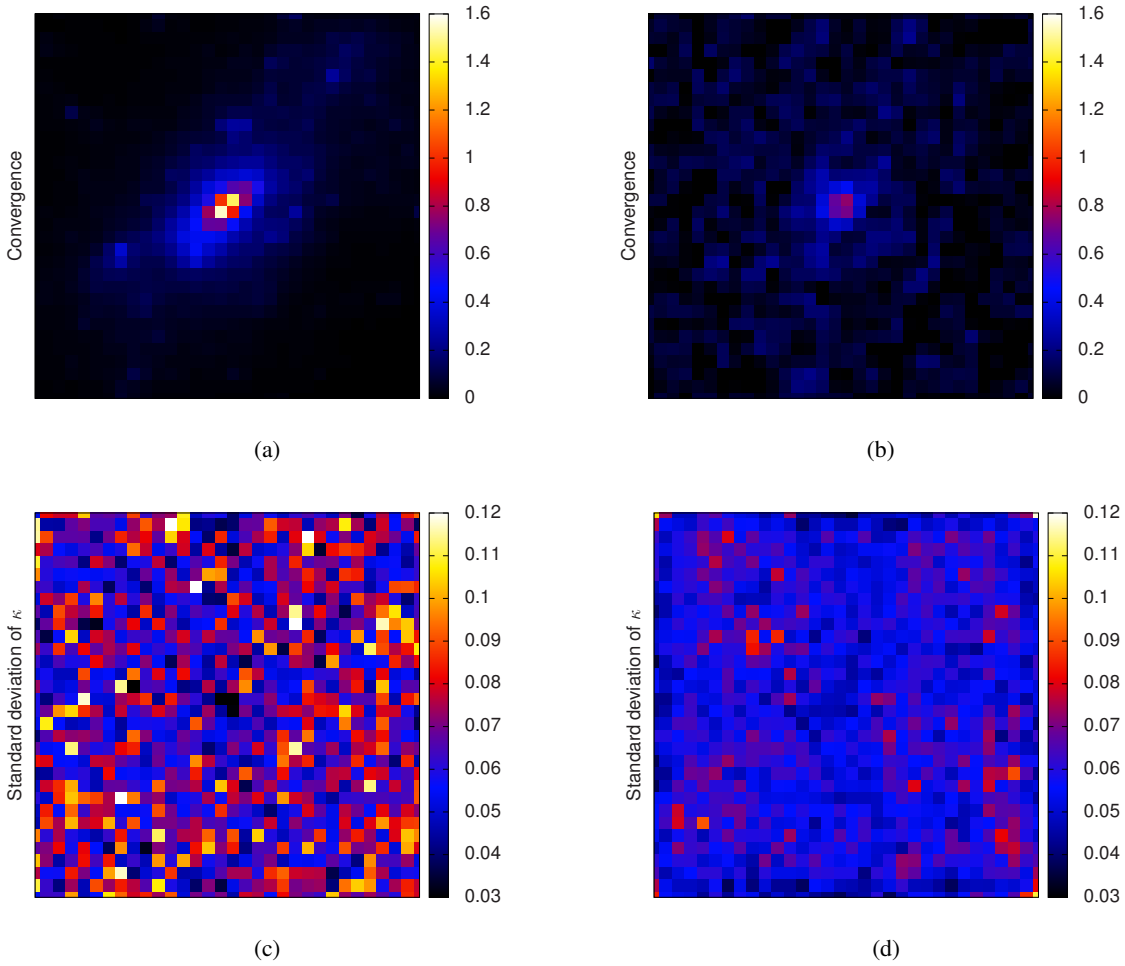

Figure 4.5: (a) Convergence of the g1 cluster on a resolution of 32×32 pixels, the centre reaches values up to $\kappa = 1.5$. (b) Reconstruction using *SaWLens* with weak-lensing information only. The convergence reaches values of $\kappa = 0.8$ and we are capable to retrieve the elongation along the main diagonal. We see slightly elevated values of the convergence in the lower left part, for which we find a corresponding structure in (a). (c) Standard deviation of (b) using Eq. (4.62). (d) Same as (c) but obtained with the bootstrapping method implemented in *SaWLens*.

4.4.2 Cluster reconstruction and error estimation

Our data set is the projection along the z-direction of the simulation and has a field of view of $21' \times 21'$. It contains roughly 13700 background galaxies, corresponding to a galaxy density of $n \approx 30$ galaxies per arcmin^2. Using the same starting resolution of 18×18 pixels and step-width of one pixel per outer-level iteration like in Section 4.3.3, we again stop at a resolution of 32×32 pixels, using 10 galaxies per pixel. Again we estimate the best value for the regularisation parameter η by evaluating the inverse covariance matrix C^{-1}: We find $\eta = 50$.

This regularisation is higher than before in Section 4.3.3 due to the intrinsic difference of the catalogues. With $\eta = 50$, Eq. (4.61) with a reasonably chosen value of a should be used. We choose a value $a = 0.98$, corresponding to a marginal correction to $\bar{\kappa}$. The result of the weak-lensing reconstruction in comparison to the real convergence map with the same resolution is shown in Fig. 4.5(a) and (b). We see that a weak-lensing reconstruction underestimates the convergence significantly. This issue of underestimating the convergence while using weak-lensing measurements has already been discussed in Merten (2010), see also Fig. 4.6(a). Nevertheless, *SaWLens* is capable of reproducing the elongation along the main diagonal from the lower left to the upper right corner, which corresponds to

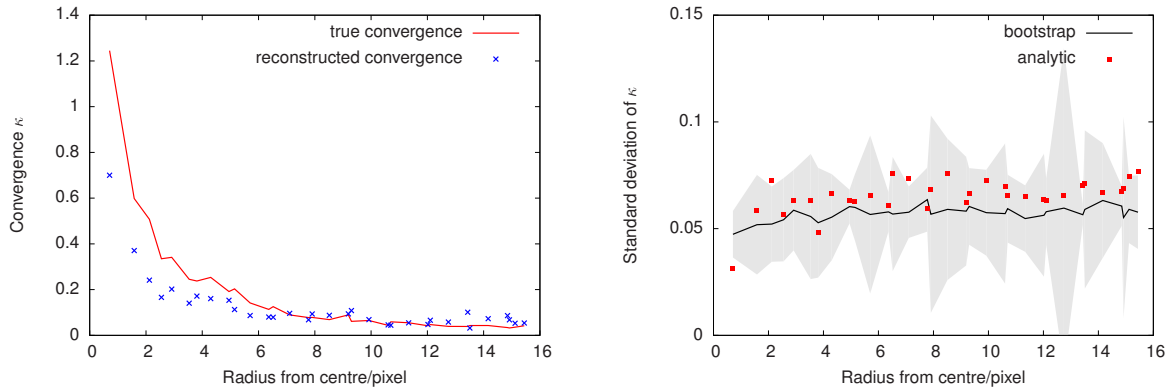

(a) (b)

Figure 4.6: (a) Azimuthal average of the convergence obtained from the simulation directly and from the weak-lensing reconstruction. (b) Azimuthal average of the standard deviation (red) squares corresponding to Fig. 4.5(c) and the profile obtained from bootstrapping (black), corresponding to Fig. 4.5(d). The grey-shaded area indicates the one-sigma region due to the circular average obtained from the bootstrap.

the inclination of nearly 45° as given in Meneghetti et al. (2010b).

In the same way as explained in Section 4.3.3 we can calculate the standard deviation of the convergence in each pixel. This is also shown in Fig. 4.5, where we compare the analytic standard deviation (Fig. 4.5(c)) and the standard deviation obtained from bootstrapping (Fig. 4.5(d)). In both plots we see the lowered standard deviation in the cluster centre. This is expected as close to the cluster centre the signal strength should increase and less scatter is expected. However, the dip obtained with the bootstrapping method is not as deep as the one from the analytical model. We further can state from Fig. 4.5(c) in comparison to (d) that the scatter of the obtained standard deviation is much larger in the analytic model.

Furthermore, we can evaluate the standard deviation of the convergence as a azimuthally averaged profile. Figure. 4.6(b) shows this profile obtained analytically and by bootstrapping together with the one-sigma region (grey-shaded area) due to the azimuthal averaging process. As in Fig. 4.5(c) and (d), the central dip in the standard deviation is visible in the averaged profile of Fig. 4.6(b). Our analytic estimate for the standard deviation is mostly inside the one-sigma region obtained from the bootstrap but is slightly biased to higher values. This is most likely due to the chosen value of $a = 0.98$. Using Eq. (4.61) together with a smaller value for a would lower the standard deviation, better matching the obtained values from the bootstrap.

4.5 Summary and conclusion

In this chapter we have explained the reconstruction code *SawLens*, especially focussing on reconstructions using weak-lensing information. Starting from the χ^2-function for weak lensing including a regularisation term we showed how an analytic expression for the variance of the convergence κ can be obtained, see Eq. (4.61 and Eq. (4.62)). This expression needs the reconstructed convergence as well as the variance of the ellipticities used in the reconstruction. Both quantities are already computed by *SaWLens*, thus no further computational effort is needed. From Eq. (4.61) the dependence on the regularisation parameter η could be explained compared to the fully converged reconstruction using the relative size a of $\bar{\kappa}$ compared to κ. This factor is so far unconstrained and needs further assessment in future projects to reliably match it to the used value of η.

We used mock catalogues with an underlying NFW density profile to compare this analytic expression to the real scatter obtained from reconstructing different realisations of the same galaxy cluster.

Furthermore, we tested the bootstrap implementation from *SaWLens* with one specific regularisation parameter $\eta = 30$ and compared it to the analytic model. The analytically obtained, azimuthally averaged profile of the standard deviation of the convergence showed the same lowered value in the cluster centre, in compliance with the numerical experiment and the bootstrap method. The analytic model lay within the one-sigma region of the standard deviation indicated by our numerical experiment.

To obtain results in a more realistic scenario we applied our model to the simulation of a massive galaxy cluster based on an N-body/hydrodynamical simulation with a ΛCDM model. A comparison between the analytic model and a bootstrap for this cluster revealed good agreement for the obtained uncertainties of the convergence κ. Also the feature of a diminishing standard deviation towards the cluster centre was reproduced within one standard deviation. We further noted that the scatter in the standard deviation is larger and the standard deviation was slightly biased to higher values, though mostly still within the one-sigma region of the results obtained with bootstrapping.

With these findings a reliable error estimation for weak-lensing reconstructions using *SaWLens* can be achieved by this analytic model. Even more, as the analytic model relies only on quantities which have to be calculated by *SaWLens* anyway, an error estimation can be done without any further computational effort. This is also interesting in the sense that fields with better angular resolution - than the one used above – can be achieved by current weak-lensing observations.

The runtime of common bootstrap methods is a major limiting factor in the reconstruction of the mass distribution of galaxy clusters. Large science projects like the CLASH project (see Chapter 3) analyse observed clusters in the weak-lensing regime with resolutions of up to 150×150 pixels. Due to these large fields the error estimation consumes roughly 80% of the time needed for a reconstruction. This severe issue can be completely overcome by this novel approach we presented here. Our analytic approach can readily be implemented in existing weak-lensing reconstruction pipelines, once the parameter a is chosen. However, if the reconstruction has fully converged and is independent of any prior – which its most favourable – the result should be independent of the regularisation and hence $a = 1$.

Following the procedure explained, i.e. carefully following the reconstruction prescription, an analytic error estimation for strong-lensing features seems also feasible. Certainly, due to the non-linear behaviour of the strong-lensing constraints in the reconstruction further assumptions have to be made for an analytic error estimation.

Chapter 5
5 Richardson-Lucy deprojection

In the following chapters we will focus on reconstructions of the potential of galaxy clusters using the thermal Sunyaev-Zel'dovich effect or the emission of thermal bremsstrahlung. Both observables have been explained in Section 3.2.2 and Section 3.2.3. With the assumptions made there these observables probe the gravitational potential of galaxy clusters. However, only their corresponding three-dimensional quantities may give this insight. Inevitably, we need a deprojection technique to retrieve the three-dimensional quantity from its line-of-sight integrated observable.

This chapter explains the chosen deprojection algorithm based on the method presented by Lucy (1974, 1994b,a), first assuming spherical symmetry and then relaxing this assumption to a spheroidal cluster geometry. Furthermore, we will briefly discuss the merits of this *Richardson-Lucy* deprojection method compared to other techniques.

We also present a direct comparison to the well established *onion peeling method*. This method was recently applied to the massive galaxy cluster *Abell 1689* by Eckert et al. (2012).

The contents of this chapter have been published in Tchernin, Majer, Meyer et al. (2013), Majer, Meyer, Konrad et al. (2013) and Konrad, Majer, Meyer et al. (2013).

5.1 Merits and limits of deprojections

As described above we adopt the Richardson-Lucy algorithm (Lucy, 1974, 1994b) for deprojection. Because there are different algorithms for the deprojection of two- into three-dimensional distributions, we want to give a brief discussion of the main features of other deprojection methods.

We begin with the well known *onion peeling method* (Fabian et al., 1981; Kriss et al., 1983), which is very intuitive, though it has the drawback of being a non-local method. The data is binned around the centre of the cluster in annuli with a chosen width. In each of these annuli the average value is taken, in doing so the deprojected quantity is approximated by this constant multiplied with the volume of the three-dimensional shell corresponding to the chosen position. This procedure is progressing inwards once the outer shells have been calculated and subtracted. For each three-dimensional shell at a given radius one has to know the result of all shells with larger radius. This method therefore produces a strong correlation between different shells. Another disadvantage is the strong dependence on the outermost shell, or equivalently, the problem of defining the boundaries of the cluster.

Another widely used method is the deprojection based on an *Abel transform* (for a brief discussion see Mamon & Boué, 2010). This technique involves numerical integration as well as calculating derivatives in each data-bin. Due to the latter the inversion is highly sensitive to fluctuations, inevitable in real observations. This disadvantage may be overcome by smoothing the data or fitting it to an assumed model, but the second approach would give up the non-parametric character of this deprojection.

Considering these points, avoiding non-locality is a good choice for our purpose, one choice for such a method is the Richardson-Lucy deprojection. It is non-parametric and local, in the sense that all, within the limits of observational smoothing, lines-of-sight are independent. An individual line-of-sight certainly collects information from a large number of radial bins. But, as each line-of-sight integral does not depend on the integral of another line-of-sight we may have holes of missing data in our input, which is a most welcome feature. It is of great importance as we assume hydrostatic equilibrium and a polytropic stratification of the ICM to proceed from the deprojected quantity to the gravitational potential. The mentioned assumptions are often not applicable in the centre of clusters due to a number of processes (e.g. cooling effects) wherefore the Richardson-Lucy algorithm allows us to leave out the centre of clusters. The RL-scheme includes an entropic regularisation term, which in turn smoothes the result and accelerates the convergence of the code itself. It is important to say that the strength of the regularisation is relaxed as the deprojection proceeds.

A recent comparison of our method with the onion peeling algorithm from Eckert et al. (2012) can be found in Tchernin et al. (2013) and will also be discussed in Section 5.6.

5.2 Principles of the Richardson-Lucy deprojection

Generally, the Richardson-Lucy (RL) deprojection connects two functions, say $g(s)$ and $f(r)$, related by projection and deprojection,

$$g(s) = \int \mathrm{d}r\, K(s|r)\, f(r)\,, \tag{5.1}$$

$$f(r) = \int \mathrm{d}s\, K'(r|s)\, g(s)\,, \tag{5.2}$$

and mediated by the projection kernel $K(s|r)$ and the deprojection kernel $K'(r|s)$ respectively. The functions $g(s)$ and $f(r)$ as well as their kernels need to be designed such that they fulfil the non-negativity and normalisation criteria,

$$\int \mathrm{d}s\, g(s) = 1 \quad \text{and} \quad \int \mathrm{d}r\, f(r) = 1\,, \tag{5.3}$$

$$\int \mathrm{d}s\, K(s|r) = 1 \quad \text{and} \quad \int \mathrm{d}r\, K'(r|s) = 1\,. \tag{5.4}$$

Neither the deprojection $f(r)$ nor the deprojection kernel $K'(r|s)$ are known. However, given an estimate $\tilde{f}_i(r)$ at the iteration step i for the function $f(r)$ and using *Bayes' Theorem*, an estimate $\tilde{g}_i(s)$ of the projection $g(s)$ is

$$\tilde{g}_i(s) = \int \mathrm{d}r\, K(s|r)\tilde{f}_i(r)\,, \tag{5.5}$$

implying the estimate for the deprojection kernel

$$\tilde{K}'(r|s) = \frac{\tilde{f}_i(r)}{\tilde{g}_i(s)}\, K(s|r)\,. \tag{5.6}$$

The RL-scheme is now given by the estimate $\tilde{f}_i(r)$ for the function $f(r)$ at the iteration level i and an improved estimate $\tilde{f}_{i+1}(r)$ is found by

$$\tilde{f}_{i+1}(r) = \tilde{f}_i(r) \int \mathrm{d}s\, \frac{g(s)}{\tilde{g}_i(s)}\, K(s|r)\,. \tag{5.7}$$

Beginning with a reasonable guess for $\tilde{f}_0(r)$, the iteration Eq. (5.7) usually converges quickly.

A regularisation term needs to be included in presence of noise to prevent overfitting. Lucy (1994b) showed that, provided $g(s)$ is normalised, the deprojection algorithm described by the above iteration can be cast into the form

$$\begin{aligned}\Delta_H \tilde{f}_i(r) &= \tilde{f}_{i+1}(r) - \tilde{f}_i(r) \\ &= \tilde{f}_i(r)\left(\frac{\delta H[\tilde{f}_i]}{\delta \tilde{f}_i(r)} - \int \mathrm{d}r\, \tilde{f}_i(r)\frac{\delta H[\tilde{f}_i]}{\delta \tilde{f}_i(r)}\right),\end{aligned} \tag{5.8}$$

containing the functional derivative of

$$H[\tilde{f}] = \int \mathrm{d}s\, g(s) \ln \tilde{g}(s)\,, \tag{5.9}$$

with respect to $\tilde{f}_i(r)$, as $\tilde{g}(s)$ is a function of $\tilde{f}$ through Eq. (5.1). If we interpret $g(s)$ at a given position as the probability density assigned to each $\tilde{g}(s)$, the likelihood L writes as

$$\ln L = H[\tilde{f}] + \mathrm{const}\,, \tag{5.10}$$

hence $H[\tilde{f}]$ is equivalent to a likelihood function. It is maximised in order to obtain the best possible solution. Lucy (1994b) suggested to augment $H[\tilde{f}]$ by the entropic term

$$S[\tilde{f}] = -\int \mathrm{d}r\, \tilde{f}(r) \ln \frac{\tilde{f}(r)}{\chi(r)}\,, \tag{5.11}$$

which contains a prior $\chi(r)$ to suppress small scale fluctuations. The functional H is then replaced by

$$H[\tilde{f}] \rightarrow Q[\tilde{f}] = H[\tilde{f}] + \alpha S[\tilde{f}] \tag{5.12}$$

with a parameter α, called *strength of regularisation*, controlling the influence of the entropic term. Since

$$\frac{\delta S[\tilde{f}_i]}{\delta \tilde{f}_i(r)} = -\ln \frac{\tilde{f}_i(r)}{\chi(r)} - 1\,, \tag{5.13}$$

the entropic term changes the iteration prescription to

$$\Delta \tilde{f}_i = \tilde{f}_{i+1}(r) - \tilde{f}_i(r) = \Delta_H \tilde{f}_i + \Delta_S \tilde{f}_i \quad \text{with} \quad \Delta_S \tilde{f}_i = -\alpha \tilde{f}_i \left(\ln \frac{\tilde{f}_i}{\chi} + S[\tilde{f}]\right), \tag{5.14}$$

again provided that $\tilde{f}_i$ is normalised.

The prior $\chi(r)$ against which the deprojection is to be regularised should reflect a-priori knowledge of the expected solution. If such knowledge is absent an appropriate choice would be a constant prior. But as shown by Narayan & Nityananda (1986); Lahav & Gull (1989) and Lucy (1994b), the choice of a constant prior leads to a statistical bias in the estimates of the deprojected functions such that they appear flatter than they should. This issue can be addressed by selecting as a default solution a smoothed version of the previously obtained result. This approximation, known as *floating default solution* (Horne, 1985; Lucy, 1994b), is built by adopting the following definition,

$$\chi(r) = \int_0^\infty \mathrm{d}r'\, P(r|r') f(r')\,, \tag{5.15}$$

where $P(r|r')$ is a normalised, sharply peaking and symmetric function of $r - r'$. In our investigations, we choose a properly normalised Gaussian form with *smoothing scale* L corresponding to the standard deviation of the Gaussian

$$P(r|r') = \frac{1}{\sqrt{2\pi L^2}} \exp\left[-\frac{(r-r')^2}{2L^2}\right]. \tag{5.16}$$

5.3 Richardson-Lucy deprojection and spherical symmetry

Assuming spherical symmetry, we rewrite Eq. (5.1) as

$$g(s) = \int_0^\infty \mathrm{d}r\, K(s|r) f(r) \tag{5.17}$$

with the specific projection kernel

$$K(s|r) = \frac{2}{\pi} \frac{r}{\sqrt{r^2 - s^2}} \Theta(r^2 - s^2)\,, \tag{5.18}$$

where the factor $2/\pi$ was introduced to ensure that the kernel K is normalised. The theta-function only allows radii r which are larger than a given value of s.

Exploiting the assumed spherical symmetry of the cluster, we can re-bin our two-dimensional data in concentric annuli, averaging the observable in each of them. An overview of these annuli and the line-of-sight is given in Fig. 5.1(a) and (b). The function $g(s)$ is now replaced by a specific observation, e.g. SZ or X-ray measurements. By deprojecting this observable we find an estimate $\tilde{f}(r)$ for the corresponding three-dimensional quantity $f(r)$.

Proceeding in this manner we can use the connection between the effective pressure P, the three-dimensional equivalent to the specific intensity change from the thermal SZ effect (see Section 3.2.2), and the gravitational potential. Correspondingly, we can use the link between the X-ray emissivity (see Section 3.2.3), the deprojected quantity from the X-ray surface brightness, and the gravitational potential. According to Eq. (3.11) the lensing potential ψ is the properly scaled line-of-sight projection of the gravitational potential. Therefore we can infer an estimate $\tilde{\psi}$ for the two-dimensional potential, which is proportional to the lensing potential. It can thus be directly combined with estimates of ψ derived from lensing or other methods.

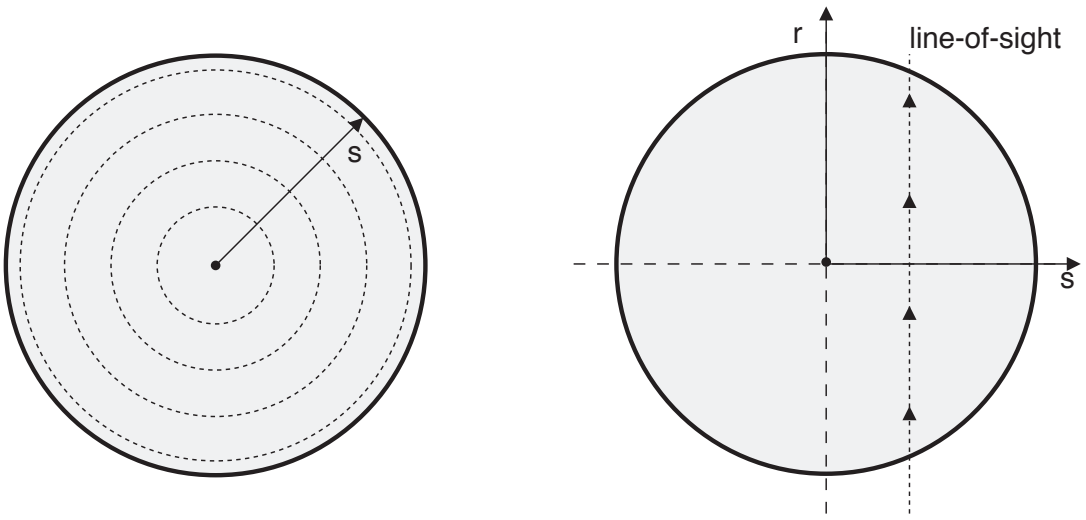

(a) (b)

Figure 5.1: (a) Procedure of radial averaging in the observational plane and the corresponding radius s. (b) Orthogonal view to (a), explaining the orientation of the line-of-sight. Due to the spherical symmetry and convenience we can draw the three-dimensional radius r in this orientation.

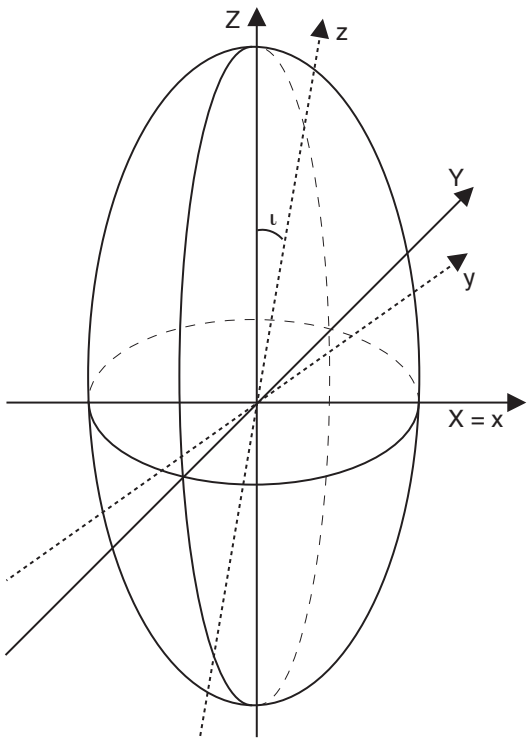

Figure 5.2: Relation between the observer's frame of reference (x, y, z) and the cluster coordinate system (X, Y, Z). The systems are assumed to be inclined to each other with an inclination angle ι. Also compare this geometrical setup with the spherical one in Fig. 5.1(a) and (b) from Section 5.3.

5.4 Richardson-Lucy deprojection and spheroidal symmetry

We now relax our symmetry assumption towards spheroidal cluster geometries. The observer's frame of reference is denoted by small letters (x, y, z); the cluster is then observed in the (x, y)-plane, and the z-direction corresponds to the line-of-sight. The coordinate frame of the cluster is defined by capital letters (X, Y, Z), this frame is inclined by the angle ι against the observer's frame of reference, as depicted in Fig. 5.2. The observed galaxy cluster has its own frame of reference, namely the (R, Z)-plane, while Z is pointing along the symmetry axis of the spheroidally shaped cluster and R is the radius. This definition allows us to define the following coordinate-transformations and a relation for R,

$$X = x\,, \tag{5.19}$$

$$Y = y\cos\iota - z\sin\iota\,, \tag{5.20}$$

$$Z = y\sin\iota + z\cos\iota\,, \tag{5.21}$$

$$R = \sqrt{X^2 + Y^2}\,. \tag{5.22}$$

The line-of-sight projection is then given as an integral of $f(R, Z)$,

$$\begin{aligned} g(x, y) &= \int \mathrm{d}z\, f(R(x, y, z), Z(x, y, z)) \\ &= \int \mathrm{d}R \int \mathrm{d}Z\, f(R, Z)\, K(x, z|R, Z)\,. \end{aligned} \tag{5.23}$$

So far we have not specified the deprojection kernel $K(R, Z|x, y)$, which was given by Eq. (5.18) in the spherically symmetric case from Section 5.3. If we want to construct the kernel, we have to

define it in our specific geometry. Following the line of thought from Binney et al. (1990), also presented in Reblinsky (2000a,b); Puchwein & Bartelmann (2006); Puchwein (2007), a deprojection kernel $K(x, y|R, Z)$ for elliptical objects may be derived. Binney et al. (1990) formulated this kernel for the deprojection of elliptical galaxies, beginning with the deprojected quantity $f(R, Z)$,

$$f(R,Z) = \int_0^\infty \mathrm{d}R'^2 \int_{-\infty}^\infty \mathrm{d}Z'\, f(R',Z')\, \delta(R^2 - R'^2)\, \delta(Z - Z')\,. \tag{5.24}$$

This is now projected along the line-of-sight using Eq. (5.23) to yield the projected quantity $g(x, y)$ in the observer's frame of reference,

$$g(x,y) = \int_{-\infty}^\infty \mathrm{d}z \int_0^\infty \mathrm{d}R'^2\, \delta\left[R^2(x,y,z) - R'^2\right] \int_{-\infty}^\infty \mathrm{d}Z'\, f(R',Z')\, \delta\left[Z(x,y,z) - Z'\right]\,. \tag{5.25}$$

The δ-distribution can be rewritten as $\delta\left[f(x)\right] = \sum_s \frac{\delta(x-x_s)}{|f'(x_s)|}$. The function f' is the derivative of f with respect to x. $f(x)$ has to be a real and differentiable function with $f(x_s) = 0$. By replacing the δ-distribution and applying the coordinate transformation from Eqs. (5.19), (5.20), and (5.21), we find

$$f(z_s) = y\sin\iota + z_s\cos\iota - Z' \stackrel{!}{=} 0 \Rightarrow z_s = \left.\frac{Z' - y\sin\iota}{\cos\iota}\right|_{\cos\iota\neq 0}\,. \tag{5.26}$$

The inclination angle can be restricted to $0 \leq \iota < \pi/2$ which leads to non-zero and positive values of $\cos\iota$. Further substituting R with the relation given in Eq. (5.22) yields

$$\begin{aligned} g(x,y) = \pi \int_0^\infty \mathrm{d}R'^2 \int_{-\infty}^\infty \mathrm{d}Z' \int_{-\infty}^\infty \mathrm{d}z\, \frac{f(R',Z')}{\cos\iota} \\ \times\, \delta\left[x^2 + (y\cos\iota - z\sin\iota)^2 - R'^2\right]\, \delta\left(z - \frac{Z' - y\sin\iota}{\cos\iota}\right)\,. \end{aligned} \tag{5.27}$$

After an integration over z, we identify the projection kernel as

$$K(x,y|R,Z) = \frac{\delta\left[\left(\frac{y}{\cos\iota} - Z\tan\iota\right)^2 - (R^2 - x^2)\right]}{\pi\cos\iota}\,. \tag{5.28}$$

This kernel obeys the normalisation constraint

$$\int_{-\infty}^\infty \mathrm{d}x \int_{-\infty}^\infty \mathrm{d}y\, K(x,y|R,Z) = 1\,. \tag{5.29}$$

Given the explicit form of the deprojection kernel allows us to proceed in the RL-scheme. The integral of Eq. (5.25) is given by an integral along the line-of-sight according to Eq. (5.23) which yields an estimate for the projected quantity. At the iteration step n, we proceed in the RL-formalism by re-writing Eq. (5.7) with the estimated deprojection $\tilde{f}_n$,

$$\frac{\tilde{f}_{n+1}(R,Z)}{\tilde{f}_n(R,Z)} = \int \mathrm{d}x \int \mathrm{d}y\, \frac{g(x,y)}{\tilde{g}_n(x,y)}\, K(x,y|R,Z)\,. \tag{5.30}$$

The δ-distribution in the kernel $K(x, y|R, Z)$ above can be eliminated by the same computational rule for the δ-distribution using roots, already used above,

$$\begin{aligned} f(y) = \left(\frac{y}{\cos\iota} - Z\tan\iota\right)^2 - (R^2 - x^2) \stackrel{!}{=} 0 \\ \Rightarrow y_\pm = \cos\iota\left(Z\tan\iota \pm \sqrt{R^2 - x^2}\right)\,. \end{aligned} \tag{5.31}$$

This describes a full ellipse in the observer's sky for a fixed pair of coordinates (R, Z). The derivative f' is then given as

$$f'(y) = \frac{2}{\cos\iota}\left(\frac{y}{\cos\iota} - Z\tan\iota\right)$$
$$\Rightarrow f'(y_\pm) = \pm\frac{2}{\cos\iota}\sqrt{R^2 - x^2}\,. \tag{5.32}$$

This allows us to integrate Eq. (5.30) over the y-coordinate so that

$$\frac{\tilde{f}_{n+1}(R,Z)}{\tilde{f}_n(R,Z)} = \frac{1}{2\pi}\int \mathrm{d}x\,\frac{1}{\sqrt{R^2-x^2}}\left[\frac{g(x,y_+)}{g_n(x,y_+)} + \frac{g(x,y_-)}{g_n(x,y_-)}\right]. \tag{5.33}$$

As the integration over the x-coordinate is limited to $-R \le x \le +R$, we can introduce a variable t:

$$x(t) = R\cos t \Rightarrow x(-\pi) = -R \text{ and } x(0) = R\,,$$
$$\sqrt{R^2-x^2} = R\sqrt{1-\cos^2 t} = -R\sin t \quad \text{for} \quad t \in [-\pi, 0]\,, \tag{5.34}$$

which leads to the final result where we sum over both signs,

$$\frac{\tilde{f}_{n+1}(R,Z)}{\tilde{f}_n(R,Z)} = \frac{1}{2\pi}\sum_{\pm}\int_{-\pi}^{0}\mathrm{d}t\,\frac{g(R\cos t, Z\sin\iota \pm R\sin t\cos\iota)}{\tilde{g}_n(R\cos t, Z\sin\iota \pm R\sin t\cos\iota)}\,. \tag{5.35}$$

In this way the RL-algorithm in spheroidal geometry is fully described by Eq. (5.23) and Eq. (5.35), corresponding to Eq. (5.5) and Eq. (5.7) from the general scheme.

Evaluating Eq. (5.35) involves a problem which concerns Z and R: Imagine our data set to be given by an observation with a specific field of view (FOV) with the coordinates x and y. For large values of Z and R the ellipse, which we integrate over, may partly reach outside this FOV. We therefore need to set some sort of conditions for the boundaries. This issue has been addressed by Reblinsky (2000b) where different methods were tested. A robust solution, regarding the obtained results, is to keep values outside the bounding box constant at the last value along the path of integration inside the box. We will also use this scheme throughout this work.

5.5 Constraining the two degrees of freedom α and $\mathbf{L}$

The strength of regularisation α as well as the smoothing scale L, which we have introduced in Section 5.2, are still unconstrained. α carries a prejudice on how smooth the result should be. Small values of α allow the algorithm to fit the noise and the data rather than the data alone. Contrarily, too strong regularisations result in under-fitting. On the other hand, the floating default kernel with the scale L smoothes the deprojection effectively on the given scale L.

Further improving the idea of the floating default kernel, we make the smoothing scale L dependent on the position s, motivated as follows: The signal-to-noise ratio (S/N) of all cluster observables diminishes towards the outskirts of the cluster. This may be compensated by increasing the effective width of each annulus with the cluster's radius for the spherically symmetric case. The effective width may be changed by either using a non-linear binning and keeping L constant or by keeping the width of each annulus fixed and varying L. The latter is more practical since it allows us to choose an L value according to the given data set and independent of the binning. One simple choice, which is increasing with the radius, is a linearly increasing L with a maximum value $L_{\max}$ at the lagest position $s_{\max}$ of the profile. In this way we reduce the influence of L at the centre of the cluster, whereas we keep the smoothing properties for larger radii. In this manner we tend to have a flatter S/N profile in the smoothed data. But varying the smoothing scale might also cause errors to be correlated in spatially varying ways. For simplicity we do not consider this throughout this work. If we render the

smoothing scale dependent on the position, we still have to set the maximum scale $L_{\max}$ of the floating default kernel (see below).

As pointed out by Lucy (1994b), there is no generally applicable criterion to find the best value for α, though this α does exist. But by testing different expressions and in combination with the floating default kernel, we are able to estimate the best-fitting α. We find it by iterating each deprojection over a given set of possible α values. Certainly, there is an upper limit for α, given by Eq. (5.14), as $\Delta\tilde{f}_i + \tilde{f}_i$ must remain strictly positive due to the normalisation condition. To find the best-fitting α and $L_{\max}$, we calculate the integrated difference, thus we take information from each radial position into account, of the projected deprojection and observational data for each α with a pre-defined $L_{\max} = L_{\max,i}$,

$$W(L_{\max,i}, \alpha) = \left| \int \mathrm{d}s \left[g(s) - \int \mathrm{d}r \, K(s|r) \tilde{f}_i(r) \right] \right|_{L_{\max,i}} . \tag{5.36}$$

This quantity should be as small as possible, implying that the projected deprojection follows the data as well as possible. All the profiles considered in this analysis decrease with s, thus the inner radii contribute most to W.

This procedure is then repeated for a reasonable range of values for $L_{\max,i}$. For each deprojection we compare the projected deprojection with the original data. Again, this quantity is minimised to find the best-fitting $L_{\max,i}$, which is then used for the deprojection.

However, we still have to define the range of $L_{\max}$ values. This range has to be chosen independently for each data set, though the following points give some guide line for $L_{\max}$:

- It should be larger than the average width of two adjacent bins, otherwise L would have a negligible effect.
- For our analysis the data could be smoothed on scales of the same size as the resolution from weak-lensing observations for a later combination of the data sets.
- The noise of the data itself, especially at the outskirts of the cluster, has a strong impact on the scale of the kernel. Once the signal-to-noise profile is known, L could be assessed correspondingly.

5.6 Richardson-Lucy method compared to onion peeling

For testing our algorithm and comparing it to well-established methods like the onion peeling method, we choose the prominent cluster *Abell 1689*. For this massive cluster numerous observations exist (e.g. *Chandra*, *ROSAT*, *Subaru* or *HST*). Motivated by the low background and the data provided by Eckert et al. (2011), reduced with the *ESAS* software (Snowden et al., 1994), we use an archival 13.4 ks surface brightness profile from *ROSAT/PSPC*, see also Fig. 5.3(a). For a detailed description of the data reduction we refer the reader to Eckert et al. (2011). This profile reaches out to large radii in the energy range of 0.4 - 2 keV (see also Vikhlinin et al., 1999).

First of all, we reconstruct the three-dimensional emissivity from the two-dimensional surface brightness using the algorithm for spherical symmetry as described in Section 5.2. We use the errors provided by Eckert et al. (2011) to re-sample the surface brightness with a Gaussian distribution and reconstruct each of the 100 samples. The scale of the floating default kernel L is chosen to be linearly increasing with $L_{\max} = 1.05$ Mpc, whereas the strength of regularisation is taken as $\alpha = 0.2$. Both values are determined once for the original data set by the bootstrap method explained in Section 5.5, and are then kept constant for each sample. In this way we obtain the mean of those 100 samples and the standard deviation, shown in Fig. 5.3(b). The RL deprojection method is normalised, if we want to compare it to other methods we are free to multiply our deprojection with a constant. This multiplicative normalisation constant between both methods is determined by matching our reconstruction and the result from the onion peeling at a radius of 1 Mpc. We find that the performance of

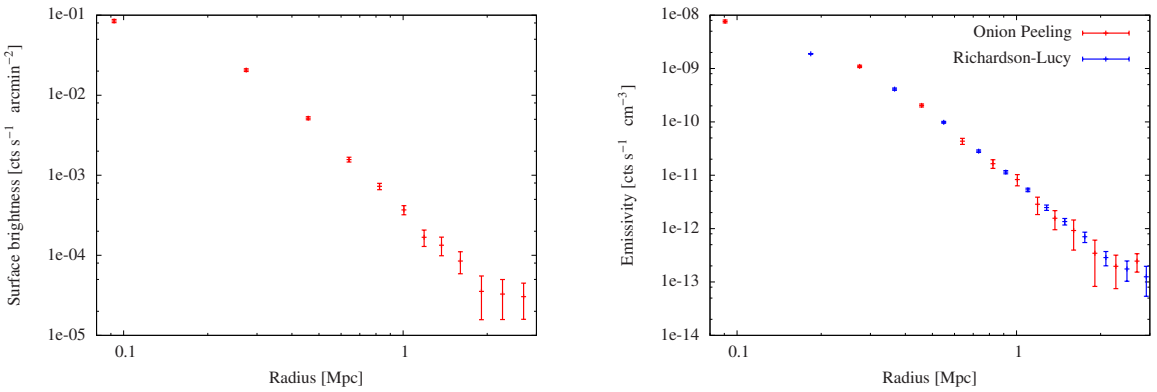

(a) (b)

Figure 5.3: (a) Surface brightness profile obtained with ROSAT. (b) Reconstructed emissivity using the RL-method (blue) and the onion peeling method (red).

our algorithm is compatible with the onion peeling method. Both methods agree within one standard deviation. However, this comparison does not exclude a bias present in both deprojection methods. From the emissivity we proceed to the three-dimensional density as follows: The temperature of Abell 1689 lies between 2 keV and 10 keV (Kawaharada et al., 2010), the observed energy band of 0.4 to 2 keV is below the bremsstrahlung cut-off energy. In this regime the emissivity depends only weakly on the temperature. Therefore, we can express the electron density as

$$\frac{\rho_\mathrm{e}}{\rho_{\mathrm{e},0}} = C\sqrt{\frac{j_\mathrm{band}}{j_{\mathrm{band},0}}} \tag{5.37}$$

with the emissivity j_band in the specific energy band and quantities with the subscript '0' refer to an arbitrary radius. The constant C is found by matching the reconstruction to the density profile from Eckert et al. (2013) at 1 Mpc. Figure 5.4(a) shows the comparison of our reconstruction with the onion peeling method for the electron density. Again the results are in very good agreement and well within one standard deviation except for the innermost data point at $r \approx 0.2$.

Further, by assuming a polytropic stratification of the ICM and using the relation from Eq. (3.31) the temperature profile can be expressed as a function of the emissivity,

$$T(r) \propto \rho(r)^{\gamma-1} \propto j_\mathrm{band}^{(\gamma-1)/2}\,. \tag{5.38}$$

To obtain the temperature profile, we first have to infer the adiabatic index γ. For this purpose we use the pressure profile by Nagai et al. (2007) and the corresponding parameters from Planck Collaboration (2013b). By fitting the polytropic equation, we infer an adiabatic index of $\gamma = 1.19 \pm 0.04$. Given this index, we can derive the temperature profile by applying Eq. (5.38) and compare it to the onion peeling method and direct measurements. Figure 5.4(b) shows the reconstructed temperature profile and the one-sigma region, again found by bootstrapping (one bootstrap for each bound on the adiabatic index). The dark-blue curve shows the reconstruction with $\gamma = 1.19$. Figure 5.4(b) compares our reconstruction to the onion peeling method (red), to the data from Susaku (Kawaharada et al., 2010) (black), and to the data from XMM-Newton (Snowden et al., 2008) (grey). The data from Susaku and XMM-Newton were obtained by spectral fitting. According to these results the polytropic assumption is well justified as we can reproduce the decrease in the temperature profile accurately.

However, a cautionary remark has to be made here: In the inner part of galaxy clusters cooling processes may occur, rendering the cooling time shorter than the Hubble time (e.g Fabian, 1994), thus changing the adiabatic index. It may imply that assuming a constant adiabatic index is a bold assumption as we do not take this effect into account in our model. Another problem is the assumption of

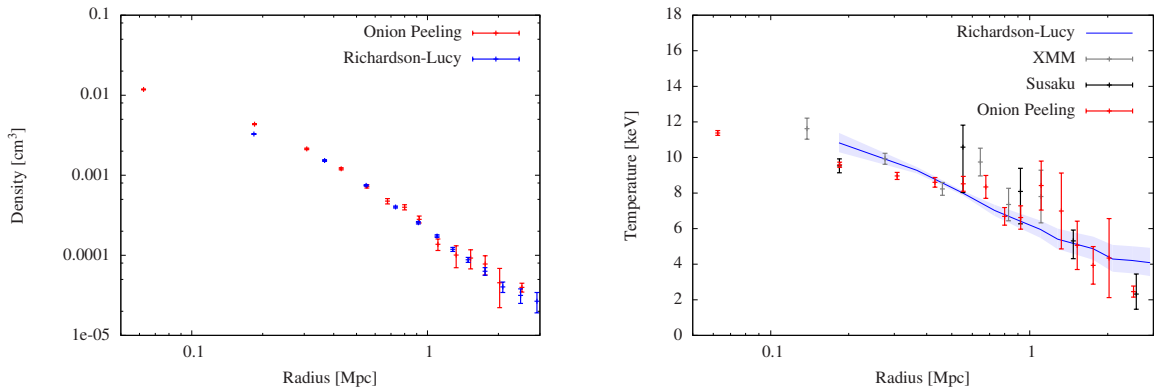

(a) (b)

Figure 5.4: (a) Comparison of the reconstructed density profile using the onion peeling method (red) and the RL-method (blue). (b) Temperature profile of A1689 obtained from Susaku (black), XMM-Newton (grey), using the onion peeling method (red) and the RL-method (blue).

hydrostatic equilibrium as kinematics and X-ray studies suggest deviations from it for Abell 1689. Findings from Sereno et al. (2013); Andersson & Madejski (2004) indicate that Abell 1689 might be a merging cluster aligned with the line-of-sight and thus not relaxed.

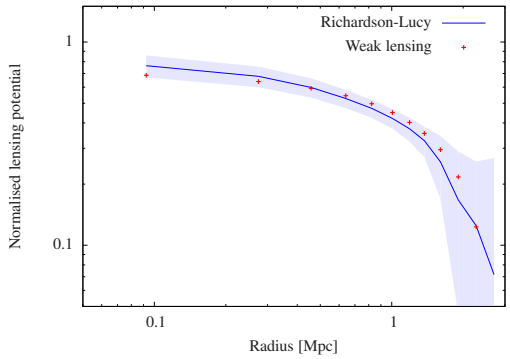

Figure 5.5: Reconstructed and normalised lensing potential of Abell 1689 obtained with the RL-method (blue) and with *SaWLens* (red, credits: J. Merten). The light-blue area indicates the two-sigma region.

However, we do calculate the lensing potential and compare it with a weak-lensing reconstruction obtained with *SaWLens*, shown in Fig. 5.5. We proceed in the same manner as we did for the emissivity. Only the normalisation is chosen such that both profiles are evaluated at the same positions which is achieved by interpolating the profile obtained with weak lensing. Both profiles further obey the normalisation constraint from Eq. (5.4). Our reconstructed profile roughly reproduces the shape of the lensing potential obtained with the weak-lensing reconstruction. As the lensing reconstruction is based on weak-lensing data only, it is expected to be biased as well. Even though the assumption of spherical symmetry seems not justified, our reconstruction still reproduces the lensing potential within two standard deviations.

5.7 Testing the influence of the free parameters α and L

In the above section we used a bootstrapping method to quantify the uncertainty of our reconstruction. The parameters α and $L_{\max}$ were constrained according to Section 5.5. But now we consider how these parameters influence a reconstructions if they are chosen freely.

We take the surface brightness data from Abell 1689 and reconstruct them in the following two ways:

(1) We fix the strength of regularisation α and reconstruct with different values of $L_{\max}$.

(2) We fix the smoothing scale $L_{\max}$ and carry out the reconstruction for different values of α.

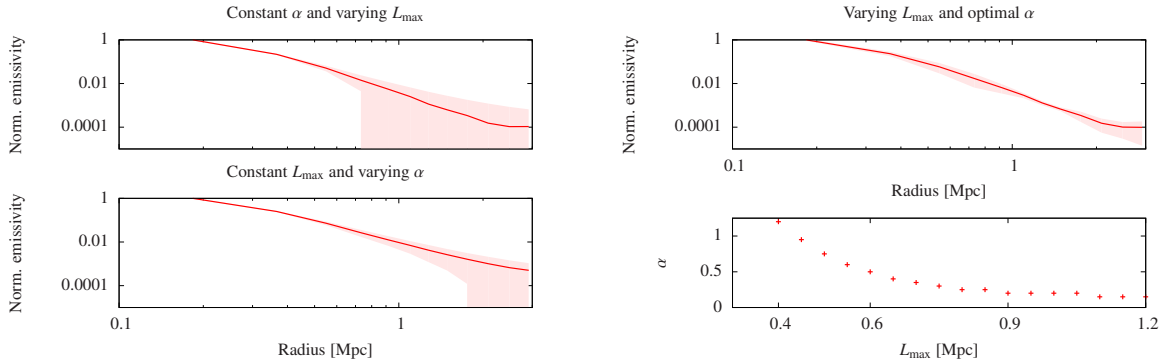

(a) (b)

Figure 5.6: (a) Upper panel: Reconstructed and normalised emissivity for Abell 1689 with a constant value for $\alpha = 0.2$ and different values for $L_{\max}$. The light-red area illustrates the three-sigma region. Lower panel: Same as the upper panel but with fixed $L_{\max} = 1.05\,\mathrm{Mpc}$ and varying α. (b) Upper panel: Same as the lower panel of (a) but now the optimal α was determined according to Eq. (5.36) with a fixed value for $L_{\max} = 1.05\,\mathrm{Mpc}$. Lower panel: The best-fitting α in dependence of the chosen value of $L_{\max}$.

We fix the chosen value $\alpha = 0.2$ and sample $L_{\max}$ in the range of $0.4 \leq L_{\max} \leq 1.35\,\mathrm{Mpc}$. The mean value of all reconstructions with one value fixed and the three-sigma region are shown in Fig. 5.6(a). For the second test, we set the maximum value of the smoothing scale constant at $L_{\max} = 1.05\,\mathrm{Mpc}$ and reconstruct the emissivity of Abell 1689 with different values for α in the range of $0.05 \leq \alpha \leq 1.0$. For these reconstructions we calculate the mean value and the corresponding standard deviation.

In the same way we can test how the optimisation from Eq. (5.36) influences the standard deviation of our reconstruction. We iterate the same range of values for $L_{\max}$, but this time we determine the best-fitting α by applying Eq. (5.36). This result is shown in the upper panel of Fig. 5.6(b), and the lower panel shows the optimal α in dependence of $L_{\max}$.

We summarise here the findings from Fig. 5.6:

- The scatter in Fig. 5.6(a) is large in both panels for large radii. But the upper panel shows an even larger scatter which implies that the reconstruction is sensitive to the chosen value for $L_{\max}$.
- In the lower panel Fig. 5.6(a) the mean result is slightly biased to higher values for larger radii. This fact is due to the mentioned under-fitting for large values of α, see also Section 5.5.
- We further see from Fig. 5.6(a) that the maximum scale of the smoothing scale $L_{\max}$ has large influence on the outskirts of the radial profile, indicating the need of a properly chosen $L_{\max}$.
- The scatter in the upper panel in Fig. 5.6(b) is much smaller than in both panels of Fig. 5.6(a). According to this result the optimisation criterion from Eq. (5.36) is able to adjust the value of α to the given value of $L_{\max}$. This is a very important finding as it allows us to choose a value of $L_{\max}$, which may not be the best-fitting one. But still we will have reliable results once the algorithm is allowed to assess the best-fitting α.
- The behaviour of the best-fitting α with a changing value of $L_{\max}$ is as expected as both parameters have a smoothing effect on the deprojection: The larger the smoothing scale the less regularisation is needed – α decreases with $L_{\max}$.

5.8 Summary and conclusion

In the this chapter we generally explained the Richardson-Lucy deprojection method and reformulated this method in two special geometries, the spherical and spheroidal geometry. With this method we are able to retrieve the deprojection of radial profiles for spherically symmetric distributions and the deprojection of two-dimensional spheroidal distributions. The Richardson-Lucy method includes two variables, the strength of regularisation α and the scale of the floating default kernel L. Both of them have to be assessed with the specific data set to be considered. However, we made the scale of the floating default kernel dependent on the examined position, allowing us to change the S/N profile of the data supplied to the algorithm. On the other hand both parameter – α and $L_{\max}$ – are chosen in such a way that the difference between the projection of the deprojected data and the data itself is minimal.

We also note here a major difference between the spherical and spheroidal deprojection method: In both geometries we average over a given number of pixels of our image as we carry out the integration along the three-dimensional contour. However, the spherical geometry in comparison to the spheroidal has one degree of freedom more, due to the additional symmetry. In the spherical case we exploit this symmetry explicitly by binning our data in annuli around the cluster centre. Afterwards we integrate over specific bins, which are given by the kernel. In the spheroidal case we only average over a given number of pixels as we integrate along the three-dimensional contour, as indicated by the kernel. In this way the average in the spherical case is taken over more pixels than in the spheroidal one. This will, as we see later in this work, directly influence the possible usage of data sets, as it gives constraints on a needed S/N.

Furthermore, we compared our algorithm in spherical symmetry to the existing onion peeling method from Eckert et al. (2013) by applying it to the massive galaxy cluster Abell 1689. We were able to show, considering our results concerning the obtained emissivity profiles, that both deprojection methods yield the same result within their errors. Even more, the agreement of the retrieved temperature profile and temperature profiles inferred from spectral fitting lies well within the one-sigma region. Further, the temperature profile seems to obey a polytropic relation or at least it is not in conflict with one. This also implies that in the case of Abell 1689 the assumption of spherical symmetry, the ideal gas equation and a polytropic stratification is applicable.

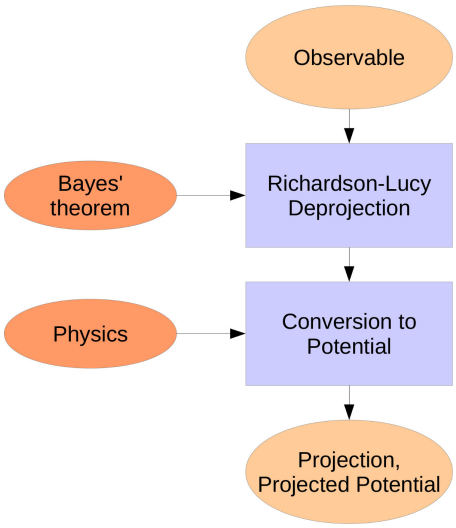

Figure 5.7: Schematic overview of our used reconstruction method. It involves a deprojection, assumptions about the physical state of the ICM and a projection (credits: M. Bartelmann).

From the obtained emissivity profile we proceeded to the three-dimensional gravitational potential by using Eq. (3.47) and further on to the two-dimensional lensing potential by applying Eq. (3.11). This allowed us to compare our retrieved result with the lensing potential of Abell 1689 obtained with weak-lensing data using *SaWLens*. This comparison showed a good agreement between both methods. The overall scheme of our used reconstruction method is depicted in Fig. 5.7. It uses the RL-method for deprojection and links the deprojected observable with the gravitational potential under given assumptions about the ICM. Finally, an estimate proportional to the lensing potential is obtained by a projection along the line-of-sight.

In the last section we have evaluated how the results from Section 5.6 are biased by the free parameters α and $L_{\max}$. We have shown that the search for the best-fitting value of α for a given value of $L_{\max}$ lowers the scatter in the reconstruction tremendously. We have also shown that α exhibits the assumed behaviour with a varying $L_{\max}$: It decreases as the smoothing scale increases.

Chapter 6

6 Reconstruction of the mass distribution of clusters using the thermal Sunyaev-Zel'dovich effect

The thermal SZ effect probes the ICM embedded in the dark-matter potential well of a galaxy cluster as the background photons of the CMB undergo inverse Compton scattering. This effect has been explained in Section 3.2.2 as well as the link between the specific intensity change and the lensing potential, which allows us to reconstruct the latter. This involves the deprojection of the observed SZ signal to obtain the effective pressure of the ICM, which is then related to the gravitational potential. As we want to infer the three-dimensional structure of the galaxy cluster from a two-dimensional distribution, we clearly need certain symmetry assumptions.

To test our reconstruction algorithm with the deprojection method from Chapter 5, we start with the explained scheme for spherical symmetry (see Section 5.3). We use mock data of a spherical galaxy cluster with an NFW density profile. The mock thermal SZ signal includes the noise characteristics of the *Atacama Large Millimeter/submillimeter Array* (ALMA).

Proceeding to a more realistic scenario, we improve our cluster model by applying our method to a cluster based on an N-body/hydrodynamical simulation with a ΛCDM model. The simulation is taken from Meneghetti et al. (2010b), based on original work of Saro et al. (2006), and was explained in detail in Section 4.4.1. To this specific cluster simulation we also apply our Richardson-Lucy deprojection algorithm for spheroidal cluster geometry from Section 5.4. The result of our reconstruction is then compared to the real underlying lensing potential retrieved from the simulation itself.

The contents of this chapter have been published in Konrad, Majer, Meyer et al. (2013) and Majer, Meyer, Konrad et al. (2013).

6.1 Simulation of ALMA observations

In this section we will briefly discuss the realistic noise model our mock cluster is embedded in. As possible noise sources we take into account background fluctuations due to unresolved clusters and the instrumental noise of ALMA itself. Furthermore, we include an estimate of the fluctuations introduced by primary CMB anisotropies.

6.1.1 Background fluctuations due to unresolved clusters

Galaxy clusters unresolved by the telescope beam contribute a background noise level y_{bg} that needs to be taken into account in all following calculations. Clusters are unresolved if they appear (much) smaller than the beam size. The background signal is thus dominated by low-mass clusters (Bartelmann, 2001). Since an ideally homogeneous background could be removed from the data, we only have to consider the average background fluctuation level Δy_{bg}. The mean background level contributed by unresolved clusters with the differential mass function $n(M, z)$ is

$$y_{\mathrm{bg}} = \int \mathrm{d}M \int \mathrm{d}V \, Y(M, z) \, n(M, z) \,, \tag{6.1}$$

where the mass- and redshift-integrations have to be carried out over that area in the mass-redshift plane where clusters are unresolved. The integrated Compton-y parameter $Y(M, z)$ of a cluster with mass M at redshift z is

$$Y = \int \mathrm{d}^2 s \, y(\boldsymbol{s}) = \frac{k_{\mathrm{B}} T}{m_{\mathrm{e}} c^2} \frac{\sigma_{\mathrm{T}}}{D_{\mathrm{d}}^2} N_{\mathrm{e}} \,, \tag{6.2}$$

where the angular-diameter distance D_{d} to the cluster appears and the total number of electrons N_{e}. We choose the cluster mass function $n(M, z)$ described by the Sheth-Tormen model (Sheth & Tormen, 1999) (see also Section (2.7) for further details),

$$n(M, z) = A \sqrt{\frac{2}{\pi}} \left(1 + \frac{1}{\nu^{2q}}\right) \frac{\rho_{\mathrm{bg}}}{M} \frac{\mathrm{d}\nu}{\mathrm{d}M} \exp\left(-\frac{\nu^2}{2}\right) M \,. \tag{6.3}$$

The number of background sources follows a continuos probability distribution. If one neglects any cluster correlations and a constant background which could be removed, the rms due to background fluctuation is

$$\sigma_{\mathrm{bg}} = \left[\int \mathrm{d}M \int \mathrm{d}V \, Y^2(M, z) \, n(M, z) \right]^{1/2} . \tag{6.4}$$

6.1.2 Instrument noise

Another relevant source of noise is the measurement noise of the telescope and the detector. We assume that the measurement error of the telescope has a Gaussian distribution with standard deviation σ_{Tel} around zero, with σ_{Tel} depending on the telescope and detector configuration and the setup of the specific observation.

Since we need a resolution for our simulation that is comparable to other observations of massive galaxy clusters, we choose the Atacama Large Millimeter/submillimeter Array (ALMA) as an example telescope for achieving sufficiently precise thermal SZ observations. For all simulations presented in the remainder of this work, we use the following configuration of ALMA: All $N_{\mathrm{ant}} = 32$ antennae are assumed to be available with a yet to set baseline. This configuration has then a given angular resolution in a frequency band chosen to be centred on $\nu = 116\,\mathrm{GHz}$. Its bandwidth is assumed to be $\Delta\nu = 7.5\,\mathrm{GHz}$. According to the ALMA user manual (Lundgren, 2012) the point-source sensitivity σ_{Tel} of ALMA is

$$\sigma_{\mathrm{Tel}} = \frac{2 k_{\mathrm{B}} T_{\mathrm{sys}}}{\eta_{\mathrm{q}} \eta_{\mathrm{c}} A_{\mathrm{eff}} \sqrt{N_{\mathrm{ant}}(N_{\mathrm{ant}} - 1) n_{\mathrm{p}} \Delta\nu t_{\mathrm{int}}}} \,, \tag{6.5}$$

where T_{sys} is the temperature of the system[2], η_{q} the quantum efficiency ($\eta_{\mathrm{q}} = 0.96$), η_{c} the correlator efficiency ($\eta_{\mathrm{c}} = 0.88$), A_{eff} the effective area of an individual antenna, n_{p} the number of polarisation states ($n_{\mathrm{p}} = 2$), and t_{int} is the integration time. Given the standard deviation of the instrument noise, the final observed image can be simulated assuming a Gaussian distribution of the signal with the variance σ_{Tel}^2.

[2]The system temperature is a combination of the receiver temperature, sky temperature and the ambient temperature (Lundgren, 2013).

6.1.3 CMB fluctuations

On small angular scales, roughly around 1′, the primary CMB anisotropy may be negligible due to its exponential cut-off at these length scales. However, observing massive galaxy clusters implies the observation of a large patch of the sky. Thus, on cluster scales one has to take primary CMB anisotropies, as a source of background noise, into account.

As the thermal SZ effect measures the CMB intensity change due to a cluster, we need to quantify the intrinsic CMB intensity change across the field. Since the observation is done with a beam of finite width, the CMB signal needs to be convolved with this beam B. The correlation function $\xi(r)$ between two points on the sky in flat-sky approximation is then given as

$$\xi(r) = \int \mathrm{d}k \, \frac{k}{2\pi} P(k) \, |\hat{B}(k)|^2 \, J_0(k\, r) \tag{6.6}$$

with the angular power spectrum $P(k)$ of the CMB and the Fourier transform $\hat{B}$ of the beam profile and the Bessel function of 0^{th}. The correlation function depends only on the distance, allowing us to evaluate the variance of these two points as the average over a circular FOV with radius R:

$$\begin{aligned} \sigma^2_{\text{CMB}} &= \frac{1}{\pi R^2} \int \mathrm{d}^2 r \, \xi(r) \\ &= \frac{2}{R^2} \int_0^R r \, \mathrm{d}r \int \frac{\mathrm{d}^2 k}{(2\pi)^2} P(k) \, |\hat{B}(k)|^2 \, \mathrm{e}^{i \boldsymbol{k} \cdot \boldsymbol{r}} \\ &= \frac{1}{\pi R} \int \mathrm{d}k \, P(k) \, |\hat{B}(k)|^2 J_1(k\, R) \end{aligned} \tag{6.7}$$

with the Bessel function of 0^{th} and 1^{st} order, J_0 and J_1 respectively. This variance may now be calculated and included in our noise model. The CMB power spectrum is computed using CAMB (Lewis et al., 2000).

6.2 Application to mock data with spherical symmetry

To test the algorithm sketched in Section 3.2.2, we simulate the thermal SZ signal of a massive galaxy cluster, assuming spherical symmetry, hydrostatic equilibrium, and an NFW density profile. We choose the concentration parameter $c = 5$ and a spatially flat standard ΛCDM cosmology with $\Omega_{\text{m0}} = 0.3$ and $\Omega_{\text{b0}} = 0.04$. The properties of the ICM are chosen as follows:

- The plasma contains 75% hydrogen and 25% helium by mass.
- Both hydrogen and helium are completely ionised.
- The gas-mass fraction equals the universal baryon mass fraction $f_{\text{b}} = \Omega_{\text{b}}/\Omega_{\text{m}}$.
- The gas has a constant polytropic index of $\gamma = 1.2$.

The gas density and temperature profiles are then calculated using Eqs. (3.35) and (3.37). To obtain a temperature profile which drops to zero at a large radius, we choose a cut-off radius for the gravitational potential of $r_{\text{cut}} = r_{200}$. Given the density and temperature profiles, the specific intensity change ΔI_{SZ} can be calculated using Eq. (3.23).

The mass of the cluster is chosen to be $5 \times 10^{14}\, \mathrm{M}_\odot\, h^{-1}$ at redshift 0.2, the scale radius is $r_{\text{s}} = 0.25\, \mathrm{Mpc}\, h^{-1}$.

Since the above noise contributions from Sections 6.1.1, 6.1.2, and 6.1.3 are not correlated with each other, the total uncertainty is then given by Gaussian error propagation. For our mock simulation this results in $S/N = 1.25$ per pixel at the scale radius for the chosen ALMA configuration. With this, the radial profile of the thermal SZ signal can be obtained by averaging the simulated image in annuli around the cluster centre. This profile is shown in Fig. 6.1 for one realisation of the noise for the simulated galaxy cluster. At a radius $s \gtrsim 0.8\,\mathrm{Mpc}\,h^{-1}$ (i.e. $3 \times r_\mathrm{s}$), the cluster signal sinks below the noise level and becomes nearly constant.

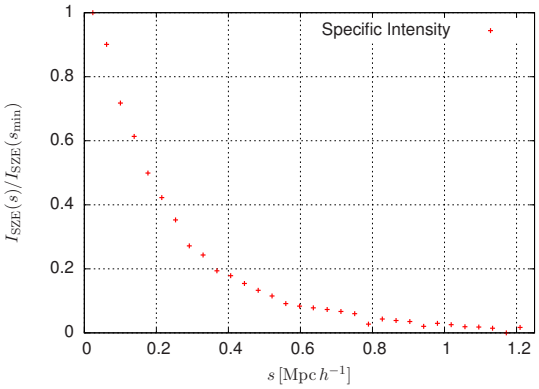

Figure 6.1: Azimuthally averaged and normalised specific intensity in dependence of the angular radius s. The displayed maximal range of radial values corresponds to the virial radius of the cluster.

Applying our Richardson-Lucy algorithm to the simulated specific intensity change ΔI_SZ returns an estimate for the three-dimensional effective pressure. Through Eq. (3.41), an estimate of the gravitational potential is obtained. For the specific data set shown in Fig. 6.1, the estimate for the gravitational potential is shown in Fig. 6.2(a). The reconstruction is carried out with $\alpha = 0.25$ and $L_\mathrm{max} = 0.31\,\mathrm{Mpc}\,h^{-1}$. Both values are the best-fitting ones according to the procedure explained in Section 5.5. From the obtained gravitational potential we can carry out the line-of-sight integration to retrieve the lensing potential. The comparison of our reconstruction and the true lensing potential inferred from the simulation is shown in Fig. 6.2(b). The reconstruction is reliable to a maximum radius of $r \approx 0.7\,\mathrm{Mpc}\,h^{-1}$ (cf. Fig. 6.3) as beyond this radius the deviations from the true lensing potential grow.

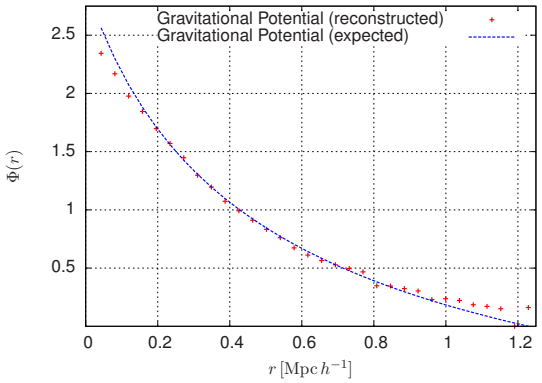

(a)

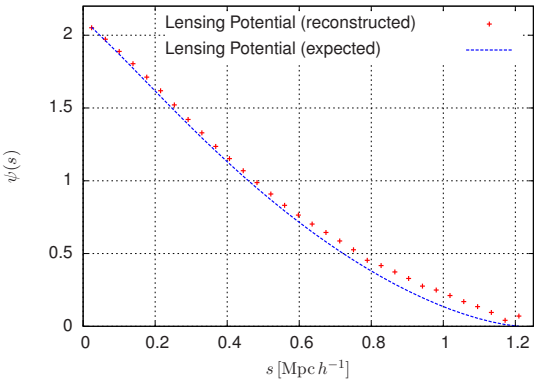

(b)

Figure 6.2: (a) Comparison between the recovered and normalised gravitational potential and the expected result, α was chosen by the best fit (see text). (b) Comparison between the normalised lensing potential ψ and the expected result.

We quantify the error of our algorithm by 100 bootstrap samples of the noise model described above, which yields different realisations of the same cluster. To these we apply our reconstruction algorithm. From all reconstructions we calculate the rms deviation of the recovered lensing potential from its true profile, according to,

$$\mathrm{rms}(s;\psi,\psi_\mathrm{true}) = \left[\frac{1}{N}\sum_{n=1}^{N}\frac{(\psi(s)-\psi_\mathrm{true}(s))^2}{\psi^2_\mathrm{true}(s)}\right]^{1/2}. \tag{6.8}$$

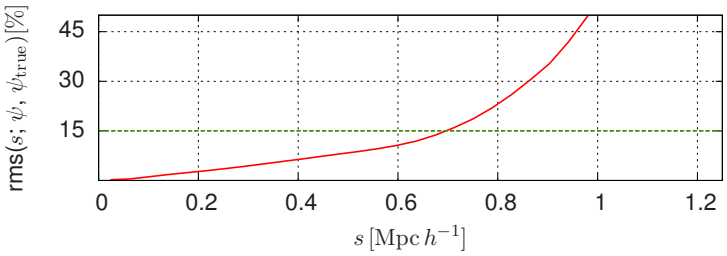

Figure 6.3: Relative rms deviation of the projected potential ψ from the true profile ψ_{true}, derived from 100 realisations of the modeled galaxy cluster. The green line shows the 15% level for comparison.

The rms obtained from this bootstrap is shown in Fig. 6.3 together with a reference line at the 15% level of deviation (green line). We achieve a relative accuracy of less than 15% for radii smaller than $\approx 0.7\,\text{Mpc}\,h^{-1}$. At larger radii, the rms reaches much higher values. This is clearly due to the increasing noise at large radii, since the S/N per pixel at the virial radius is below 0.02. Furthermore, the true lensing potential approaches zero by construction at the virial radius, whereas our reconstruction remains finite and positive.

6.3 Application to a hydrodynamical simulation assuming spherical symmetry

Up to now we have relied on spherical symmetry and an ICM which is in hydrostatic equilibrium. But it is well known that these assumptions are not necessarily applicable for observed galaxy clusters. Even though our algorithm so far assumes spherical symmetry and hydrostatic equilibrium, we test our method on a realistic data set that is not restricted in this sense.

Our data set is taken from Meneghetti et al. (2010b) (see also references therein) and is based on an N-body/hydrodynamical simulation. This cluster may not be in hydrostatic equilibrium and is certainly not spherically symmetric (see Fig. 6.4[3] and Section 4.4.1 for more details). Therefore both our assumptions may not be strictly fulfilled, but according to the quality of agreement we achieve below with our reconstruction, they are still applicable, at least within the measurement uncertainty.

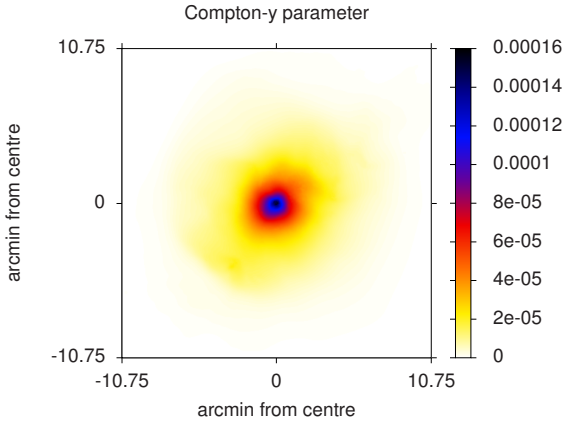

Figure 6.4: The Compton-y parameter as obtained from the hydrodynamical simulation.

Our data set has a field of view of 21.5′ and a resolution of 512×512 pixels (i.e. 2.51″ per pixel). For the same FOV we have the convergence map at hand to estimate the underlying lensing potential. We obtain the lensing potential by solving Poisson's equation numerically with a fast-Fourier transform using the surface-mass density of the cluster.

The Compton-y parameter from Fig. 6.4 is used to create a mock observation of this cluster with ALMA by adopting the appropriate parameters and adding noise as described in Section 6.1.1, 6.1.2, and 6.1.3. In this manner we obtain a simulation with a resolution of 5″ and a $S/N = 1.27$ per pixel at the scale radius (i.e. $s \approx 2.4'$). The radial profile of the normalised specific intensity is shown in Fig. 6.5(a). This profile is deprojected with our algorithm and used to infer the lensing potential. This

[3]The image was produced with Splotch: http://www.mpa-garching.mpg.de/~kdolag/Splotch

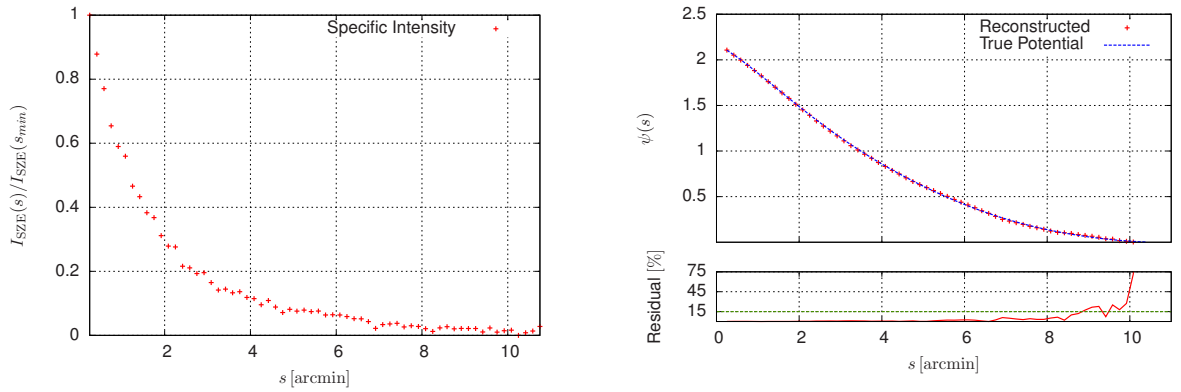

(a) (b)

Figure 6.5: (a) The computed specific intensity, derived from the Compton-y parameter obtained from the hydrodynamical simulation. The radial profile was produced with ALMA properties at 116 GHz, a resolution of 5″ and $S/N = 1.27$ per pixel at the scale radius. (b) Upper panel: Normalised reconstruction of the lensing potential compared with the real lensing potential from the hydrodynamical simulation ($\alpha = 0.4$ and $L_{\max} = 1.75'$). Lower panel: The relative modulus of the residual from the reconstruction and the true lensing potential. The green line indicates the 15% level.

is then compared to the real lensing potential mentioned above. Crucial for the result is the knowledge of the polytropic index, for which we take a value of $\gamma = 1.22 \pm 0.02$. This value is inferred by fitting the the surface brightness and temperature profile presented in Meneghetti et al. (2010b), which constrains the index η from Eq. (3.41) to $\eta \approx 5.55$.

Referring to Fig. 6.5(a), the mean noise level of the input data is crucial for the reconstruction to work reliably as the noise exceeds the signal at $s \approx 9'$. Note that the virial radius, taken as r_{200} from the best-fitting NFW profile, of this cluster lies at $r_{\rm vir} \approx 8'$. The effect is visible as the signal approaches a constant corresponding to the noise level.

However, Fig. 6.5(b) shows that up to a radius of $s \approx 8' - 9'$ our reconstruction reproduces the lensing potential well. The relative deviation, see the lower panel in Fig. 6.5(b), of the reconstruction from the underlying real lensing potential shows only deviations which do not exceed 15% within the virial radius.

6.4 Application to a hydrodynamical simulation assuming spheroidal symmetry

The galaxy cluster considered in the section above is not spherically symmetric, obvious from Fig. 6.4. This statement is even more evident once the axis ratios from Tab 4.1 are evaluated. However, referring to Section 5.4, the adopted Richardson-Lucy deprojection method may also be applied to such spheroidal objects.

We test our method for spheroidal geometry on the same simulation as described in Section 4.4.1. This time, however, we need a more robust signal as we do not average in annuli anymore (see the discussion in Section 5.8). Thus a much higher S/N compared to the data set used in Section 6.3 has to be created. This certainly limits crucially the resolution we can effectively use for our algorithm. We enhance the S/N by lowering the resolution to 64×64 pixels and set the integration time to 24 h. This results in a $S/N = 1.36$ at the virial radius, roughly at $r_{\rm vir} \approx 8'$. The obtained specific intensity change at a frequency of 116 GHz is shown in Fig. 6.6 together with the virial radius (black circle).

This data set is now reconstructed using the spheroidal implementation of our Richardson-Lucy algorithm according to Section 5.4. We use $\alpha = 0.24$, found by applying Eq. (5.36) and the method

explained in Section 5.5. The smoothing scale is taken as $L_{\max} = 1.6'$ and increases quadratically rather than linearly as explained in Section 5.5. This accounts for the greater number of pixels with a low S/N towards the outskirts of the cluster. Further, we need the inclination angle ι, which we take again from Meneghetti et al. (2010b) as $\iota = 84°$.

As in Section 6.3 we use an adiabatic index of $\gamma = 1.22$ to calculate the exponent η. The gravitational potential is then obtained from the deprojected specific intensity change. Projecting the gravitational potential along the line-of-sight then gives a scaled version of the lensing potential. We now have the freedom to subtract or add a constant to the lensing potential as well as to multiply our reconstruction with a constant. By exploiting this freedom we scale the lensing potential to a maximum value of $\psi_{\max} = 1$ and add a constant such that the mean of the reconstructed potential is equal to zero at the boundaries. To compare our reconstruction with the true lensing potential we apply the same procedure to the real lensing potential.

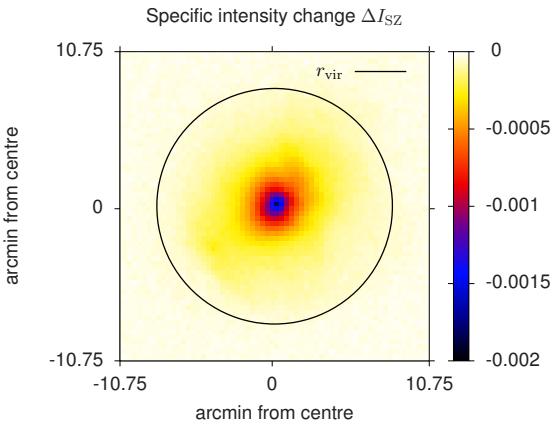

Figure 6.6: Specific intensity change obtained from the input data from Fig. 6.4 for a specific configuration of ALMA (see text for details). The resolution of 64×64 pixel corresponds to an angular resolution of $20''$.

Figure 6.7(a) shows the reconstructed lensing potential scaled and shifted as mentioned above together with the virial radius (white line). The green curve shows the 15%-contour of deviation regarding the true underlying lensing potential. The true lensing potential is shown in Fig. 6.7(b) again with the virial radius of the cluster (white line). The mentioned 15%-contour is obtained from the absolute residual shown in Fig. 6.7(c). We see that the reconstruction is roughly below the 15% level nearly up to the virial radius. The corners in our FOV tend to deviate very strongly from the true result which is obvious from our reconstruction method: According to Fig. 5.2 the cluster is assumed to have a symmetry axis along the y-direction in the plane of the sky. But from Fig. 6.4 we see that the cluster is rotated clockwise by an angle $\alpha \approx 45°$ away from this symmetry axis. This means that we first have to rotate the input data losing information outside the incircle. These missing values are then replaced by a constant extrapolation as explained in Section 5.4. Clearly, the reconstruction obtained in these regions contains no meaningful information on the lensing potential.

For the spherically symmetric case the scale of the smoothing scale $L_{\max}$ has been chosen by the algorithm itself by applying the method explained in Section 5.5. This procedure is very time-consuming and not feasible for this two-dimensional data set. Therefore, we only test for the best-fitting α, whereas $L_{\max}$ is chosen, guided by the points mentioned in Section 5.5. However, we test a control sample with a few different values of $L_{\max}$ covering a reasonable range (i.e. 5% – 25% of the maximum value for R). All of them yield approximately the same result once we allow the strength of regularisation α to vary. By adopting a quadratically increasing smoothing scale, we further limit the effect of $L_{\max}$ in the cluster centre.

Comparing the three panels from Fig. 6.7, we can make following statements:

- The reconstruction algorithm in spheroidal geometry is capable of reproducing the elliptical shape of the lensing potential.
- For regions with a high S/N the reconstruction is reliable in reproducing the exact values of the lensing potential.
- As soon as the noise exceeds the signal, deviations from the real lensing potential are large.

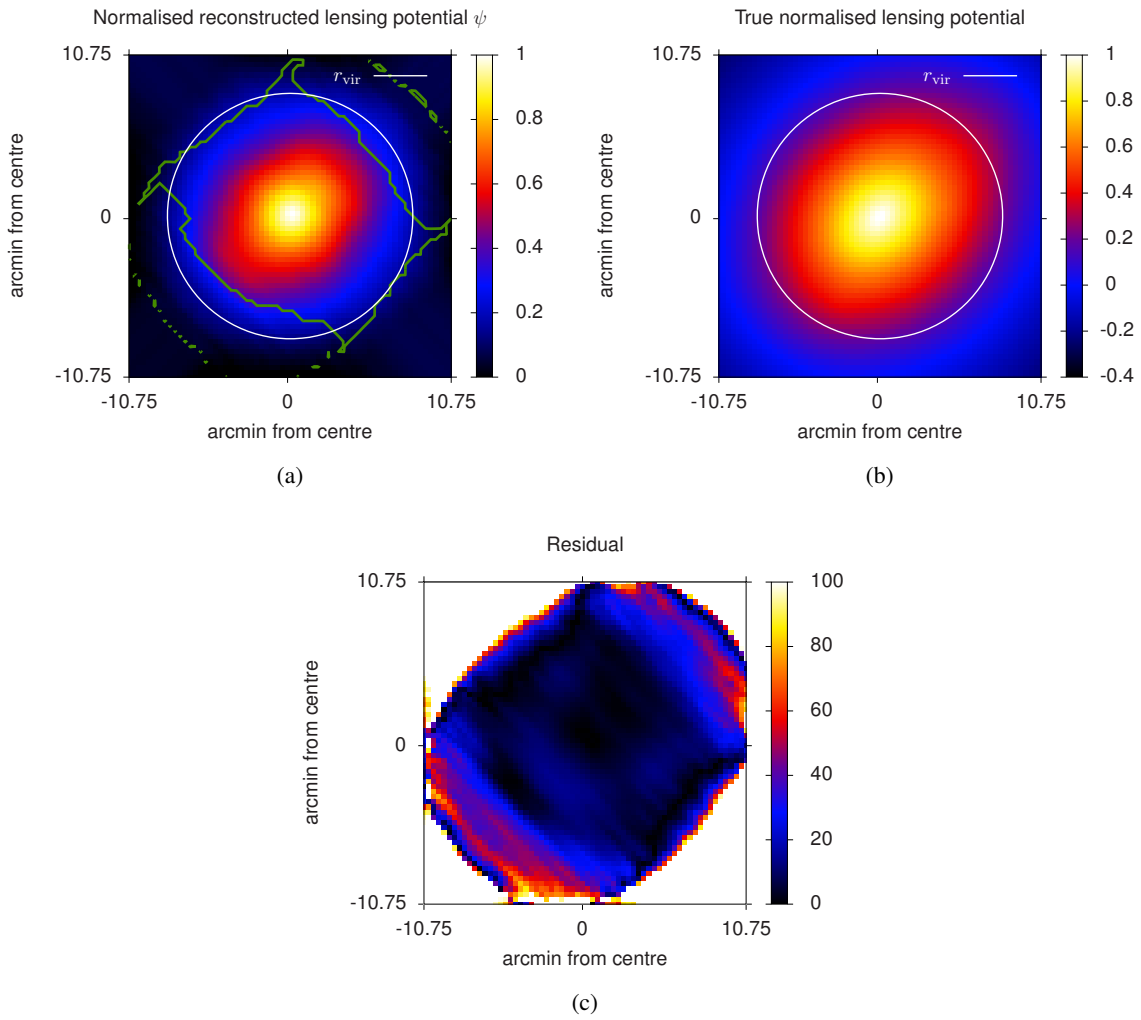

Figure 6.7: (a) Reconstructed lensing potential from the specific intensity change shown in Fig. 6.6. The white circle corresponds to the virial radius, and the green contour depicts a 15% deviation from the real underlying lensing potential. (b) True lensing potential as obtained from the hydrodynamical simulation. (c) Modulus of the relative residual from (a) and (b).

6.5 Summary and conclusion

In this chapter we showed how the observable provided by the thermal SZ effect in clusters, i.e. the relative intensity change of the CMB observed through the hot intracluster plasma, can be connected to the projected, two-dimensional lensing potential. The final goal of this study is to bring all cluster observables – strong and weak gravitational lensing, X-ray emission, the thermal SZ effect and ultimately also galaxy kinematics – on a common ground to use all of them in a joint reconstruction procedure which recovers the lensing potential best compatible with all these observables.

Under the assumption of hydrostatic equilibrium, a polytropic gas stratification and an ideal gas, we already derived in Section 3.2.2 how the Compton-y parameter is related to the gravitational potential. This allowed us to construct an algorithm beginning with the Richardson-Lucy deprojection of the observed specific intensity change, which is proportional to the Compton-y parameter, into the effective pressure. The Richardson-Lucy deprojection was the first step in the algorithm requiring symmetry assumptions. For simplicity, not by necessity, we chose to assume spherical symmetry initially. The deprojected Compton-y parameter was then readily converted to the three-dimensional gravitational potential, which was finally projected along the line-of-sight.

We simulated the thermal SZ data with a spherically-symmetric NFW density profile for the underlying mass distribution. The cluster had a mass of $M = 5\times10^{14}\,\mathrm{M}_\odot\,h^{-1}$ at redshift 0.2. It was observed with the signal-to-noise characteristics of one specific configuration of the ALMA interferometer. In addition to instrumental noise, we included background fluctuations in the thermal SZ signal due to unresolved clusters and CMB anisotropies. We sampled this cluster with different realisations of our assumed noise model (see Section 6.1). For each of these mock observations of a galaxy cluster the lensing potential was reconstructed using the algorithm for spherical symmetry from Section 5.3. In this way, we could calculate the rms deviation from the mean of the reconstructions and the real lensing potential obtained from the NFW density profile. The results looked very promising: The three- and two-dimensional potentials were well reproduced with our method. The bootstrapping showed relative rms accuracies of the recovered, two-dimensional lensing potential at or below the 15% level up to a cluster-centric radius of $s \lesssim 0.7\,\mathrm{Mpc}\,h^{-1}$.

Furthermore, we made our input data more realistic by replacing the mock catalogues with a cluster from an N-body/hydrodynamical simulation. We used a specific configuration of the ALMA interferometer which enabled us to carry out the spherical reconstruction method in a more realistic scenario. The simulated cluster was neither spherically symmetric nor in hydrostatic equilibrium. Nevertheless, we were able to reconstruct a large fraction of the galaxy cluster below a relative deviation of 15%.

Assuming spherical symmetry for galaxy clusters is in some tension to the approximated elliptical shape of clusters and does not agree with the model of structure collapse according to the Zel'dovich approximation (see Section 2.6.3) either. However, due to the nature of observations we need at least one symmetry assumption if we want to infer the three-dimensional structure of the cluster.

We extended the spherical RL to spheroidal cluster geometry already in Section 5.4, but applied it in this chapter to data for the first time. We used the same realistic cluster from the simulation in Section 6.3, taken from Meneghetti et al. (2010b). We changed the configuration of the ALMA interferometer, i.e. we changed the resolution and observation time, to achieve a higher S/N, which is needed for a two-dimensional reconstruction (see the discussion in Section 5.8). Again the results were very promising as we were able to reconstruct the lensing potential up to a radius of $r \approx 0.9\times r_{\mathrm{vir}}$ with a relative residual of less then 15%. This is clearly a leap towards the combination of observations based on the thermal Sunyaev-Zel'dovich effect and observations based on gravitational lensing. By retrieving the two-dimensional lensing potential, we are now capable to implement an appropriate χ^2-term directly into the reconstruction scheme explained in Section 4.1.

Chapter 7

7 Reconstruction of the mass distribution of clusters using X-ray emission

So far we have studied the feasibility of recovering the lensing potential of massive galaxy clusters using the thermal Sunyaev-Zel'dovich effect. But in Section 3.2.3 we also presented a similar method to retrieve the lensing potential of clusters by using their X-ray emission. This idea follows the same concept developed so far: We want to combine the obtained results with other methods to infer the lensing potential, leading us to an overall best-fitting model.

By assuming the cluster to be in hydrostatic equilibrium and an ICM that follows a polytropic equation of state, we sketched a method which involves a deprojection. The overall scheme of the algorithm is identical to the one applied in Chapter 6, but due to the different physics of X-ray emission and its noise, we need to test the validity of our method separately.

As we have elaborated on the physics of the emission of X-rays due to thermal bremsstrahlung in Section 3.2.3, we now concentrate first on the simulation of such an observation. We use the properties of the *Chandra X-ray Observatory* (Chandra) to simulate mock data. As in the case of the thermal SZ effect we include a background noise model. We choose the same cluster properties as in Chapter 6: The simulated galaxy cluster has a spherically symmetric NFW density profile. We apply our reconstruction method to this mock data set, which contains the binned surface brightness of the cluster. As it turns out, we achieve a higher degree of accuracy in reconstructing the lensing potential due to the different noise and beam characteristics.

Furthermore, we extend our method towards spheroidal cluster geometries as in Section 6.4. We apply this reconstruction algorithm to the cluster based on an N-body/hydrodynamical simulation, discussed in Section 4.4.1. This time however, we have a realistic simulation of an observation with the Chandra X-ray Observatory from Meneghetti et al. (2010b) using the *X-ray MAp Simulator* (XMAS) (presented in Gardini et al., 2004; Rasia et al., 2008). It is realistic in that sense that it mimics all uncertainties of the Chandra satellite.

The contents of this chapter have been published in Konrad, Majer, Meyer et al. (2013); Majer, Meyer, Konrad et al. (2013); Tchernin, Majer, Meyer et al. (2013).

7.1 Simulation of Chandra observations

We choose a spherically symmetric cluster model with an NFW density profile, in detail explained in Section 3.1.2, and apply a noise model corresponding to observations carried out with Chandra.

If we assume the cluster to be in hydrostatic equilibrium and an ICM that follows a polytropic equation of state, we can use Eq. (3.35) and Eq. (3.37) to calculate the density and temperature profile of the cluster. To obtain a temperature profile which drops to zero at a large radius, we choose a cut-off

radius for the gravitational potential of $r_{\mathrm{cut}} = r_{200}$. The specific emissivity $j_X(\nu)$ due to bremsstrahlung is given by Eq. (3.43) in Section 3.2.3. The expectation value for the number of photons emitted in a detector in the energy interval $[E_0, E_1]$ per unit volume and time then reads

$$N_X = \int_{E_0(1+z_{\mathrm{cl}})}^{E_1(1+z_{\mathrm{cl}})} \frac{\mathrm{d}\,(h\nu)}{h} \frac{j_X(\nu)}{h\nu} \tag{7.1}$$

with the redshift z_{cl} of the cluster. In order to obtain an image comparable to observations, we simulate the CCD of Chandra as follows:

- We neglect the convolution of the image with the telescope beam: Each pixel is mapped to a unique solid-angle element. The physical area δA at the distance of the cluster spanned by one pixel is
$$\delta A = \delta\theta^2 \, D_{\mathrm{ang}}^2, \tag{7.2}$$
where D_{ang} is the angular diameter distance to the cluster and $\delta\theta$ the angular scale of the cluster mapped onto one pixel, assuming them to be perfectly quadratic.
- Any absorption of X-ray photons between the cluster and the telescope is neglected.
- The detector has a perfect quantum efficiency within a sharp energy interval. Given the photon counts of the cluster by Eq. (7.1), a pixel centred on the radial coordinate s is expected to collect
$$\delta N\,(s) = \delta A \int \mathrm{d}z \, N_X\left(\sqrt{s^2 + z^2}\right) \frac{A_{\mathrm{eff}}}{4\pi D_{\mathrm{lum}}^2(z_{\mathrm{cl}})} (1 + z_{\mathrm{cl}}) \tag{7.3}$$
photons per second. Note that the z-integration refers to a line-of-sight integration. D_{lum} is the luminosity distance to the cluster, and A_{eff} is the effective detector area. Since the above equation includes a conversion from photon energy to photon counts, only one factor of $(1 + z_{\mathrm{cl}})$ appears.
- The limited energy resolution of the telescope is imitated by choosing appropriate energy intervals in Eq. (7.1).

For the exact properties of the CCD we adopt the characteristics of the Chandra Advanced CCD Imaging Spectrometer (ACIS). The detection energy range of Chandra is $0.5 - 8\,\mathrm{keV}$. We arbitrarily choose $\left(E_{\mathrm{up}} - E_{\mathrm{low}}\right)/E_{\mathrm{res}} = 15$ energy intervals with the lower and upper energy boundary E_{low} and E_{up} and the energy resolution E_{res}. We can choose the intervals since our method is sensitive only to the total number of photons and no spectral information is needed. We calculate photon numbers to the pixels by drawing Poisson deviates with the appropriate expectation value δN for all 15 energy intervals. The mean energy is assigned to each photon and the sum of energies asigned to the corresponding pixel. We include statistical noise by adding a constant background such that approximately 20% (arbitrarily chosen) of the detected photons are due to background photons with the lowest considered energy of 0.5 keV (Hasinger, 1996). The pixel width is taken to be $0.5''$ and the exposure time is set to 3000 s.

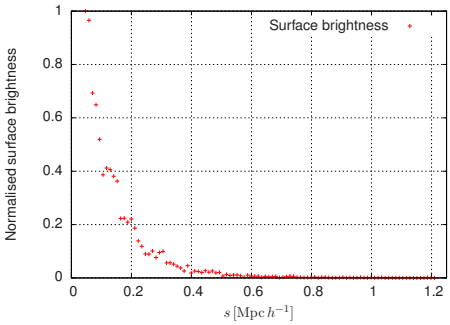

Figure 7.1: Azimuthally averaged and normalised surface brightness profile of a simulated galaxy cluster with a mass of $5 \times 10^{14}\,\mathrm{M}_\odot\,h^{-1}$ and a redshift of 0.2.

In this way we obtain an X-ray surface brightness, which is then azimuthally averaged around the cluster's centre, taken at the emission peak, and binned. This profile is used as an estimate for the X-ray surface brightness profile and supplied to the Richardson-Lucy deprojection algorithm in the next

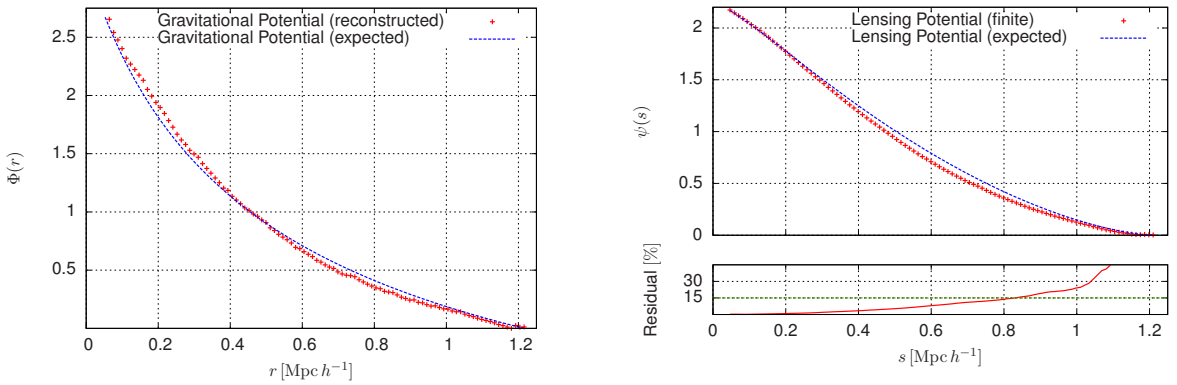

(a) (b)

Figure 7.2: (a) Reconstructed and normalised gravitational potential of a simulated galaxy cluster with a mass of $5 \times 10^{14}\,\mathrm{M}_\odot\,h^{-1}$ and a redshift of 0.2. The potential was reconstructed assuming $\alpha = 1.1$ and $L_{\mathrm{max}} = 0.21\,\mathrm{Mpc}\,h^{-1}$. (b) Upper panel: Reconstructed lensing potential ψ (red) and real lensing potential ψ_{true} (blue) for this simulated cluster. Lower panel: rms deviation of ψ from ψ_{true} calculated from 100 different realisations of the modelled galaxy cluster. The green line represents the 15% threshold.

section. Figure 7.1 shows the normalised surface brightness profile of a simulated Chandra image for one realisation of a galaxy cluster with a mass of $5 \times 10^{14}\,\mathrm{M}_\odot\,h^{-1}$ and a redshift of 0.2. With these characteristics and the cosmology we already used in Section 6.2 and a concentration of $c = 5$, this cluster has a scale radius of approximately $r_{\mathrm{s}} = 0.25\,\mathrm{Mpc}\,h^{-1}$.

7.2 Application to mock data with spherical symmetry

In the above section we explained how we generate our mock simulation using the basic characteristics of Chandra and a NFW density profile for the cluster. In this way we obtain a data set to which we can apply our reconstruction method. In parallel to Chapter 6, we infer the lensing potential of the galaxy cluster by applying Eq. (3.47) and using the method explained in Section 3.2.3.

The reconstructed and normalised gravitational potential is shown in Fig. 7.2(a) together with the true potential inferred from the simulation. Despite the statistical fluctuations of the surface brightness profile supplied to the algorithm, the contribution of the background noise exceeds the real surface brightness profile at large radii (i.e. $s \gtrsim 0.8\,\mathrm{Mpc}\,h^{-1}$) which can easily be corrected by estimating and subtracting the background prior to reconstruction. The reconstructed lensing potential follows the true potential very well up to a radius of $s \approx 0.8\,\mathrm{Mpc}\,h^{-1}$ as seen in Fig. 7.2(b) and referring to the 15% level. The reconstruction is carried out with $\alpha = 1.1$ and $L_{\mathrm{max}} = 0.21\,\mathrm{Mpc}\,h^{-1}$. Both values are found with the optimisation procedure from Section 5.5. The value for α is higher compared to the one found in Section 6, i.e. α was of the order 0.3, which reflects the different noise characteristics of the X-ray emission: In comparison to the thermal SZ effect we now have fluctuations on small scales which requires more regularisation.

As in Chapter 6 we calculate the uncertainty of our reconstructed lensing potentials based on different realisations of the background noise. We create 100 samples of the background noise and reconstruct each data set separately. For each result of the reconstruction the mean squared deviation from the true potential is calculated and then averaged over the number of bootstraps, which gives the rms deviation from Eq. (6.8). The rms is shown in the lower panel of Fig. 7.2(b). We choose the parameters α and L_{max} for each data set separately by applying the method explained in Section 5.5. However, we restrict L_{max} to the range $0.06 \leq L_{\mathrm{max}} \leq 0.25\,\mathrm{Mpc}\,h^{-1}$. This range is guided by the points mentioned in Section 5.5 and further reflects the bin size and roughly 20% of the total field size. The relative rms from the true lensing potential remains below 15% for radii smaller than $s \approx 0.8\,\mathrm{Mpc}\,h^{-1}$.

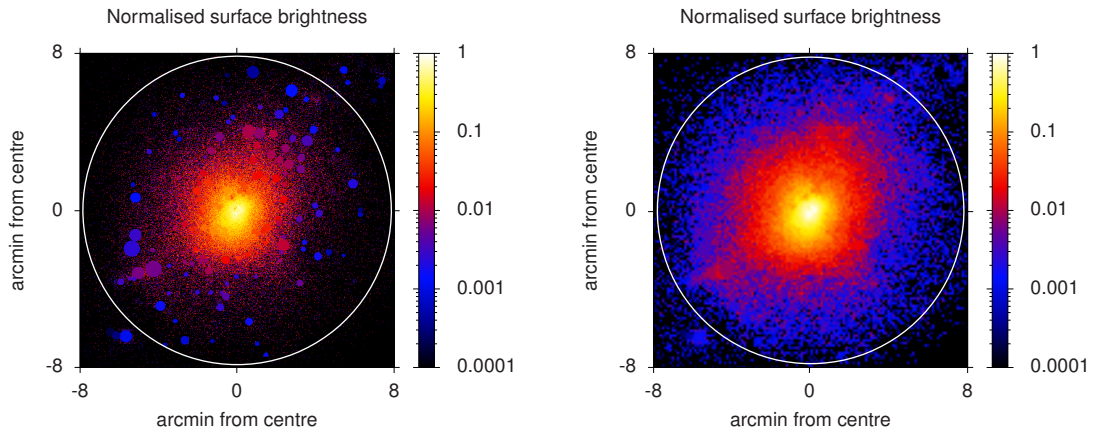

(a) (b)

Figure 7.3: (a) Masked and normalised surface brightness of the g1 cluster in the xy-plane. The masked areas are filled with the mean value of their neighbouring pixels. The FOV has an angular diameter of 16′. with a resolution of 512×512 pixels. (b) Corresponding image to (a) but on a lower resolution of 128×128 pixels. In both figures the white circle indicates the virial radius.

7.3 Application to a hydrodynamical simulation assuming spheroidal symmetry

We now use again the g1 cluster from the hydrodynamical simulation from Section 4.4.1. For this simulation we have the same X-ray observation as in Meneghetti et al. (2010b) (see there and the references therein for further details). The images were created with a constant response over the whole detector using the properties of the ACIS-S3 CCD. The images have a field of view of 16′ side length which corresponds to 2.97 Mpc h^{-1} in the given cosmology and a redshift of $z = 0.297$. The exposure time is 500 ks using the soft band $[0.7 - 2]$ keV. In this image regions with dense cold blobs, which are related to the cores of structures that merged previously (Meneghetti et al., 2010b) with this cluster, are masked. The masks are filled with the mean value of the pixels which surround the mask. The resulting image of the g1 cluster is shown in Fig. 7.3(b). For our spheroidal deprojection method, which is computationally rather expensive (the order of several hours for 128×128 pixels), we may only reconstruct an image of up to 128×128 pixels rather than the full resolution of 512×512 from Meneghetti et al. (2010b). We therefore lower the resolution of Fig. 7.3(a) to the above size, shown in Fig. 7.3(b), which corresponds to an angular resolution of 7.5″.

This image is supplied to our deprojection algorithm explained in Section 5.4. The inclination angle ι is inferred from Meneghetti et al. (2010b) to be $\iota \approx 84°$. We determine the strength of regularisation as explained in Section 5.5, but we set the value for to $L_{\max} = 1.2'$, due to the computational time issue mentioned above. Like in Section 6.4 we choose a quadratically increasing smoothing scale as it fits better to the S/N profile. In this way we constrain the best-fitting strength of regularisation to be $\alpha = 0.1$. This value is again rather small compared to the one needed in Section 7.2 due to the fact that the observation has such a high S/N because of the long integration time. With the estimated adiabatic index of $\gamma = 1.22 \pm 0.02$ from the data presented in Meneghetti et al. (2010b) we can further set the exponent from Eq. (3.47) to $\hat{\eta} = 9.55$.

Given the above parameters, we can carry out the reconstruction: First we apply our Richardson-Lucy deprojection for spheroidal cluster geometry to infer the three-dimensional emissivity. Then, we use Eq. (3.47) and the exponent $\hat{\eta}$ to proceed to the three-dimensional gravitational potential. This is finally projected along the line-of-sight to yield a scaled estimate for the lensing potential. Like in Section 6 we can compare our result to the lensing potential inferred from the surface-mass density

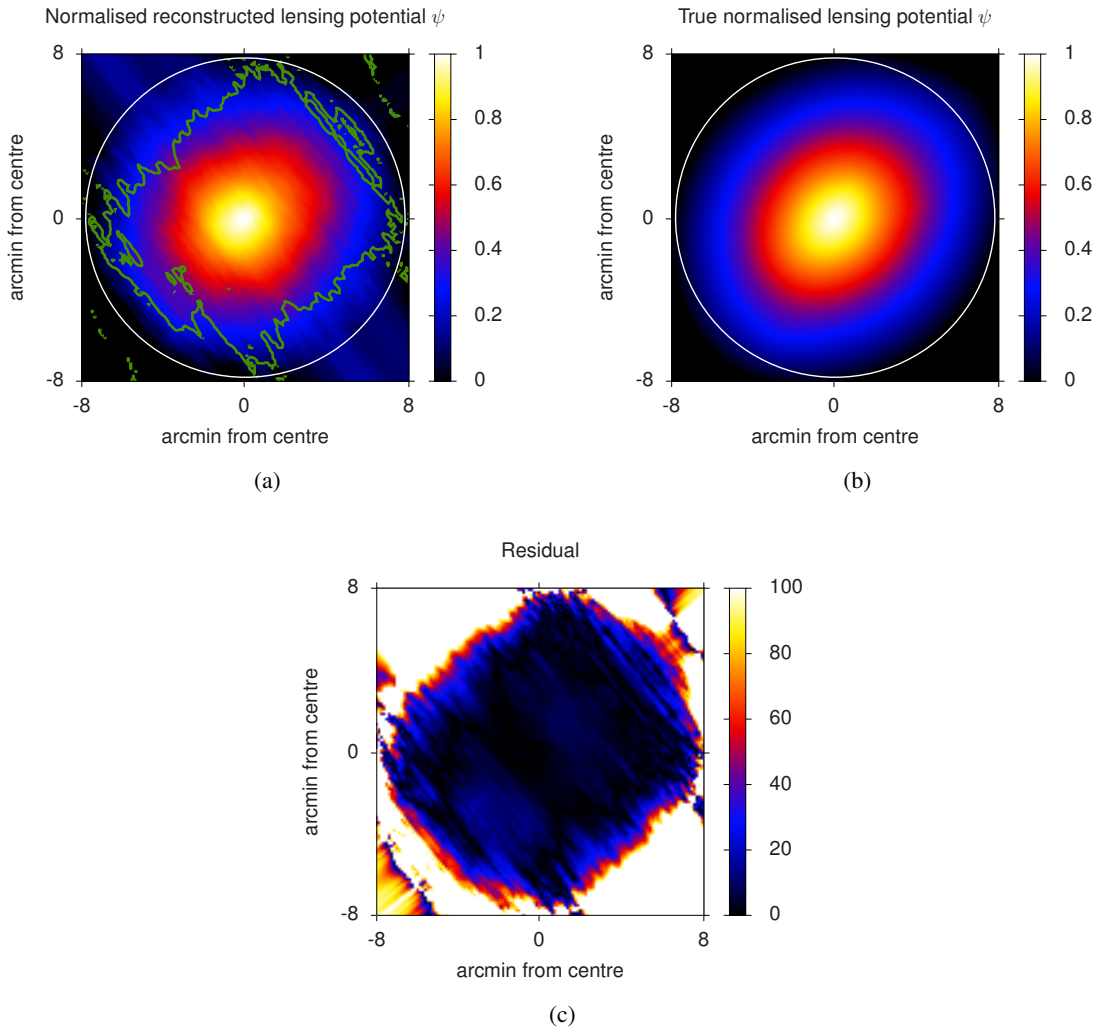

Figure 7.4: (a) Reconstructed lensing potential from the specific intensity change shown in Fig. 6.6. The white circle corresponds to the virial radius and the green contour depicts a 15% deviation from the real underlying lensing potential. (b) True lensing potential as obtained from the hydrodynamical simulation together with the virial radius (white line). (c) Modulus of the relative residual from (a) and (b).

map. Both the reconstruction and the real lensing potential are shown in Fig. 7.4. Again we see the elongated shape of the real lensing potential in Fig. 7.4(b), but this time the virial radius (indicated by the white circle) covers the whole FOV as the angular diameter of the image is now only 16′ across which corresponds to the FOV of Chandra. In Fig. 7.4(a) we show our reconstructed lensing potential together with the virial radius and a 15%-contour (green line) derived from the relative residual in Fig. 7.4(c). By comparing Fig. 7.4(a) with (b) we can see that we reproduce the elliptical shape of the lensing potential reliably. In the residual from Fig. 7.4(c) we further see that the reconstruction is below the 15% level for $s \approx 0.8 \times r_{\mathrm{vir}}$. Like in Section 6.4 we have larger deviations from the true lensing potential for the boundaries of our FOV, again due to the principle of our deprojection method as we are limited to the incircle.

Given these results we can say that our reconstruction algorithm based on a Richardson-Lucy deprojection method works reliably also for a spheroidal cluster geometry. We can further state that the assumption of hydrostatic equilibrium and a polytropic equation of state does not contradict the measurement in the case of this simulated cluster. However, in comparison to the one-dimensional reconstruction assuming spherical symmetry from Section 7.3 we need a stronger signal as we do not

increase the S/N of the supplied data by a further averaging process. This issue was already discussed in Section 5.8. Furthermore, the knowledge of the inclination angle ι is crucial for the reconstruction. For this particular input parameter our reconstruction has to rely on other techniques to provide this angle.

7.4 Summary and conclusion

In this Chapter we studied how our deprojection method performs with realistically simulated observations of X-ray emission due to thermal bremsstrahlung. In Chapter 5 we outlined our non-parametric reconstruction method for the projected gravitational potential of galaxy clusters in general. In Chapter 6 we applied this algorithm to observations of the thermal SZ effect. Like in Chapter 6, we first assumed hydrostatic equilibrium and spherical symmetry to create a mock data set of a galaxy cluster with an NFW density profile. To this mock data set, which included background noise as well, we applied our reconstruction method showing how well the algorithm performs under realistic conditions. Furthermore, we determined the rms deviation from 100 noise realisations which gave us an estimate for the errors of our cluster reconstruction algorithm. It was calculated to be at most 15% for $s \approx 0.8 \times r_{\mathrm{vir}}$.

Even though our simulated galaxy cluster had a rather smooth surface brightness profile, this technique can be applied without restrictions to less well-behaved observational data, e.g. strongly peaked emission in the cluster centre due to cooling effects. In such cases, the centre could be masked and then passed to the Richardson-Lucy algorithm. The results would still be reliable thanks to the local character of the deprojection scheme.

We applied the spheroidal cluster deprojection method explained in Section 5.4 to a cluster from the N-body/hydro-dynamical simulation from Section 4.4.1. For this simulation we used an imitated Chandra observation from Meneghetti et al. (2010b) using the XMAS code (see Gardini et al., 2004; Rasia et al., 2008). We re-binned the image to obtain a reasonable computational time for our reconstruction method. We were able to reconstruct the lensing potential up to a radius of roughly $0.8 \times r_{\mathrm{vir}}$ with a relative residual from the true lensing potential of less than 15%.

However, we want to summarise the major differences between the data sets used in this section and the ones from Chapter 6 for the thermal SZ effect:

(1) The only difference in our scheme regarding the physical processes – emission versus inverse Compton scattering – is the exponent $\hat{\eta}$ which corresponds to η for the thermal SZ effect in Eq. (3.41) and Eq. (3.47), which is related to the adiabatic index γ.

(2) The used telescope is different and thus has different characteristics, most importantly a different beam size and shape.

(3) The signal is a discrete set of detected photons, whereas for the thermal SZ effect the signal was a continuous distortion of the CMB.

(4) The noise of the X-ray emission is shot-noise, thus Poissonian. The noise in thermal SZ measurements continuous due to the specific intensity change of the CMB.

The findings of Chapter 6 and 7 clearly show that our reconstruction method is capable to recover the lensing potential of galaxy clusters both for the thermal SZ effect and for the X-ray emission of the ICM. Even though we assume hydrostatic equilibrium and a polytropic equation of state, we obtain reasonable results for a massive galaxy cluster which does not obey these assumptions per se. These methods add a further term to the χ^2-function of the mass reconstruction code *SaWLens* explained in Section 4.1.

Chapter 8

8 Application to RXJ1347-1145

In Chapter 6 we applied our reconstruction method to a spherically symmetric galaxy cluster and to a non-spherically symmetric galaxy cluster from a hydrodynamical simulation using their thermal SZ signals. Both applications showed promising results. In this Chapter we utilise our reconstruction method to infer the lensing potential of the massive galaxy cluster *RXJ1347-1145* (hereafter RXJ1347). The observation was made with *Bolocam* and provided by Sayers et al. (2013). This cluster is one of the most luminous ones so far detected in the X-ray band. For this cluster we also have a lensing-based reconstruction of the mass distribution at hand (Meneghetti et al., 2014), as part of the CLASH sample, to directly compare our results with.

First we apply the spherical reconstruction method with the deprojection from Section 5.3 and then the spheroidal scheme from Section 5.4.

8.1 RXJ1347

The massive galaxy cluster RXJ1347 is one of the most luminous clusters in the X-ray band with a X-ray luminosity of 6.0×10^{45} erg s^{-1} in the range of $2 - 10$ keV and was first discovered within the ROSAT all-sky survey (Voges et al., 1999). After that numerous other observations were carried out, e.g. with Chandra (Allen et al., 2002, 2008) and with XMM Newton (Gitti & Schindler, 2004; Snowden et al., 2008). Optical observations revealed two giant elliptical galaxies, coinciding with the peaks of the X-ray emission (Cohen & Kneib, 2002; Bradač et al., 2008), which suggests that the cluster has undergone a major merger (Gitti et al., 2007). Also a radio mini halo was reported (Gitti et al., 2007). Together with lensing analyses (Bradač et al., 2008) and SZ observations (Carlstrom et al., 2002; Bonamente et al., 2008; Mason et al., 2010; Plagge et al., 2013) this cluster is best suited for a multi-wavelength approach. The mass of RXJ1347 within the virial radius was inferrerd, using the assumption of spherical symmetry and hydrostatic equilibrium, by Schmidt & Allen (2007) to be $M \approx 2.3 \times 10^{15}\,\mathrm{M}_\odot\,h^{-1}$ at a redshift of $z = 0.451$. They calculated a concentration of $c = 4.791$ with a scale radius $r_\mathrm{s} = 0.54\,\mathrm{Mpc}$ for the best-fitting NFW profile. According to Medezinski et al. (2010) the virial radius is $r_\mathrm{vir} = 1.6\,\mathrm{Mpc}\,h^{-1}$. By a combination of the thermal SZ effect and X-ray emission Sereno et al. (2006) inferred that the cluster may have a prolate or oblate shape. For the prolate case, which we will assume here, Sereno et al. (2006) find an estimated inclination angle $\iota = 35° \pm 12°$. These findings are confirmed by Chakrabarty et al. (2008) who determine RXJ1347 to be a triaxial and prolate cluster with $\iota < 47°$.

The SZ observation was kindly provided by Sayers et al. (2013) and obtained with Bolocam (Glenn et al., 1998). It is part of the *Bolocam X-Ray/SZ Galaxy Cluster Sample* (Sayers et al., 2013). The observation covers a FOV of $10' \times 10'$ and the virial radius of this cluster has an extent of roughly $6.6'$. The cluster was observed for 15.5 hours with the band centre at 140 GHz, achieving a maximal signal-to-noise ratio of $S/N = 36.6$. The data are shown in Fig. 8.1.

A potential problem occurs by applying our method to Bolocam data: The beam of Bolocam has roughly a size of 58″ (FWHM). In such a case the assumption of a narrow beam compared to the resolution, like we stated in Section 3.2.2, is not applicable in a strict sense. By applying our method we would obtain the beam-convolved effective pressure, which then is transformed to the gravitational potential. One would expect the result to be flatter due to this convolution. However, for simplicity we assume the beam to be narrow.

One last piece of information is still missing before we can apply our reconstruction method: It is the polytropic index γ, which is needed to calculate the exponent $\eta = 1/(\gamma - 1)$ from Eq. (3.41). Bonamente et al. (2012) used thermal SZ observations with the *Sunyaev-Zel'dovich Array* as part of the *Combined Array for Research in Millimeter-wave Astronomy* (CARMA) together with Chandra X-ray observations to estimate a mean pressure profile for a large number of relaxed clusters – one of them is RXJ1347. The pressure profile is computed using the model of Bulbul et al. (2010). This analytic formula is based on spherical symmetry and a polytropic gas stratification with a single index linking the gas temperature T to the electron density n_e with the polytropic index n,

$$n_e \propto T^n \,. \tag{8.1}$$

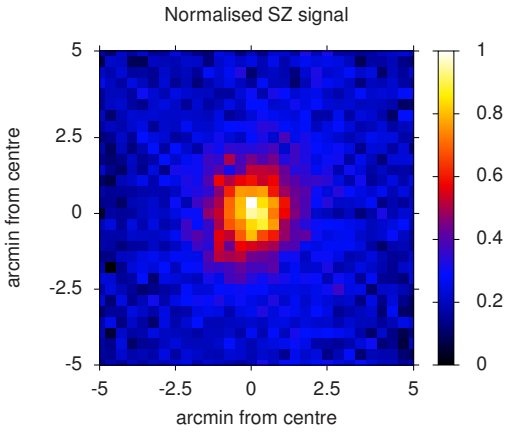

Figure 8.1: Thermal SZ signal of RXJ1347 at 140 GHz as obtained with Bolocam (Sayers et al., 2013). The FOV has a size of 10′ × 10′ with an exposure time of 15.5 hours and maximal $S/N = 36.6$.

Bulbul et al. (2010) use a generalised NFW profile, see Section 3.1.2, for the density of the halo, which yields for the gas pressure

$$P_e(r) = P_{e0}\left[\frac{1}{\beta - 2}\,\frac{(1 + r/r_s)^{\beta-2} - 1}{r/r_s(1 + r/r_s)^{\beta-2}}\right]^{n+1} , \tag{8.2}$$

with the four fitting parameters P_{e0}, n, r_s, and β.

However, Bonamente et al. (2012) reduce the density profile to the original NFW profile (i.e. $\beta = 2$) and use $n = 3.5$, derived as the median of a fit. From Eqs. (3.35) and (3.37) we obtain $\gamma = 1.28$.

8.2 Reconstruction assuming spherical symmetry

The data from Fig. 8.1 are binned and averaged in annuli to obtain a radial profile, see Fig. 8.2(a). Given the scatter in each bin we apply the same bootstrapping method as in Section 5.6 to create further data sets by re-sampling the input data with a Gaussian distribution. With this method we obtain 100 realisations of the signal, which are all reconstructed with our algorithm assuming spherical symmetry. The strength of regularisation α and the scale of the floating default kernel L_{max} are calculated for each realisation individually by applying the optimal fit criterion from Section 5.5. For the original data set we report the values $\alpha = 0.9$ and $L_{max} = 1.3'$. From all 100 reconstructions we calculate the standard deviation and assign this number to the original reconstruction as the error.

From Meneghetti et al. (2014) we have the convergence map reconstructed using the *SaWLens* code (see Section 4.1) with strong and weak-lensing measurements. This convergence map is used to infer the lensing potential on the same angular scale as the Bolocam observation by solving Poisson's equation numerically. The comparison of our reconstruction using thermal SZ data (blue) and the result using gravitational lensing (red) is shown in the upper panel of Fig. 8.2(b). Our reconstruction

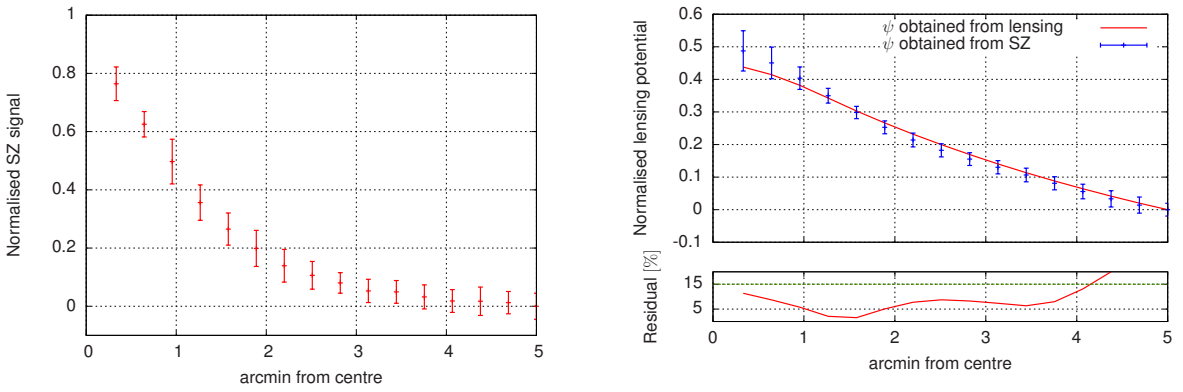

(a) (b)

Figure 8.2: (a) Averaged and normalised thermal SZ signal obtained from Fig. 8.1. The errors correspond to the standard deviation in each annulus. (b) Upper panel: Normalised reconstruction of the lensing potential from the profile in (a) together with the lensing potential from Meneghetti et al. (2014). Lower panel: Modulus of the relative residual of both curves in the upper panel. The green line marks a 15% threshold.

is fully compatible within its uncertainties to the azimuthally averaged profile of the reconstruction using gravitational lensing. However, the assigned errors are most likely overestimating the real uncertainties: The averaged bins contain not only information on the noise in each annulus but also a bias, which is introduced by the non-sphericity of the cluster, as RXJ1347 is most likely not spherically symmetric (Sereno et al., 2006; Chakrabarty et al., 2008). This further implies that the spheroidal reconstruction, which we apply in the next section, should yield more realistic results.

The lower panel of Fig. 8.2(b) shows the modulus of the relative residual. For the whole angular range out to $s = 4'$ the deviation is below 15%.

8.3 Reconstruction assuming spheroidal symmetry

As in Section 6 we apply our reconstruction algorithm for spheroidal geometry to the Bolocam data of RXJ1347. But before we go into a detailed analysis of the reconstruction, we explain how an error estimatimation is obtained for this reconstruction.

8.3.1 Error estimation

We shortly discuss on the errors we expect for our spheroidal reconstruction method as the bootstrap method used in the preceding section is not applicable in this case due to the long computing time of the code.

Denoting the observational data with $g(s)$ and the deprojected quantity with $f(r)$ corresponding to Section 5, we can make the following considerations: Starting with the general iteration scheme from Eq. (5.7) and assuming the observational noise of Bolocam to be constant over the FOV, we write

$$\begin{aligned}\tilde{f}_{i+1}(r) &= \tilde{f}_i(r) \int \mathrm{d}s \, \frac{g(s)}{\tilde{g}_i(s)} \, K(s|r) \\ &= \tilde{f}_i(r) \int \mathrm{d}s \, \frac{\bar{g}(s) + \delta g}{\tilde{g}_i(s)} \, K(s|r) \\ &= \tilde{f}_i(r) \left(\int \mathrm{d}s \, \frac{\bar{g}(s)}{\tilde{g}_i(s)} \, K(s|r) + \frac{\delta g}{\bar{g}(s)} \int \mathrm{d}s \, \frac{\bar{g}(s)}{\tilde{g}_i(s)} \, K(s|r) \right), \end{aligned} \tag{8.3}$$

assuming that the data splits into a noise-free part $\bar{g}(s)$ and a noise contribution δg such that $g(s) = \bar{g}(s) + \delta g$. We further assume for simplicity – and as it yields reasonable results – the relative deviation $\delta g/\bar{g}(s)$ to be independent of s. The integrals in Eq. (8.3) approaches unity as our algorithm converges to the mean solution $\bar{g}$, allowing us to write

$$\begin{aligned}\tilde{f}_{i+1}(r) &= \tilde{f}_i(r)\left(\int \mathrm{d}s\, \frac{\bar{g}(s)}{\tilde{g}_i(s)}\, K(s|r) + \frac{\delta g}{\bar{g}(s)}\right) \\ &= \tilde{f}_i(r)\left(1 + \frac{\delta g}{\bar{g}(s)}\right) \\ &\equiv \bar{\tilde{f}}_{i+1}(r) + \delta f_{i+1} \end{aligned} \tag{8.4}$$

and to identify the error on the deprojected quantity $\tilde{f}_{i+1}(r)$. Dropping the indices, thus assuming our algorithm has converged, the relative error of $g(s)$ and $f(r)$ should be equal,

$$\frac{\delta f}{f(r)} = \frac{\delta g}{g(s)}\,. \tag{8.5}$$

Our algorithm then proceeds to the gravitational potential $\varphi(r)$ with the exponent η from Eq. (3.41),

$$\begin{aligned} f(r) + \delta f &= [\varphi(r) + \delta\varphi]^\eta \\ &= \varphi^\eta(r)\left[1 + \frac{\delta\varphi}{\varphi(r)}\right]^\eta \\ &\approx \varphi^\eta(r)\left[1 + \eta\,\frac{\delta\varphi}{\varphi(r)}\right]. \end{aligned} \tag{8.6}$$

The last approximation holds if we neglect higher order terms in $\delta\varphi$. Again, we have a proportionality between the relative deviations,

$$\frac{\delta f}{f(r)} = \eta\,\frac{\delta\varphi}{\varphi(r)}\,. \tag{8.7}$$

The final step in our reconstruction scheme is the line-of-sight projection of the gravitational potential to infer the lensing potential $\psi(s)$. We write

$$\begin{aligned}\psi(s) + \delta\psi &= \int \mathrm{d}r\, K(s|r)\, [\varphi(r) + \delta\varphi] \\ &= \int \mathrm{d}r\, K(s|r)\, \varphi(r) + \int \mathrm{d}r\, K(s|r)\, \delta\varphi\,, \end{aligned} \tag{8.8}$$

from which we can conclude that

$$\begin{aligned}\delta\psi &= \int \mathrm{d}r\, K(s|r)\, \delta\varphi \\ &= \frac{1}{\eta}\int \mathrm{d}r\, K(s|r)\, \varphi(r)\, \frac{\delta f}{f(r)} \\ &= \frac{1}{\eta}\,\frac{\delta g}{g(s)}\int \mathrm{d}r\, K(s|r)\, \varphi(r) \\ &= \frac{1}{\eta}\,\frac{\delta g}{g(s)}\,\psi(s)\,. \end{aligned} \tag{8.9}$$

The relative error $\delta\psi/\psi(s)$ is thus the relative error of the data $g(s)$ divided by the exponent η. This is in agreement with the statement we made in Sections 3.2.2 and 3.2.3: As η is a large number, fluctuations in the data will be smoothed considerably once the algorithm proceeds to the lensing potential.

From Sayers et al. (2013) we have received 1000 independent noise realisations of the Bolocam field considered here (see Sayers et al., 2011, for further details). With these we can estimate the relative errors of the data and take the average over the entire FOV. With this constant, we apply Eq. (8.9) to infer the errors of our reconstructed lensing potential.

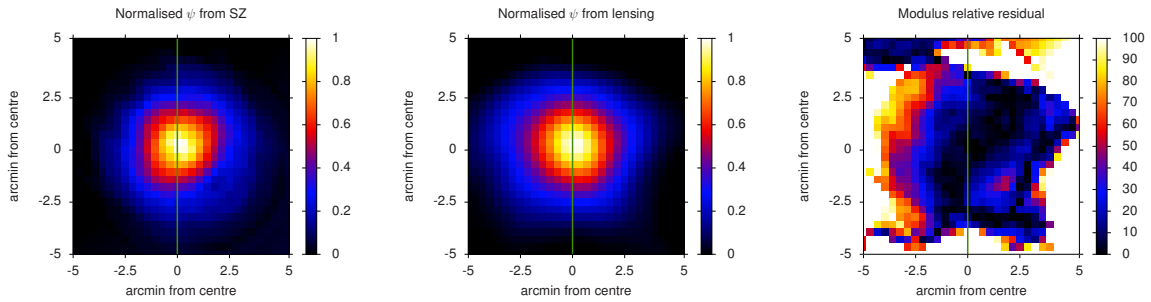

(a) (b) (c)

Figure 8.3: (a) Reconstructed lensing potential ψ of RXJ1347 using the signal of thermal SZ effect shown in Fig. 8.1. (b) Lensing potential ψ reconstructed with weak- and strong-lensing information using *SaWLens* (Meneghetti et al., 2014). (c) Modulus of the relative residual of (a) from (b). In all three panels the green line indicates the section of Fig. 8.4.

8.3.2 Reconstruction

We choose a quadratically increasing smoothing scale with $L_{\max} = 1'$ as we did in Sections 6.4 and 7.3 and the best-fitting strength of regularisation is $\alpha = 0.315$ (see Section 5.5 for details). The convergence map from Meneghetti et al. (2014) was transformed to the lensing potential by solving Poisson's equation by means of a fast Fourier method and zero-padding (adding zeros around the image before Fourier transformation) to account for the periodic boundary condition of this method. Once again exploiting our freedom to choose the normalisation and the background level, we normalise both lensing potentials. We show our reconstruction in Fig. 8.3(a), the lensing potential obtained from the lensing reconstruction in Fig. 8.3(b), and the modulus of the residual in Fig. 8.3(c). In all three figures the green line indicates the section of Fig. 8.4, which we will discuss below. Considering Fig. 8.3 we conclude the following:

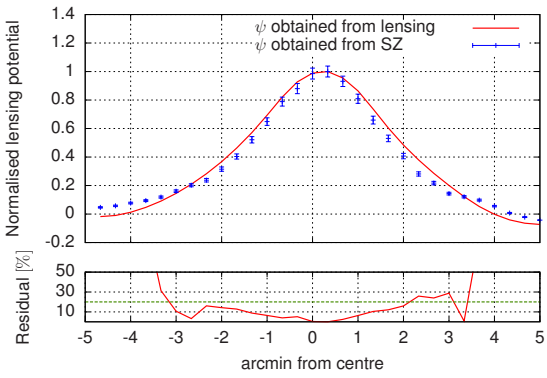

Figure 8.4: Upper panel: Profile of the reconstructed and normalised lensing potential. The position was indicated by a green line in Fig. 8.3. Blue marks our reconstruction with the errors obtained from Eq. (8.9). Red indicates the lensing potential reconstructed with weak- and strong-lensing constraints. Lower panel: Modulus of the relative residual inferred from the upper panel. The green dotted line marks a 20% level.

- The overall agreement of both reconstructions is very satisfactory. Even for areas with a low S/N, i.e. for radii $|s| \gtrsim 3'$, we achieve good results.
- Due to the assumption of spheroidal geometry we have to find a symmetry axis in the lensing potential which is not visible in this extent in the reconstruction using lensing constraints.
- The lensing potential in Fig. 8.3(b) falls off more slowly in the outskirts of the cluster.
- The modulus of the residual in Fig. 8.3(c) shows deviations within 20% for the central region of the cluster. The deviations in the outer parts of the cluster increase steeply towards the outskirts of the cluster.
- The deviations in the corners of the FOV are mainly due to the rotation in the plane of the sky as explained in Section 6.

In Fig. 8.3 we indicate with a green line a specific section through our reconstruction, for which we show the corresponding profile in Fig. 8.4. A section through the cluster's centre seems reasonable due to the highest S/N there. In this view we can further include the errors obtained with Eq. (8.9). The shape of the reconstructed lensing potential follows the one of the lensing potential obtained with *SaWLens* for an angular radius of $-3' \lesssim s \lesssim 3'$ and the obtained values are within one standard deviation. The modulus of the residual in the lower panel of Fig. 8.4 is below 20% for the same region. As seen in the complete view of Fig. 8.3(c) the outskirts of the cluster are over-estimated.

8.4 Summary and conclusion

We applied our reconstruction method based on both spherical and spheroidal geometry to the massive galaxy cluster RXJ1347. We used an observation of the thermal SZ effect obtained with Bolocam (Sayers et al., 2013). Our results were compared to a strong- and weak-lensing reconstruction by Meneghetti et al. (2014) using the *SaWLens* code. The adiabatic index was taken as $\gamma = 1.28$ as inferred using the data presented in Bonamente et al. (2012) who assumed the pressure profile of Bulbul et al. (2010).

The spherical reconstruction showed a very good agreement between the different reconstruction methods. Errors were assigned to our reconstruction by using a bootstrapping method. However, the inferred errors probably overestimate the real uncertainties due to the fact that we azimuthally average over the signal fluctuations and over the obvious elliptical shape of the cluster by assuming spherical symmetry. But the modulus of the relative residual from the lensing reconstruction was below 15% for a radius of $s \lesssim 4'$.

The spheroidal reconstruction algorithm was applied directly to the Bolocam data assuming an inclination angle of $\iota = 35°$ (Sereno et al., 2006). The S/N, peaking in the centre at $S/N = 36.6$, dropped towards the corners of the FOV allowing us only to reliably reconstruct an angular region of $-3' \lesssim s \lesssim 3'$. But the overall shape of the inferred lensing potential corresponded to the reconstruction using *SaWLens* accept for the assumed symmetry axis. We further explained how measurement uncertainties propagate through our algorithm to first order. This information was used to calculate a profile of both reconstructions along the y-axis of the FOV's centre with the corresponding errors. It revealed a very good agreement in the cluster centre, where our reconstruction agreed within one sigma with the one obtained from lensing information.

But by applying our reconstruction method to RXJ1347, we also saw the current limits of this method: The lensing potential obtained from weak- and strong-lensing constraints does not obey any a-priori symmetry in the plane of the sky. Thus our algorithm was not capable of recovering features prominent in the lensing reconstruction which deviated from the assumed spheroidal geometry. Another source of uncertainty was introduced with the polytropic index and the inclination angle as both have to be inferred with other techniques and both are needed a-priori for the reconstruction. However, once these parameters are known for a specific cluster and the S/N is large enough, our reconstruction method yields reliable and promising results for future cluster analyses.

As explained above, we have problems to infer the lensing potential in the outer parts of the FOV due to the rotation in the plane of the sky. The reliability of our method is further reduced in these regions because of the lower S/N there. But once our reconstructed lensing potential is supplied to the *SaWLens* code by an appropriate χ^2-function, these parts could be excluded. Our reconstructed lensing potential from thermal SZ measurements then serves as a further and independent constraint on the convergence.

9 Chapter 9
Conclusion and outlook

In this work we presented three different ways to infer the two-dimensional line-of-sight projection of the gravitational potential – which is proportional to the lensing potential – of massive galaxy clusters. This included observations of gravitational lensing, of the thermal Sunyaev-Zel'dovich effect and finally of the X-ray emission due to thermal bremsstrahlung. All three observables can be brought together on the common ground of the lensing potential with the overall effort to extend common lensing reconstruction methods based on gravitational lensing. Such a multi-wavelength approach combines all available cluster observables in one consistent joint reconstruction, and well-tested strong- and weak-lensing reconstruction codes are expected produce more reliable results. As it is straightforward to proceed from the lensing potential to the convergence also estimates of cluster mass distributions will become more accurate, which will in turn tighten the bounds on the cosmological parameters Ω_m and σ_8. It is also important to answer the questions raised, for instance the claimed universality of the NFW density profile or the problem of over-concentrated halos, by numerical simulations and to understand how the discrepancies between simulations and observations arise.

Reconstructions using information from gravitational lensing are widely used to infer the mass distributions of galaxy clusters. This method relies on constraints from weak and strong lensing as both give an independent estimate for the lensing potential of the cluster. However, to know the uncertainties of such a reconstruction method is crucial if one wishes to assess their reliability and if one wants to constrain cosmological parameters from it. Conventional and computationally very expensive methods rely on a bootstrapping method where the input ellipticities get re-sampled to estimate the statistical errors. To avoid this time-consuming procedure, we derived an analytic error estimation for reconstructions using weak-lensing information. In doing this we followed the reconstruction method implemented in *SaWLens* (Merten, 2010). This novel expression does not need any data resampling but only uses quantities already calculated by the reconstruction code itself. We confirmed that our analytic method is able to calculate the occurring errors compatible to the ones obtained with the common bootstrapping approach.

However, for our ansatz to work reliably we were in the need to fix one specific parameter which has to be inferred somehow. But, if the lensing reconstruction code has fully converged and is independent of any starting assumption (i.e. a vanishing convergence), the missing parameter was shown to tend towards unity. With these findings, this work is a step towards a fully analytic error estimation for reconstruction codes which use weak-lensing information and further has shown some general considerations, which may be also be applicable to an analytic error estimation regarding strong-lensing constraints.

The used non-parametric reconstruction code *SaWLens* may be augmented with further terms by means of additional χ^2-contributions. In the aspect of exploiting this possibility by adding further terms to the objective function, we established a relation between the lensing potential and observations of both the thermal SZ effect and X-ray emission. This relation was based on the assumption of hydrostatic equilibrium and an ICM with a polytropic equation of state and further involved a de-

projection of the observables. This deprojection was carried out by means of the Richardson-Lucy deprojection algorithm to infer the three-dimensional structure of the relevant observable under given symmetry assumptions. We started with spherical symmetry from where we extended the method to spheroidal geometry, which is more suitable for real galaxy clusters.

An alternative deprojection method is given by the so-called onion peeling. We compared the performance of our method in spherical symmetry to this broadly used method. This was done with the massive galaxy cluster Abell 1689 to which the onion peeling was applied by Eckert et al. (2012) using the X-ray surface brightness obtained with ROSAT. A comparison of our reconstructed emissivity and the one from Eckert et al. (2013) revealed that both methods agreed within their errors. Reassured by these findings, we tested our complete reconstruction method to infer the lensing potential from the given observables. This was done in spherical and spheroidal symmetry, respectively. We carried out a series of tests to estimate the reliability of our reconstruction, for which we started with thermal SZ measurements of a mock galaxy cluster. A realistic observation was imitated using the specifications of the ALMA interferometer with an elaborated noise model. To account for deviations of the above assumptions, we further applied our method to a galaxy cluster from a realistic N-body/hydrodynamical simulation. This cluster was neither set to be in hydrostatic equilibrium nor was the included ICM forced to follow a polytropic relation. Additionally, it was triaxialy shaped. Despite these possible deviations from our assumptions, we were also able to reconstruct the radial profile of the lensing potential very accurately, as we did before with our mock galaxy cluster.

Another observable of galaxy clusters is the X-ray emission from thermal bremsstrahlung. This signal itself is different compared to the thermal SZ effect: X-ray emission is of statistical nature compared to the continuous signal of the thermal SZ effect. Further differences between the data sets exist in the telescope beams as well as in their noise properties. Even though the physical processes behind the X-ray emission and the thermal SZ effect are different, we could formulate a similar method to infer the lensing potential from this observable. We applied the spherical reconstruction method to the same mock galaxy cluster as before, but now observations were imitated with the properties of the Chandra satellite. Once again we found very promising results regarding the reconstructed lensing potential.

An oblate or prolate cluster shape is certainly a much better assumption for most observed galaxy clusters, and the presented spheroidal reconstruction method is clearly more adequate compared to the spherical deprojection in such a case. We therefore applied our spheroidal reconstruction method to the galaxy cluster mentioned above by assuming it to be observed with ALMA. We further used a realistic simulation from Rasia et al. (2006) imitating the Chandra telescope for this cluster. In the thermal SZ case as well as in the case of X-ray emission, we achieved comparable results in retrieving the lensing potential. The reconstructions for these – more realistic cases – correctly inferred the lensing potential for a large fraction of the virial radius. This application to both observables clearly states that our method works reliably for both observables, despite the different physics.

As a proof of our concept and due to the fact that so far our efforts were confined to situations where we exactly knew the lensing potential, we reconstructed an actual observation. We applied our reconstruction method to the galaxy cluster RXJ1347 for which we used data obtained with Bolocam which was kindly provided by Sayers et al. (2013). We applied both reconstruction methods – spherical and spheroidal – to the thermal SZ signal of this cluster to reconstruct the lensing potential and directly compare our results to the strong- and weak-lensing reconstruction of Meneghetti et al. (2014) as part of the CLASH sample.

The spherical reconstruction showed a good correspondence between both data sets, though the errors were overestimated due to the azimuthal average. This issue was resolved by applying the spheroidal deprojection method. In this case the reconstruction showed a promising agreement for the inner parts of the cluster where the S/N was high enough.

But this application to real data also showed the current limits of our approach: Besides the fact that we need an observation with a high S/N, we also need to know the inclination angle of the

cluster towards the line-of-sight. The latter issue is not straightforward to solve as estimates of this inclination angle are difficult to obtain and the errors usually quite large. Attempts from combined X-ray and thermal SZ observations have been made for example by Sereno et al. (2006). Moreover, for small inclination angles – this equals clusters which are nearly aligned with the line-of-sight – our deprojection method faces problems as the distinction between a spherical and a spheroidal cluster geometry vanishes. Current limits of the spatial resolution of thermal SZ observations further pose problems as we did not account for any convolution of the signal and the telescope's beam.

We also state here once more that we have to rely at least on spheroidal symmetry of the cluster and an ICM that is in hydrostatic equilibrium. We are further in the need of a polytropic equation of state for the ICM which obviously limits our reconstruction method to a certain class of clusters: relaxed clusters. Our method is certainly not applicable to merging clusters or clusters which are disturbed otherwise. Even though the strong- and weak-lensing reconstruction code would yield very good results on such a cluster, a combined χ^2-function which includes our reconstruction from thermal SZ effect or X-ray emission would bias the inferred mass distribution of the cluster.

However, all found results are reassuring and clearly state that our reconstruction method is capable to give better constraints to galaxy clusters for real observations once our assumptions for a specific cluster are justified. The findings of this work additionally mark the beginning of a novel multi-wavelength reconstruction method. It involves X-ray emission, the thermal SZ effect, galaxy kinematics (see Sarli et al., 2013) and lensing information on the common ground of the lensing potential. First promising attempts on this were made by Huber (2013), using a method based on the χ^2-minimisation of Merten (2010): In combining weak- and strong-lensing information with the results from our X-ray and thermal SZ reconstruction, Huber (2013) was capable to retrieve the lensing potential from a simulated galaxy cluster more accurately than using lensing information alone. This accuracy can even be improved by assigning different statistical weights to the X-ray and thermal SZ data and exploiting the S/N of the given observable. Additionally, the issue of the unknown inclination angle towards the line-of-sight might be resolvable to some degree: Puchwein (2007) reported that an implementation based on an additionally measured temperature profile of the cluster might be feasible. In this way the reprojected deprojection of the observable could be compared to the additional temperature profile and a best-fitting deprojection could be found in dependence of the inclination angle. Such an approach may also be included in our formalism.

Finally, the most important point to be carried out in the future is the application to further galaxy clusters using both – thermal SZ effect and X-ray emission – observables. Although we applied the deprojection method to Abell 1689 using ROSAT data, a full analysis including thermal SZ measurements and a full strong- and weak-lensing analysis is missing so far. Even more, an application of the spheroidal deprojection method is yet to be carried out for an X-ray observation.

As we worked out, ALMA certainly opens the night sky to a large number of galaxy clusters yet to be detected in the microwave band. However, even with the South Pole Telescope our analysis would be applicable if the S/N was high enough and the issue of beam-convolution was solved. Concerning the X-ray emission of clusters, a multitude of high-fidelity observations is already available, for example from Chandra.

We can therefore state that by combining the work presented here with the results from Sarli et al. (2013) on galaxy kinematics, Merten (2010) on gravitational lensing and certainly the efforts of Huber (2013), we are at the edge of completing a reconstruction scheme including all these different data sets. Due to the independent observables it will be capable of reaching an unprecedented accuracy in determining the mass distribution of galaxy clusters.

Bibliography

Allen, S. W., Rapetti, D. A., Schmidt, R. W., et al. (2008): *Improved constraints on dark energy from Chandra X-ray observations of the largest relaxed galaxy clusters*. MNRAS, **383**, 879. [link]

Allen, S. W., Schmidt, R. W., & Fabian, A. C. (2002): *Chandra observations of RX J1347.5-1145: the distribution of mass in the most X-ray-luminous galaxy cluster known*. MNRAS, **335**, 256. [link]

Allgood, B., Flores, R. A., Primack, J. R., et al. (2006): *The shape of dark matter haloes: dependence on mass, redshift, radius and formation*. MNRAS, **367**, 1781. [link]

Andersson, K. E. & Madejski, G. M. (2004): *Complex Structure of Galaxy Cluster A1689: Evidence for a Merger from X-Ray Data?* ApJ, **607**, 190. [link]

Angrick, C. (2011): *On the derivation of an X-ray temperature function without reference to mass and the prediction of weak-lensing number counts from the statistics of Gaussian random fields*. Ph.D. thesis, Heidelberg, Univ., Diss., 2011

Bartelmann, M. (2001): *Lensing Sunyaev-Zel'dovich clusters*. A&A, **370**, 754. [link]

Bartelmann, M. (2004): *Cosmology*. Lecture

Bartelmann, M. (2010): *TOPICAL REVIEW Gravitational lensing*. Classical and Quantum Gravity, **27** (23), 233001. [link]

Bartelmann, M., *Theoretical Astrophysics: An Introduction* (Wiley-VCH, 2013), 1 edition

Bartelmann, M., Huss, A., Colberg, J. M., et al. (1998): *Arc statistics with realistic cluster potentials. IV. Clusters in different cosmologies*. A&A, **330**, 1

Bartelmann, M., Narayan, R., Seitz, S., et al. (1996): *Maximum-likelihood Cluster Reconstruction*. ApJL, **464**, L115+

Bartelmann, M. & Schneider, P. (2001): *Weak gravitational lensing*. Phys. Rep., **340**, 291. [link]

Basu, K., Zhang, Y.-Y., Sommer, M. W., et al. (2010): *Non-parametric modeling of the intra-cluster gas using APEX-SZ bolometer imaging data*. A&A, **519**, A29. [link]

Beckwith, S. V. W., Stiavelli, M., Koekemoer, A. M., et al. (2006): *The Hubble Ultra Deep Field*. AJ, **132**, 1729. [link]

Binney, J. & Tremaine, S., *Galactic Dynamics (Princeton Series in Astrophysics)* (Princeton University Press, 1988)

Binney, J. J., Davies, R. L., & Illingworth, G. D. (1990): *Velocity mapping and models of the elliptical galaxies NGC 720, NGC 1052, and NGC 4697*. ApJ, **361**, 78. [link]

Birkinshaw, M. (1999): *The Sunyaev-Zel'dovich effect*. Phys. Rep., **310**, 97. [link]

Bonamente, M., Hasler, N., Bulbul, E., et al. (2012): *Comparison of pressure profiles of massive relaxed galaxy clusters using the Sunyaev-Zel'dovich and x-ray data*. New Journal of Physics, **14** (2), 025010. [link]

Bonamente, M., Joy, M., LaRoque, S. J., et al. (2008): *Scaling Relations from Sunyaev-Zel'dovich Effect and Chandra X-Ray Measurements of High-Redshift Galaxy Clusters*. ApJ, **675**, 106. [link]

Bond, J. R., Cole, S., Efstathiou, G., et al. (1991): *Excursion set mass functions for hierarchical Gaussian fluctuations*. ApJ, **379**, 440. [link]

Boylan-Kolchin, M., Springel, V., White, S. D. M., et al. (2009): *Resolving cosmic structure formation with the Millennium-II Simulation*. MNRAS, **398**, 1150. [link]

Bradač, M., *Strong and weak lensing united: the cluster mass distribution of the most X-ray luminous cluster RXJ1347-1145*. In R. Dettmar, U. Klein, & P. Salucci, eds., *Baryons in Dark Matter Halos* (2004)

Bradač, M., Erben, T., Schneider, P., et al. (2005): *Strong and weak lensing united*. A&A, **437**, 49. [link]

Bradač, M., Schrabback, T., Erben, T., et al. (2008): *Dark Matter and Baryons in the X-Ray Luminous Merging Galaxy Cluster RX J1347.5-1145*. ApJ, **681**, 187. [link]

Broadhurst, T., Umetsu, K., Medezinski, E., et al. (2008): *Comparison of Cluster Lensing Profiles with ΛCDM Predictions*. ApJ, **685**, L9. [link]

Bulbul, G. E., Hasler, N., Bonamente, M., et al. (2010): *An Analytic Model of the Physical Properties of Galaxy Clusters*. ApJ, **720**, 1038. [link]

Bullock, J. S., Kolatt, T. S., Sigad, Y., et al. (2001): *Profiles of dark haloes: evolution, scatter and environment*. MNRAS, **321**, 559. [link]

Cacciato, M., Bartelmann, M., Meneghetti, M., et al. (2006): *Combining weak and strong lensing in cluster potential reconstruction*. A&A, **458**, 349. [link]

Caldwell, R. R., Dave, R., & Steinhardt, P. J. (1998): *Cosmological Imprint of an Energy Component with General Equation of State*. Physical Review Letters, **80**, 1582. [link]

Carlstrom, J. E., Holder, G. P., & Reese, E. D. (2002): *Cosmology with the Sunyaev-Zel'dovich Effect*. ARA&A, **40**, 643. [link]

Chakrabarty, D., de Filippis, E., & Russell, H. (2008): *Cluster geometry and inclinations from deprojection uncertainties. Cluster geometry and inclination*. A&A, **487**, 75. [link]

Coe, D., Umetsu, K., Zitrin, A., et al. (2012): *CLASH: Precise New Constraints on the Mass Profile of the Galaxy Cluster A2261*. ApJ, **757**, 22. [link]

Coe, D., Zitrin, A., Carrasco, M., et al. (2013): *CLASH: Three Strongly Lensed Images of a Candidate z 11 Galaxy*. ApJ, **762**, 32. [link]

Cohen, J. G. & Kneib, J.-P. (2002): *Losing Weight: A Keck Spectroscopic Survey of the Massive Cluster of Galaxies RX J1347-1145*. ApJ, **573**, 524. [link]

Corless, V. L., King, L. J., & Clowe, D. (2009): *A new look at massive clusters: weak lensing constraints on the triaxial dark matter haloes of A1689, A1835 and A2204*. MNRAS, **393**, 1235. [link]

de Blok, W. J. G. (2010): *The Core-Cusp Problem*. Advances in Astronomy, **2010**, 789293. [link]

De Filippis, E., Sereno, M., Bautz, M. W., et al. (2005): *Measuring the Three-dimensional Structure of Galaxy Clusters. I. Application to a Sample of 25 Clusters*. ApJ, **625**, 108. [link]

Diaferio, A., Geller, M. J., & Rines, K. J. (2005): *Caustic and Weak-Lensing Estimators of Galaxy Cluster Masses*. ApJ, **628**, L97. [link]

Dolag, K., Bartelmann, M., Perrotta, F., et al. (2004): *Numerical study of halo concentrations in dark-energy cosmologies*. A&A, **416**, 853. [link]

Dolag, K., Borgani, S., Murante, G., et al. (2009): *Substructures in hydrodynamical cluster simulations*. MNRAS, **399**, 497. [link]

Dolag, K., Vazza, F., Brunetti, G., et al. (2005): *Turbulent gas motions in galaxy cluster simulations: the role of smoothed particle hydrodynamics viscosity*. MNRAS, **364**, 753. [link]

Doré, O., Bouchet, F. R., Mellier, Y., et al. (2001): *Cluster physics from joint weak gravitational lensing and Sunyaev-Zel'dovich data*. A&A, **375**, 14. [link]

Duffy, A. R., Schaye, J., Kay, S. T., et al. (2008): *Dark matter halo concentrations in the Wilkinson Microwave Anisotropy Probe year 5 cosmology*. MNRAS, **390**, L64. [link]

Duffy, A. R., Schaye, J., Kay, S. T., et al. (2010): *Impact of baryon physics on dark matter structures: a detailed simulation study of halo density profiles*. MNRAS, **405**, 2161. [link]

Eckert, D., Molendi, S., Gastaldello, F., et al. (2011): *X-ray observations of PKS 0745-191 at the virial radius: are we there yet?* A&A, **529**, A133. [link]

Eckert, D., Molendi, S., Vazza, F., et al. (2013): *The X-ray/SZ view of the virial region. I. Thermodynamic properties*. A&A, **551**, A22. [link]

Eckert, D., Vazza, F., Ettori, S., et al. (2012): *The gas distribution in the outer regions of galaxy clusters*. A&A, **541**, A57. [link]

Einstein, A. (1915): *Die Feldgleichungen der Gravitation*. Sitzungsberichte der Königlich Preußischen Akademie der Wissenschaften (Berlin), Seite 844-847., 844–847

Eke, V. R., Navarro, J. F., & Steinmetz, M. (2001): *The Power Spectrum Dependence of Dark Matter Halo Concentrations*. ApJ, **554**, 114. [link]

Ettori, S., Donnarumma, A., Pointecouteau, E., et al. (2013): *Mass Profiles of Galaxy Clusters from X-ray Analysis*. Space Sci. Rev., **177**, 119. [link]

Fabian, A. C. (1994): *Cooling Flows in Clusters of Galaxies*. ARA&A, **32**, 277. [link]

Fabian, A. C., Hu, E. M., Cowie, L. L., et al. (1981): *The distribution and morphology of X-ray-emitting gas in the core of the Perseus cluster*. ApJ, **248**, 47. [link]

Finoguenov, A., Reiprich, T. H., & Böhringer, H. (2001): *Details of the mass-temperature relation for clusters of galaxies*. A&A, **368**, 749. [link]

Friedmann, A. (1922): *Über die Krümmung des Raumes*. Zeitschrift für Physik, **10** (1), 377. [link]

Friedmann, A. (1924): *Über die Möglichkeit einer Welt mit konstanter negativer Krümmung des Raumes*. Zeitschrift für Physik, **21** (1), 326. [link]

Gao, L., Frenk, C. S., Boylan-Kolchin, M., et al. (2011): *The statistics of the subhalo abundance of dark matter haloes*. MNRAS, **410**, 2309. [link]

Gao, L., Navarro, J. F., Cole, S., et al. (2008): *The redshift dependence of the structure of massive Λ cold dark matter haloes*. MNRAS, **387**, 536. [link]

Gao, L., White, S. D. M., Jenkins, A., et al. (2004): *The subhalo populations of ΛCDM dark haloes*. MNRAS, **355**, 819. [link]

Gardini, A., Rasia, E., Mazzotta, P., et al. (2004): *Simulating Chandra observations of galaxy clusters*. MNRAS, **351**, 505. [link]

Giavalisco, M., Ferguson, H. C., Koekemoer, A. M., et al. (2004): *The Great Observatories Origins Deep Survey: Initial Results from Optical and Near-Infrared Imaging*. ApJ, **600**, L93. [link]

Giocoli, C., Tormen, G., Sheth, R. K., et al. (2010): *The substructure hierarchy in dark matter haloes*. MNRAS, **404**, 502. [link]

Gitti, M., Ferrari, C., Domainko, W., et al. (2007): *Discovery of diffuse radio emission at the center of the most X-ray-luminous cluster RX J1347.5-1145*. A&A, **470**, L25. [link]

Gitti, M. & Schindler, S. (2004): *XMM-Newton observation of the most X-ray-luminous galaxy cluster RX J1347.5-1145*. A&A, **427**, L9. [link]

Glenn, J., Bock, J. J., Chattopadhyay, G., et al., *Bolocam: a millimeter-wave bolometric camera*. In T. G. Phillips, ed., *Advanced Technology MMW, Radio, and Terahertz Telescopes*, volume 3357 of *Society of Photo-Optical Instrumentation Engineers (SPIE) Conference Series*, 326–334 (1998)

Goldberg, D. M. & Leonard, A. (2007): *Measuring Flexion*. ApJ, **660**, 1003. [link]

Hasinger, G. (1996): *The extragalactic X-ray and gamma-ray background.* A&AS, **120**, C607

Heavens, A. (2003): *3D weak lensing*. MNRAS, **343**, 1327. [link]

Hinshaw, G., Larson, D., Komatsu, E., et al. (2013): *Nine-year Wilkinson Microwave Anisotropy Probe (WMAP) Observations: Cosmological Parameter Results*. ApJS, **208**, 19. [link]

Hoekstra, H., Franx, M., Kuijken, K., et al. (1998): *Weak lensing analysis of CL 1358+62*. New A Rev., **42**, 137. [link]

Horne, K., *Maximum entropy reconstruction of accretion disk images from eclipse data*. In P. P. Eggleton & J. E. Pringle, eds., *NATO ASIC Proc. 150: Interacting Binaries*, 327–348 (1985)

Hubble, E. (1929): *A Relation between Distance and Radial Velocity among Extra-Galactic Nebulae*. Proceedings of the National Academy of Science, **15**, 168. [link]

Huber, K. (2013): *Joint reconstruction of a galaxy cluster's mass distribution: Combining gravitational lensing with information from thermal gas and galaxy kinematics*. Master's thesis, Heidelberg, Univ., Master Thesis

Jenkins, A., Frenk, C. S., White, S. D. M., et al. (2001): *The mass function of dark matter haloes*. MNRAS, **321**, 372. [link]

Jing, Y. P. & Suto, Y. (2000): *The Density Profiles of the Dark Matter Halo Are Not Universal*. ApJ, **529**, L69. [link]

Jing, Y. P. & Suto, Y. (2002): *Triaxial Modeling of Halo Density Profiles with High-Resolution N-Body Simulations*. ApJ, **574**, 538. [link]

Kaiser, N., Squires, G., & Broadhurst, T. (1995): *A Method for Weak Lensing Observations*. ApJ, **449**, 460. [link]

Kawaharada, M., Okabe, N., Umetsu, K., et al. (2010): *Suzaku Observation of A1689: Anisotropic Temperature and Entropy Distributions Associated with the Large-scale Structure*. ApJ, **714**, 423. [link]

Komatsu, E., Smith, K. M., Dunkley, J., et al. (2011): *Seven-year Wilkinson Microwave Anisotropy Probe (WMAP) Observations: Cosmological Interpretation*. ApJS, **192**, 18. [link]

Konrad, S., Majer, C. L., Meyer, S., et al. (2013): *Joint reconstruction of galaxy clusters from gravitational lensing and thermal gas. I. Outline of a non-parametric method.* A&A, **553**, A118. [link]

Kriss, G. A., Cioffi, D. F., & Canizares, C. R. (1983): *The X-ray emitting gas in poor clusters with central dominant galaxies*. ApJ, **272**, 439. [link]

Lahav, O. & Gull, S. F. (1989): *Distances to clusters of galaxies by maximum entropy method*. MNRAS, **240**, 753

Lemaître, G. (1927): *Un Univers homogène de masse constante et de rayon croissant rendant compte de la vitesse radiale des nébuleuses extra-galactiques*. Annales de la Societe Scietifique de Bruxelles, **47**, 49

Lewis, A., Challinor, A., & Lasenby, A. (2000): *Efficient Computation of Cosmic Microwave Background Anisotropies in Closed Friedmann-Robertson-Walker Models*. ApJ, **538**, 473. [link]

Liddle, A. R. & Lyth, D. H., *Cosmological inflation and large scale structure* (Cambridge University Press, Cambridge [u.a.], 2000). Includes index

Lucy, L. B. (1974): *An iterative technique for the rectification of observed distributions*. AJ, **79**, 745. [link]

Lucy, L. B., *Astronomical Inverse Problems.* In G. Klare, ed., *Reviews in Modern Astronomy*, volume 7 of *Reviews in Modern Astronomy*, 31–50 (1994a)

Lucy, L. B. (1994b): *Optimum strategies for inverse problems in statistical astronomy*. A&A, **289**, 983

Lundgren, A. (2012): *ALMA Cycle 1 Technical Handbook, Version 1.01*. ALMA

Lundgren, A. (2013): *ALMA Cycle 2 Technical Handbook Version 1.1*. ALMA

Luppino, G. A. & Kaiser, N. (1997): *Detection of Weak Lensing by a Cluster of Galaxies at Z = 0.83*. ApJ, **475**, 20. [link]

Macciò, A. V., Dutton, A. A., & van den Bosch, F. C. (2008): *Concentration, spin and shape of dark matter haloes as a function of the cosmological model: WMAP1, WMAP3 and WMAP5 results*. MNRAS, **391**, 1940. [link]

Macciò, A. V., Dutton, A. A., van den Bosch, F. C., et al. (2007): *Concentration, spin and shape of dark matter haloes: scatter and the dependence on mass and environment*. MNRAS, **378**, 55. [link]

Majer, C. L., Meyer, S., Konrad, S., et al. (2013): *Joint reconstruction of galaxy clusters from gravitational lensing and thermal gas. II. Inversion of the thermal Sunyaev-Zel'dovich effect*. ArXiv e-prints

Mamon, G. A. & Boué, G. (2010): *Kinematic deprojection and mass inversion of spherical systems of known velocity anisotropy*. MNRAS, **401**, 2433. [link]

Mason, B. S., Dicker, S. R., Korngut, P. M., et al. (2010): *Implications of a High Angular Resolution Image of the Sunyaev-Zel'Dovich Effect in RXJ1347-1145*. ApJ, **716**, 739. [link]

Medezinski, E., Broadhurst, T., Umetsu, K., et al. (2010): *Detailed cluster mass and light profiles of A1703, A370 and RXJ1347-11 from deep Subaru imaging*. MNRAS, **405**, 257. [link]

Melchior, P. (2010): *Shapelets for gravitational lensing and galaxy morphology studies*. Ph.D. thesis, Heidelberg, Univ., Diss., 2010

Meneghetti, M. (2007): *Introduction to Gravitational Lensing*. Lecture scripts

Meneghetti, M., Argazzi, R., Pace, F., et al. (2007): *Arc sensitivity to cluster ellipticity, asymmetries, and substructures*. A&A, **461**, 25. [link]

Meneghetti, M., Fedeli, C., Pace, F., et al. (2010a): *Strong lensing in the MARENOSTRUM UNIVERSE. I. Biases in the cluster lens population*. A&A, **519**, A90. [link]

Meneghetti, M., Melchior, P., Grazian, A., et al. (2008): *Realistic simulations of gravitational lensing by galaxy clusters: extracting arc parameters from mock DUNE images*. A&A, **482**, 403. [link]

Meneghetti, M., Rasia, E., Merten, J., et al. (2010b): *Weighing simulated galaxy clusters using lensing and X-ray*. A&A, **514**, A93. [link]

Meneghetti, M., Rasia, E., Vega, J., et al. (2014): *The MUSIC of CLASH: predictions on the concentration-mass relation*. ArXiv e-prints

Merkel, P. M. (2013): *Different aspects of the interplay between light and the large-scale structure of the Universe*. Ph.D. thesis, Heidelberg, Univ., Diss., 2013

Merritt, D., Graham, A. W., Moore, B., et al. (2006): *Empirical Models for Dark Matter Halos. I. Nonparametric Construction of Density Profiles and Comparison with Parametric Models*. AJ, **132**, 2685. [link]

Merten, J. (2010): *Gravitational lensing*. Ph.D. thesis, Heidelberg, Univ., Diss., 2010

Merten, J., Cacciato, M., Meneghetti, M., et al. (2009): *Combining weak and strong cluster lensing: applications to simulations and MS 2137*. A&A, **500**, 681. [link]

Moore, B., Governato, F., Quinn, T., et al. (1998): *Resolving the Structure of Cold Dark Matter Halos*. ApJ, **499**, L5. [link]

Moore, B., Quinn, T., Governato, F., et al. (1999): *Cold collapse and the core catastrophe*. MNRAS, **310**, 1147. [link]

Mukhanov, V. F., *Physical foundations of cosmology* (Cambridge Univ. Press, Cambridge [u.a.], 2008), repr. edition

Nagai, D., Kravtsov, A. V., & Vikhlinin, A. (2007): *Effects of Galaxy Formation on Thermodynamics of the Intracluster Medium*. ApJ, **668**, 1. [link]

Narayan, R. & Nityananda, R. (1986): *Maximum entropy image restoration in astronomy*. ARA&A, **24**, 127. [link]

Navarro, J. F., Frenk, C. S., & White, S. D. M. (1996): *The Structure of Cold Dark Matter Halos*. ApJ, **462**, 563

Navarro, J. F., Frenk, C. S., & White, S. D. M. (1997): *A Universal Density Profile from Hierarchical Clustering*. ApJ, **490**, 493

Navarro, J. F., Hayashi, E., Power, C., et al. (2004): *The inner structure of ΛCDM haloes - III. Universality and asymptotic slopes*. MNRAS, **349**, 1039. [link]

Neto, A. F., Gao, L., Bett, P., et al. (2007): *The statistics of Λ CDM halo concentrations*. MNRAS, **381**, 1450. [link]

Nord, M., Basu, K., Pacaud, F., et al. (2009): *Multi-frequency imaging of the galaxy cluster Abell 2163 using the Sunyaev-Zel'dovich effect*. A&A, **506**, 623. [link]

Oguri, M., Hennawi, J. F., Gladders, M. D., et al. (2009): *Subaru Weak Lensing Measurements of Four Strong Lensing Clusters: Are Lensing Clusters Overconcentrated?* ApJ, **699**, 1038. [link]

Oguri, M., Lee, J., & Suto, Y. (2003): *Arc Statistics in Triaxial Dark Matter Halos: Testing the Collisionless Cold Dark Matter Paradigm*. ApJ, **599**, 7. [link]

Padmanabhan, T., *Structure formation in the universe* (Cambridge University Press, Cambridge, 1993), 1. publ. edition

Peng, E.-H., Andersson, K., Bautz, M. W., et al. (2009): *Discrepant Mass Estimates in the Cluster of Galaxies Abell 1689*. ApJ, **701**, 1283. [link]

Perlmutter, S., Aldering, G., Goldhaber, G., et al. (1999): *Measurements of Omega and Lambda from 42 High-Redshift Supernovae*. ApJ, **517**, 565. [link]

Plagge, T. J., Marrone, D. P., Abdulla, Z., et al. (2013): *CARMA Measurements of the Sunyaev-Zel'dovich Effect in RX J1347.5-1145*. ApJ, **770**, 112. [link]

Planck Collaboration (2013a): *Planck 2013 results. XVI. Cosmological parameters*. ArXiv e-prints

Planck Collaboration (2013b): *Planck intermediate results. V. Pressure profiles of galaxy clusters from the Sunyaev-Zeldovich effect*. A&A, **550**, A131. [link]

Postman, M., Coe, D., Benitez, N., et al. (2012): *CLASH sources for MACS1149.6+2223 (Postman+, 2012)*. VizieR Online Data Catalog, **219**, 90025

Power, C., Navarro, J. F., Jenkins, A., et al. (2003): *The inner structure of ΛCDM haloes - I. A numerical convergence study*. MNRAS, **338**, 14. [link]

Press, W. H. & Schechter, P. (1974): *Formation of Galaxies and Clusters of Galaxies by Self-Similar Gravitational Condensation*. ApJ, **187**, 425. [link]

Puchwein, E. (2007): *On the structure of galaxy clusters*. Ph.D. thesis, Heidelberg, Univ., Diss., 2007

Puchwein, E. & Bartelmann, M. (2006): *Three-dimensional reconstruction of the intra-cluster medium*. A&A, **455**, 791. [link]

Puchwein, E., Bartelmann, M., Dolag, K., et al. (2005): *The impact of gas physics on strong cluster lensing*. A&A, **442**, 405. [link]

Rasia, E., Ettori, S., Moscardini, L., et al. (2006): *Systematics in the X-ray cluster mass estimators*. MNRAS, **369**, 2013. [link]

Rasia, E., Mazzotta, P., Bourdin, H., et al. (2008): *X-MAS2: Study Systematics on the ICM Metallicity Measurements*. ApJ, **674**, 728. [link]

Ratra, B. & Peebles, P. J. E. (1988): *Cosmological consequences of a rolling homogeneous scalar field*. Phys. Rev. D, **37**, 3406. [link]

Reblinsky, K. (2000a): *Cluster deprojection combining multiple observable data sets*. A&A, **364**, 377

Reblinsky, K. (2000b): *Projection effects in clusters of galaxies*. Ph.D. thesis, München, Univ., Diss., 2000

Riess, A. G., Filippenko, A. V., Challis, P., et al. (1998): *Observational Evidence from Supernovae for an Accelerating Universe and a Cosmological Constant*. AJ, **116**, 1009. [link]

Robertson, H. P. (1935): *Kinematics and World-Structure*. ApJ, **82**, 284. [link]

Sarazin, C. L. (1986): *X-ray emission from clusters of galaxies*. Rev. Mod. Phys., **58**, 1. [link]

Sarazin, C. L. & Surdin, V. G. (1988): *Book-Review - X-Ray Emission from Clusters of Galaxies*. Soviet Ast., **32**, 581

Sarli, E., Meyer, S., Meneghetti, M., et al. (2013): *Reconstructing the projected gravitational potential of galaxy clusters from galaxy kinematics*. ArXiv e-prints

Saro, A., Borgani, S., Tornatore, L., et al. (2006): *Properties of the galaxy population in hydrodynamical simulations of clusters*. MNRAS, **373**, 397. [link]

Sayers, J., Czakon, N. G., Mantz, A., et al. (2013): *Sunyaev-Zel'dovich-measured Pressure Profiles from the Bolocam X-Ray/SZ Galaxy Cluster Sample*. ApJ, **768**, 177. [link]

Sayers, J., Golwala, S. R., Ameglio, S., et al. (2011): *Cluster Morphologies and Model-independent Y_{SZ} Estimates from Bolocam Sunyaev-Zel'dovich Images*. ApJ, **728**, 39. [link]

Schmidt, R. W. & Allen, S. W. (2007): *The dark matter haloes of massive, relaxed galaxy clusters observed with Chandra*. MNRAS, **379**, 209. [link]

Schneider, P., *Einführung in die extragalaktische Astronomie und Kosmologie* (Springer, Berlin ; Heidelberg [u.a.], 2006a)

Schneider, P., *Extragalactic astronomy and cosmology* (Springer, Berlin ; Heidelberg [u.a.], 2006b)

Schneider, P., Kochanek, C. S., & Wambsganss, J., *Gravitational lensing: strong, weak and micro*. XIII, 552 S. Saas Fee Advanced Course, 33, 2003, Les Diablerets; Schweizerische Gesellschaft für Astrophysik und Astronomie (Springer, Berlin ; Heidelberg ; New York, 2006). Literaturangaben. - Saas-Fee Advanced Course took place from 8-12 April 2003, in Les Diablerets, Switzerland

Schneider, P. & Seitz, C. (1995): *Steps towards nonlinear cluster inversion through gravitational distortions. 1: Basic considerations and circular clusters*. A&A, **294**, 411

Schuecker, P., Caldwell, R. R., Böhringer, H., et al. (2003): *Observational constraints on general relativistic energy conditions, cosmic matter density and dark energy from X-ray clusters of galaxies and type-Ia supernovae*. A&A, **402**, 53. [link]

Seitz, C. & Schneider, P. (1997): *Steps towards nonlinear cluster inversion through gravitational distortions. III. Including a redshift distribution of the sources.* A&A, **318**, 687

Seitz, S., Schneider, P., & Bartelmann, M. (1998): *Entropy-regularized maximum-likelihood cluster mass reconstruction*. A&A, **337**, 325

Seljak, U. (2000): *Analytic model for galaxy and dark matter clustering*. MNRAS, **318**, 203. [link]

Sereno, M. (2007): *On the deprojection of clusters of galaxies combining X-ray, Sunyaev-Zeldovich temperature decrement and gravitational lensing maps*. MNRAS, **380**, 1207. [link]

Sereno, M., De Filippis, E., Longo, G., et al. (2006): *Measuring the Three-dimensional Structure of Galaxy Clusters. II. Are Clusters of Galaxies Oblate or Prolate?* ApJ, **645**, 170. [link]

Sereno, M., Ettori, S., Umetsu, K., et al. (2013): *Mass, shape and thermal properties of Abell 1689 using a multiwavelength X-ray, lensing and Sunyaev-Zel'dovich analysis*. MNRAS, **428**, 2241. [link]

Sereno, M. & Zitrin, A. (2012): *Triaxial strong-lensing analysis of the z ¿ 0.5 MACS clusters: the mass-concentration relation*. MNRAS, **419**, 3280. [link]

Shaw, L. D., Weller, J., Ostriker, J. P., et al. (2006): *Statistics of Physical Properties of Dark Matter Clusters*. ApJ, **646**, 815. [link]

Sheth, R. K., Mo, H. J., & Tormen, G. (2001): *Ellipsoidal collapse and an improved model for the number and spatial distribution of dark matter haloes*. MNRAS, **323**, 1. [link]

Sheth, R. K. & Tormen, G. (1999): *Large-scale bias and the peak background split*. MNRAS, **308**, 119. [link]

Sheth, R. K. & Tormen, G. (2002): *An excursion set model of hierarchical clustering: ellipsoidal collapse and the moving barrier*. MNRAS, **329**, 61. [link]

Snowden, S. L., McCammon, D., Burrows, D. N., et al. (1994): *Analysis procedures for ROSAT XRT/PSPC observations of extended objects and the diffuse background*. ApJ, **424**, 714. [link]

Snowden, S. L., Mushotzky, R. F., Kuntz, K. D., et al. (2008): *A catalog of galaxy clusters observed by XMM-Newton*. A&A, **478**, 615. [link]

Springel, V. (2005): *The cosmological simulation code GADGET-2*. MNRAS, **364**, 1105. [link]

Sunyaev, R. A. & Zeldovich, I. B. (1980): *Microwave background radiation as a probe of the contemporary structure and history of the universe*. ARA&A, **18**, 537. [link]

Tchernin, C., Majer, C. L., Meyer, S., et al. (2013): *Reconstruction of the lensing potential of the cluster A1689 from X-ray measurements*. submitted to A&A

Tormen, G., Bouchet, F. R., & White, S. D. M. (1997): *The structure and dynamical evolution of dark matter haloes*. MNRAS, **286**, 865

Umetsu, K. & Broadhurst, T. (2008): *Combining Lens Distortion and Depletion to Map the Mass Distribution of A1689*. ApJ, **684**, 177. [link]

Umetsu, K., Medezinski, E., Nonino, M., et al. (2012): *CLASH: Mass Distribution in and around MACS J1206.2-0847 from a Full Cluster Lensing Analysis*. ApJ, **755**, 56. [link]

Vikhlinin, A., Forman, W., & Jones, C. (1999): *Outer Regions of the Cluster Gaseous Atmospheres*. ApJ, **525**, 47. [link]

Voges, W., Aschenbach, B., Boller, T., et al. (1999): *The ROSAT all-sky survey bright source catalogue*. A&A, **349**, 389

Walker, A. G. (1935): *On Riemannian Spaces with Spherical Symmetrie about a Line, and the Conditions for Isotropy in General Relativity*. The Quarterly Journal of Mathematics, **os-6** (1), 81. [link]

Warren, M. S., Abazajian, K., Holz, D. E., et al. (2006): *Precision Determination of the Mass Function of Dark Matter Halos*. ApJ, **646**, 881. [link]

Weinberg, S., *Cosmology* (Oxford Univ. Press, Oxford [u.a.], 2008), 1. publ. edition

Wetterich, C. (1988): *Cosmology and the fate of dilatation symmetry*. Nuclear Physics B, **302**, 668. [link]

Yoshida, N., Sheth, R. K., & Diaferio, A. (2001): *Non-Gaussian cosmic microwave background temperature fluctuations from peculiar velocities of clusters*. MNRAS, **328**, 669. [link]

Yuan, Q., Zhang, T.-J., & Wang, B.-Q. (2008): *Reconstruction of Gas Temperature and Density Profiles of the Galaxy Cluster RX J1347.5 1145*. Chinese J. Astron. Astrophys., **8**, 671. [link]

Zel'dovich, Y. B. (1970): *Gravitational instability: An approximate theory for large density perturbations.* A&A, **5**, 84

Zentner, A. R., Berlind, A. A., Bullock, J. S., et al. (2005): *The Physics of Galaxy Clustering. I. A Model for Subhalo Populations*. ApJ, **624**, 505. [link]

Zhao, D. H., Jing, Y. P., Mo, H. J., et al. (2009): *Accurate Universal Models for the Mass Accretion Histories and Concentrations of Dark Matter Halos*. ApJ, **707**, 354. [link]

Zitrin, A., Meneghetti, M., Umetsu, K., et al. (2013): *CLASH: The Enhanced Lensing Efficiency of the Highly Elongated Merging Cluster MACS J0416.1-2403*. ApJ, **762**, L30. [link]

Zitrin, A., Rosati, P., Nonino, M., et al. (2012): *CLASH: New Multiple Images Constraining the Inner Mass Profile of MACS J1206.2-0847*. ApJ, **749**, 97. [link]

Zwicky, F. (1933): *Die Rotverschiebung von extragalaktischen Nebeln*. Helvetica Physica Acta, **6**, 110

Zwicky, F. (1937): *On the Masses of Nebulae and of Clusters of Nebulae*. ApJ, **86**, 217. [link]

Acknowledgements

As usual, the last part has its own intriguing charm. This work, which was supported by the Deutsche Forschungsgemeinschaft, has not been possible without the help of many other people. Continuing with regard to the contents from above, the first person is Matthias Bartelmann. I am very thankful that he gave me this unique opportunity to write my thesis within his group at the Institute of Theoretical Astrophysics (ITA) where I had such a fine time. Even more, I learned more from Matthias than I had ever expected – Thank you.
Furthermore, I want to thank Joachim Wambsganß for taking the time to be the second referee for my thesis. And of course I am grateful to Eva Grebel and Peter Bachert for completing my thesis committee.

I also want to express my gratitude to my IMPRS thesis committee consisting of Matthias Bartelmann, Joseph Hennawi and Julian Merten. Your combined advice was a very good route to follow.

The ITA would be nothing without my great long-term office mates: Francesco Pace and Philipp Merkel – I owe Philipp more than he thinks. I am also very grateful to have shared an office with Britta Zieser. She was probably the one person in the office I got to know the closest and not to forget her baking skills. Though I did not share a room with you guys – Matthias Redlich, Alexander Gelsin, Sven Meyer, Eleonora Sarli, Agnese Fabris and Gero Jürgens – we had a great time and working with you was so much fun! Not to forget my favourite post-doc, Christian Angrick, you often found the right words when I was in need of good advice, not to mention your 'eagle eyes'. And last, but certainly not least, I want to thank Björn Malte Schäfer for having the time for any of my questions.

Besides the friends I found at the ITA, I was also part of the 7^{th} IMPRS generation in Heidelberg, with whom I also had a great time. Of course, the IMPRS in Heidelberg would not be as cordial as it is without Christian Fendt – thank you.

Leaving the field of cosmology and astrophysics and entering particle physics, I want to thank my good friend Johannes ter Wolbeek. He, maybe like no other, understood my moods when things were not as they should be. A major role in my work-life balance was played by my parents and my sister, who always took care of me when the need was there. And finally, we reach the one person in my life responsible for cheering me up most of the time – Anne Heedrich. Thank you so much for all you have for me done in the last years!